

NSG-7155

California Institute of Technology
Pasadena, California 91109
"Mariner 10 Data Analysis"

(NASA-CR-149463) MARINER 10 DATA ANALYSIS.
1: SCARPS, RIDGES, TROUGHS, AND OTHER
LINEAMENTS ON MERCURY. 2: GEOLOGIC
SIGNIFICANCE OF PHOTOMETRIC VARIATIONS ON
MERCURY Ph.D. Thesis (California Inst. of

G3/91

N77-16973
HC R09
MF R01
Uncias
13288



- 1. SCARPS, RIDGES, TROUGHS, AND OTHER LINEAMENTS
ON MERCURY**
- 2. GEOLOGIC SIGNIFICANCE OF PHOTOMETRIC VARIATIONS
ON MERCURY**

Thesis by

Daniel Dzurisin

In Partial Fulfillment of the Requirements

for the Degree of

Doctor of Philosophy

California Institute of Technology

Pasadena, California

1977

(Submitted December 13, 1976)

Copyright © by

DANIEL DZURISIN

1976

DEDICATION

To Linda, for patience, warmth, and understanding.

ACKNOWLEDGMENTS

From the excitement of Mariner 10's launch, through anxious months of interplanetary cruise and four historic planetary encounters, to post-flight data analysis and thesis research, my graduate career at Caltech has been marked by singular events and opportunities for which I am openly grateful. Even more memorable than these have been my associations and interactions with distinguished members of the Caltech faculty. Dr. Bruce C. Murray steadfastly supported and encouraged my research interests in Mariner 9 and Mariner 10 image analysis, and routinely dispensed with obstacles to my progress which could otherwise have been fatal. His scientific and leadership abilities provided an uncompromising standard of excellence to challenge my educational and research ambitions. Dr. Robert P. Sharp greatly extended my appreciation of geomorphic forms and processes, and produced meticulous reviews which greatly enhanced the credibility of this work. Professor Sharp's unquestionable expertise, his easy manner, and personal concern for his students are admired by all who know him. It was a distinct personal honor to have been associated with this singular gentlemen during my stay at Caltech.

The assistance of Mr. G. Edward Danielson and Dr. Michael C. Malin of the Jet Propulsion Laboratory was critical to the timely completion of this work. Mr. Danielson contributed his expertise in Mariner 10 photometry, made available graphic arts and image processing facilities, and provided encouragement and good humor throughout my thesis research. Dr. Malin gave freely of his time to read and discuss early manuscripts,

and was unrelenting in his constructive criticism of unsatisfactory work. His friendship and candor are deeply appreciated.

Mr. Kenneth P. Klaassen of the Jet Propulsion Laboratory offered expert advice on technical topics concerning photometric measurements from spacecraft. Frequent discussions with Dr. H. Jay Melosh of Caltech advanced my understanding of theoretical rock mechanics and implications for planetary tectonism. Messrs. Donald J. Lynn, Joel A. Mosher, and Denis A. Elliott of the Image Processing Laboratory (Jet Propulsion Laboratory) were responsible for unprecedented advances in image processing which were critical to production of many images contained herein. Kay Campbell and Brenda Parson deciphered my primitive penmanship in a timely fashion to produce immaculate typewritten copies of several early drafts and the final manuscript.

This work was supported in part by a National Science Foundation graduate Research Fellowship and by National Aeronautics and Space Administration grants NAS 7-100 and NSG 7155.

ABSTRACT

Volcanic and tectonic implications of the surface morphology of Mercury are addressed in two separate sections. In Part 1, mercurian scarps, ridges, troughs, and other lineaments are described and classified as planimetrically linear, arcuate, lobate, or irregular. A global pattern of lineaments is interpreted to reflect modification of linear crustal joints formed in response to stresses induced by tidal spindown. Large arcuate scarps on Mercury most likely record a period of compressional tectonism near the end of heavy bombardment. Shrinkage owing to planetary cooling is the mechanism preferred for their production. Two planimetrically lobate escarpments probably formed by uplift along intersecting elements of the global mercurian lineament pattern. One may subsequently have been modified by extrusive igneous activity along its trace. Most irregular scarps inside craters are interpreted to be tectonic features formed in response to local stresses, perhaps induced by subsurface magma movements.

Large linear ridges on Mercury may record a period of volcanism responsible, at least in part, for intercrater plains formation. Linear ridge production is speculatively attributed to accumulation of extruded material along linear vents, and to differential erosion around relatively resistant dikes intruded into near-surface materials.

Linear, open-ended troughs are well-developed in a distinct terrain unit on Mercury characterized by intense modification of pre-existing landforms. Regional trends defined by these troughs are consistent with those of the global mercurian lineament pattern. Combined with their

regional setting, this suggests that the troughs formed by differential erosion along linear crustal fractures. A few are radial from nearby large craters, and may be highly modified chains of secondary impact craters.

Scarp s, ridges, and troughs in and around Caloris Basin define trends radial from the basin center and concentric with its rim. A radial system of linear ridges outside Caloris probably reflects the combined effects of ejecta deposition and erosion during the basin-forming event. Planimetrically irregular ridges developed in smooth plains inside Caloris may owe their origin to regional subsidence, perhaps in response to magma withdrawal from below to form smooth plains outside the basin rim. Gravitational readjustment owing to loading by plains material may be responsible for scarp and ridge formation outside Caloris. Finally, isostatic readjustment to basin excavation may have caused regional uplift inside the basin to form a system of planimetrically irregular troughs.

In Part 2, measurements of local normal albedo are combined with computer-generated photometric maps of Mercury to provide constraints on the nature of mercurian surface materials and processes. If the mercurian surface obeys the average lunar photometric function, its normal albedo at 554 nm is $.16 \pm .03$. This is roughly 40% higher than the corresponding lunar value, but the difference may be largely attributable to differences in the photometric functions of the two bodies, and to unmodelled effects such as multiple scattering. The

existence of relatively bright smooth plains confined to crater floors is most easily reconciled with a volcanic origin for some mercurian smooth plains. Lack of photometric contrast across most large escarpments on Mercury is consistent with the tectonic origin for these features inferred from morphologic studies. Local photometric and transectional relationships in two instances suggest mantling of pre-existing topography by younger, perhaps volcanic, material. Brightness of several extremely localized patches in large craters is attributed to enhanced backscatter owing to multiple reflections relative to surrounding plains and craters. These patches are generally "bluer" than typical mercurian plains, and some are surrounded by material which is "redder" than typical plains. Chemical alteration of crustal rocks, perhaps related to fumarolic activity along impact-induced fractures, is the preferred explanation for these uniquely mercurian features.

TABLE OF CONTENTS

<u>Part</u>		<u>Page</u>
I	SCARPS, RIDGES, TROUGHS, AND OTHER LINEAMENTS ON MERCURY	1
	Introduction	2
	Morphologic Classification of Scarps, Ridges, and Troughs	4
	Background	4
	Classification of Mercurian Scarps, Ridges, and Troughs	5
	Scarps	8
	Arcuate Scarps	8
	Lobate Scarps	13
	Irregular Intracrater Scarps	15
	Irregular Scarps of the Caloris Region	17
	Ridges	20
	Linear Ridges	20
	Irregular Ridges	22
	Troughs	24
	Linear Troughs	24
	Irregular Troughs	24
	Lineaments	26
	Summary	28
	Scarps	28
	Ridges	29

<u>Part</u>	<u>Page</u>
I SCARPS RIDGES, TROUGHS, AND OTHER LINEAMENTS ON MERCURY (Continued)	
Summary (Continued)	
Troughs	30
Lineaments	30
Discussion	32
Arcuate Scarps	32
Global Lineament Pattern	34
Lobate Scarps	37
Irregular Intracrater Scarps	41
Linear Ridges	44
Linear Troughs	46
Scarps, Ridges, and Troughs of the Caloris Region	47
Synthesis	51
References	57
Figure Captions	61
Figures	77
II GEOLOGIC SIGNIFICANCE OF PHOTOMETRIC VARIATIONS ON MERCURY	126
Introduction	127
Data	128
Reliability	128
Local Normal Albedos	128

<u>Part</u>		<u>Page</u>
II	GEOLOGIC SIGNIFICANCE OF PHOTOMETRIC VARIATIONS ON MERCURY (Continued)	
	Data (Continued)	
	Global Photometric Maps	131
	Average Normal Albedo	133
	Discussion	134
	Similarity of Heavily Cratered Terrain, Intercrater Plains, and Caloris Plains	134
	Photometric Contrast Across Escarpments	136
	Bright and Dark Smooth Plains	138
	Localized Bright Patches	141
	Summary	146
	References	147
	Tables	150
	Figure Captions	157
	Figures	163

PART 1

Scarps, Ridges, Troughs, and Other Lineaments on Mercury

INTRODUCTION

Mariner 10 photographs suggest that Mercury has experienced an extended and diverse evolutionary history at least partly recorded in the present configuration of the planet's surface. Initial studies by members of the Mariner 10 Imaging Science Team provide a framework for more detailed discussions of mercurian surface history. Murray et al. (1975) compared regional terrain variations on Mercury and the Moon, and proposed a five-stage evolutionary history for Mercury: 1) accretion and differentiation; 2) terminal heavy bombardment; 3) formation of Caloris Basin; 4) basin flooding and smooth plains formation by volcanic processes; and 5) reduced post-plains cratering. Strom et al. (1975) discussed the morphology and distribution of major mercurian escarpments, and attributed most to a period of global compression during the final phase of heavy bombardment. Trask and Guest (1975) cited morphologic and transectional evidence for three distinct periods of plains formation on Mercury (smooth plains, hummocky plains, intercrater plains), and suggested that widespread smooth plains were produced by extensive crustal melting and volcanism. Murray et al. (1975) and Strom et al. (1975) argued that older intercrater plains on Mercury are also of volcanic origin. These studies suggest that the mercurian surface has been modified by extensive volcanism and tectonism throughout much of its history. Resulting landforms are in part seemingly unique to Mercury. Their careful study holds promise for further insights into surface evolution on Mercury and, by comparison, on other terrestrial bodies as well.

This paper describes mercurian scarps, ridges, troughs, and other lineaments, proposes a scheme for their morphologic classification, and discusses their implications for mercurian volcanism and tectonism.

Some non-crater forms such as isolated peaks, quasi-circular depressions, and a group of morphologically complex south polar landforms are not treated. The origin of intercrater plains, smooth plains within some large craters and basins, and Caloris plains both inside and outside the rim of Caloris Basin are addressed only by inference from superimposed landforms. Early sections of this paper present descriptive material, including global maps of mercurian scarps, ridges, troughs, and other lineaments, and morphologic descriptions of type localities which form the basis for a non-genetic classification system. These descriptive data are referenced in later sections which discuss alternative explanations, and their implications for mercurian tectonism and volcanism. At least three distinct tectonic periods are identified, and evidence for early igneous intrusive and extrusive activity is discussed. A tentative volcanic/tectonic chronology for Mercury is presented in the paper's final section.

MORPHOLOGIC CLASSIFICATION OF SCARPS, RIDGES, AND TROUGHS

Background

Description and interpretation of high resolution spacecraft images of the planets has established a need for a generalized, morphologic classification system for surface landforms. For craters, this need has been met by schemes based on rim crispness, floor morphology, preservation of central peaks, wall terraces, ejecta deposits, and secondary crater fields; and other morphologic parameters (e.g., Arthur, 1963; Pohn and Offield, 1970; Pike, 1974).

No corresponding system exists for non-crater forms on planets other than Earth. Classical schemes developed for terrestrial landforms are not generally applicable, because they are based on criteria too specific to be evaluated from spacecraft photography, and because some extra-terrestrial landforms have no direct earthly analog. Faced with these difficulties, Sharp (1973a,b,c) in a pioneering series of papers presented morphologic descriptions of troughed, fretted, chaotic, pitted, and etched terrains on Mars. Resulting terrain characterizations provided a basis for speculative interpretation of a wide variety of martian landforms. In a subsequent work, Sharp and Malin (1975) described the morphologies of prominent channel-forms on Mars and suggested type localities to serve as a framework for classification of martian channels by genesis. With these earlier efforts in mind, detailed morphologic description and classification coupled with type examples or localities

are used here as a basis for discussion and interpretation of scarps, ridges, and troughs on Mercury.

Classification of Mercurian Scarps, Ridges, and Troughs

Strom et al. (1975) applied the term "lobate scarps" to "relatively steep and long escarpments which usually show a broadly lobate outline on a scale of a few to tens of kilometers." This scheme does not distinguish between major scarps cutting large craters and intercrater plains, scarps confined to smooth plains flooring relatively large craters, and scarps of the Caloris plains, some of which are transitional into ridges. Many of these features are of distinctly differing morphology and demonstrably differing age. More detailed description and classification therefore seem appropriate. For purposes of this paper, mercurian scarps, ridges, and troughs have been divided into several morphologic groups based on planimetric form and specific morphologic characteristics. This approach was chosen for its simplicity, generality, and lack of genetic implications.

Planimetrically, mercurian scarps, ridges, and troughs can be classed as linear, arcuate, lobate, or irregular (Figure 1). "Linear" is used here as an adjective to describe surface features characterized by planimetric linearity (O'Leary et al., 1976). "Arcuate" is used in the traditional sense to describe features which are gently bowed or curved in the form of segments or sections of circles. The term is distinguished from "lobate", which is applied to margins of elongate tongues or projections (i.e., "lobes"). "Irregular" applies here to planimetrically more complex forms which may in part be curved, sinuous,

or angular. The distinction is best illustrated in Figure 1, which gives examples of each planimetric class.

Additional descriptors used to further classify mercurian scarps, ridges, and troughs include dimensional parameters, small-scale morphology, geologic and topographic setting, and geographic location.

Relief was determined by stereo photogrammetry or by comparison in stereo images with craters whose depths were measured by shadow analysis.

Thus Mirni Ridge (Figure 1,D) can be characterized as a NW/SE trending linear ridge roughly 175 km long, 5 km wide, and nearly 1 km high which disrupts two large craters near 37°S latitude and 40°W longitude.

Hero Scarp (Figure 1,A), for comparison, is described as an arcuate escarpment roughly 500 km long and 0.5-1.0 km high which cuts across intercrater plains and several large craters near 57°S, 173°W. An unnamed escarpment at 24°S latitude, 53°W longitude (Figure 1,B) is classed as planimetrically lobate, with irregular outline in detail.

Finally, Figure 1,G shows a group of planimetrically irregular troughs which cut smooth plains inside Caloris Basin at 30°N, 190°W. These examples are treated in more detail in later sections.

Global maps of all mercurian scarps, ridges, and troughs included in this study are presented in Figures 2-4. As shown in those figures, roughly 80% of all scarps studied face toward terminators, in both incoming (evening) and outgoing (morning) quadrants. This probably reflects in large part enhanced visibility of scarps with shadows, suggesting that many sun-facing scarps remain unrecognized in Mariner 10 photographs. The observed predominance of terminator-facing scarps

could be a real consequence of their modes of origin, but this would require a highly constrained scarp distribution and fortuitous timing for Mariner 10 encounters with Mercury.

SCARPS

The terms "scarp" and "escarpment" are used here interchangeably for relatively steep, cliff-like slopes of considerable lateral extent separating terrain lying at different levels. Planimetrically linear scarps are relatively rare on Mercury. A few cut smooth plains inside large craters, or plains around Caloris Basin. Much more abundant on those surfaces are scarps which are curved or irregular in plan view, and hence all are discussed together under the heading "irregular scarps." Arcuate and lobate escarpments cutting large craters and intercrater plains comprise two additional scarp types treated below.

Arcuate Scarps

Planimetrically arcuate escarpments on Mercury are typically hundreds of kilometers long and roughly 1 km high. Their traces are characteristically convex as viewed from the downward side. Such features are seemingly without lunar, martian, or terrestrial analog. Hero Scarp (57° S, 175° W, Figure 5) is a striking example. Roughly 500 km long with an estimated maximum relief of 0.5-1.0 km, Hero rises abruptly at the rim of a 20 km crater near point A (Figure 5b) to cut intercrater plains and four relatively degraded craters (A,B,C,D) ranging in diameter from 25 to 100 km. Inside crater B, a smaller crater roughly 8 km in diameter may also be disrupted, but this relationship is partly obscured in shadow (Figure 5b, arrow). The scarp gives way to a ridge, locally up to 12 km wide, in its midreach (Figure 5b, segment EF). A prominent scarp opposes the ridge's northeastern flank to form a trough roughly 130 km long. To the southeast, Hero gradually loses

its topographic expression before terminating at the rim of a 50 km crater (G). Hero clearly postdates both intercrater plains and several large craters in the area, but may predate craters A and/or G at its endpoints. Combined with the abundance of small craters superposed on the scarp, this suggests that Hero is a relatively ancient feature in the mercurian landscape.

Adventure and Resolution scarps (Figure 6) are other examples of large-scale, arcuate mercurian escarpments. Resolution (62° S, 52° W, Figure 6b, segment AB) rises abruptly at A and cuts intercrater plains for roughly 100 km before it is obscured at B by a broad, complex topographic rise (Figure 6b, FGHI). Stereo photography (Figure 7) suggests that Resolution is topographically continuous with Adventure Scarp to the southwest. Before modification to its present form, an uninterrupted and topographically prominent escarpment presumably cut intercrater plains for 350 km along trace ABCD (Figure 6). This feature is interpreted to have been planimetrically and morphologically similar to Hero Scarp. Adventure (64° S, 63° W, Figure 6b, segment CD) transects intercrater plains and a 60 km crater before terminating roughly 150 km southward in a group of shallow, irregular pits ranging in diameter from 1 to 5 km (Figure 6,D). Maximum relief across these scarps is estimated to be 0.5-1.0 km.

Discovery Scarp (54° S, 38° W) is planimetrically more complex, consisting of two arcuate segments each roughly 200 km long (Figure 8b, AE and FI). The scarp's northern segment is interrupted near the rim of a 50 km crater (Figure 8b, BC), and may be buried by ejecta from that

crater. However, a smaller escarpment which parallels Discovery to the west (Figure 8b, arrows) is also interrupted near a large crater, although the scarp cuts and therefore postdates the crater floor. This suggests that material differences between loose, brecciated ejecta and more competent intercrater plains may account for Discovery's lack of topographic expression along segment BC (Figure 8b).

Two large craters transected by Discovery show no significant morphologic differences across the scarp. Inside the larger crater (Figure 8b, EF), Discovery consists of smaller curved segments 10-15 km long which join to produce a sinuous trace. An opposing, west-facing scarp cuts the smooth floor of this crater to form, with Discovery, a graben-like trough 5-15 km wide. To the south, stereo photography (Figure 9) reveals that intercrater plains immediately east of Discovery slope gently back toward the scarp to form a shallow, asymmetric trough as much as 20 km wide which narrows southward. Discovery in this area (Figure 8b, FH) is compoundly arcuate in plan, with three curved segments each roughly 40 km long. South of its intersection at H (Figure 8b) with a ridge-like lineament, Discovery abruptly changes direction and loses topographic identity at what may be the modified rim of a preexisting crater. Despite appearances in monoscopic images, stereoscopy (Figure 9) reveals that Discovery remains topographically prominent in this southernmost reach (Figure 8b, HI). Absence of a distinct shadow in this area presumably reflects the combined effects of a more sunward trace and slight reduction of slope on the scarp's face.

Throughout most of its length, Discovery is characterized by a rounded brink and convex-upward face which steepens toward a well-defined base to produce an abrupt basal nickpoint. Maximum relief, measured photogrammetrically, is $1.1 \pm .04$ km.

Two relatively small landforms are distinguished by their conspicuous locations near the brink of Discovery Scarp (Figure 10, arrows). Near the midpoint of Discovery's northern arcuate segment, a domical hill with summit depression punctuates the surface immediately above the scarp. This feature is unique in this region, although similar forms are found on smooth plains around Caloris Basin. A shallow, roughly circular depression 15 km in diameter lies perched atop the rounded brink of Discovery near the midpoint of the scarp's southern arcuate segment. This depression resembles numerous other shallow pits developed in mercurian intercrater plains which are unassociated with scarps, suggesting that pits are not genetically related to arcuate escarpments.

Significant horizontal displacement orthogonal to the trace of an arcuate escarpment on Mercury is indicated by offset of the rim of Guido D'Arezzo Crater near 38° S, 19° W (Figure 11). Vostock Scarp rises from the smooth floor of a 75 km degraded crater at A, and transects that crater and Guido D'Arezzo immediately to the southeast before losing its major topographic expression at B, where it intersects a faint N/S trending lineament. Dip slip movement along the scarp has brought into juxtaposition two rim segments of Guido D'Arezzo with significantly different chord lengths, as illustrated in Figure 11b. No evidence exists for significant strike

slip displacement along Vostock Scarp. The observed foreshortening of Guido D'Arezzo crater suggests roughly 10 km of dip slip movement directed roughly N 60°E. Several faint lineaments mark the face of Vostock Scarp to produce a terraced appearance, and an opposing scarp cuts crater floor material for roughly 20 km near Vostock's southern end. (Figure 12, arrows).

Plains to the east and south of Vostock Scarp are cut by numerous large escarpments, most of which are curved in plan with convex traces as viewed from the downward side (Figure 11b). Those not heavily modified have rounded brinks and convex faces which steepen toward the base.

Santa Maria Scarp (6° N, 20° W, Figure 13) consists of alternating linear and arcuate segments which together form an escarpment roughly 230 km long and 200-500 m high. In detail, the scarp's trace is lobated for much of its length. Santa Maria's brink is rounded and in some sections is only poorly defined. Shading suggests that the scarp's face is convex upward in cross-section, steepening from the brink toward an abrupt basal nickpoint. Large craters and intercrater plains cut by Santa Maria in general display no discernible differences across the scarp. There is some suggestion that scarp formation may have induced mass movements from the walls of one transected crater (Figure 13, arrow). There is no evidence of horizontal movement along Santa Maria, although relative displacement by as much as a few kilometers would likely not be discernible in Mariner 10 photography.

Lobate Scarps

A limited number of large, planimetrically lobate scarps cut large craters and intercrater plains on Mercury. The prominent escarpment in Figure 14 is roughly 0.5-1.0 km high and can be traced continuously for nearly 700 km. It consists in part of three roughly linear segments (Figure 14b, AB,CD,DE) which trend N 65° E, N 40° W, N 10° E, respectively.

These linear segments are joined by a less prominent, curved segment (Figure 14b, BC) to produce the lobate outline of the feature as a whole. Several faint lineaments in the area parallel linear segments of the escarpment, suggesting regional structural control of the scarp's outline. Intercrater plains on both sides of the escarpment are relatively flat and punctuated by craters as large as 40 km in diameter.

At higher resolution, (Figure 15), this scarp is seen to consist of curved and angular sections which join to produce a ragged outline in detail. In cross-section, the scarp's face appears more nearly planar than the convex faces characteristic of mercurian arcuate escarpments. Viewed stereoscopically (Figure 16a), the surface immediately behind the scarp's brink is seen to slope gently away from the scarp to form a broad, asymmetric ridge roughly 30 km wide.

North of the lobate scarp, (Figure 15, arrows), parts of an 80 km degraded crater and 200 km double ring basin are obscured by material comprising intercrater plains. These plains are distinguished from smooth floors of the crater and basin, and from surrounding intercrater plains, by the former's irregular, highly pitted surface and lower albedo (Dzurisin, 1976). Stereoscopy (Figure 16b) reveals that

pre-existing crater and basin rims are topographically continuous through the obscured areas, and that the pitted unit is locally elevated above its surroundings. As indicated in Figure 14b, several lineaments within the pitted surface are aligned with linear segments of the major lobate escarpment to the south.

Another large lobate escarpment (Figure 17, FGHI; see also Figure 6) transects Resolution Scarp and crosses several large craters and inter-crater plains. This feature consists of two roughly linear segments (Figure 17b, FG and HI) joined by a curved segment to form a planimetrically lobate outline. The northern linear segment trends N 30°W and is roughly 300 km long, 25 km wide and 500 m high. It is distinguished from arcuate escarpments like nearby Adventure and Resolution Scarps (Figure 17b, CD and AB) by its gentler slope, broader face, and lobated outline in detail. The brink and base of segment FG (Figure 17b) are less well defined than those of typical arcuate scarps, and its face in cross-section is more planar.

A broad discontinuous ridge is visible stereoscopically (Figure 7) immediately behind, and parallel to, segment FG (Figure 17b). The scarp transects and partly obscures Resolution Scarp at B (Figure 17b) and two large craters at G. The obscured crater rim segments can be traced without offset in stereo images (Figure 7), and Resolution is seen to be topographically continuous with Adventure Scarp to the west. Northward, segment FG of the lobate scarp curves sharply west and is superposed by a 25 km crater at F (Figure 17b). It emerges trending

N 130° W and is essentially collinear with an abrupt escarpment cutting the smooth floor of a 45 km crater at E.

The lobate escarpment becomes topographically more pronounced and changes character dramatically to the southwest. Segment HI (Figure 17b) trends N 125° W for roughly 150 km before losing its topographic continuity in a group of morphologically complex scarps and ridges poleward of 75° S latitude. It assumes the topographic form of large arcuate scarps described earlier, and cuts a 50 km crater near H (Figure 17b) without visibly altering surface morphology on either side of the scarp. This is in strong counterdistinction to the scarp's obscuration of transected craters to the north, and is reminiscent of similar crater transections by arcuate escarpments like Discovery and nearby Adventure.

Irregular Intracrater Scarps

Smooth flat floors of many large craters on Mercury are cut by scarps completely confined within the surrounding crater rim. These intracrater scarps are typically 100-500 m high and range in length from a few to in excess of 100 km. They display no consistent planimetric form. Some are essentially linear in plan view, but others are curved or highly complex in detail. For simplicity of presentation, these scarps are collectively grouped here as planimetrically irregular landforms. Descriptions of several representative examples follow.

Scarp AB in Figure 18 cuts the wall and floor of an 80 km crater near 19° S latitude, 31° W longitude. Its face is relatively steep and planimetrically regular, rising roughly 100-300 m above the crater

floor to the south. The scarp curves around a group of peaks near the crater's center, suggesting topographic or structural influence on the scarp's trace by the peaks.

Scarp CD and EG in Figure 18 are planimetrically more linear in large aspect, but less regular on the scale of a few kilometers.

Segment EF traverses the smooth floor of a 90 km crater at 19° S, 27° W for 50 km before abruptly losing much of its topographic expression northeast of its intersection at F with scarp CD. The surface to the NE above scarp CD is distinguished from the remainder of the crater floor by a rougher, textured appearance. Neither scarp can be traced onto the surrounding crater wall. Maximum relief associated with these escarpments is estimated to be 100-200 m.

The escarpment labeled H in Figure 18 and shown at higher resolution in Figure 19 traverses the smooth floor and, atypically, cuts the northern rim of an oblong 30×50 km depression near 20.5° S, 28.5° W. It is paralleled inside the crater by a less pronounced, linear escarpment roughly 15 km to the west. In contrast to its transection of the crater's northern rim, the east-facing scarp abuts and then parallels the southern rim for nearly 20 km. Morphology of the surface cut by these scarps seemingly mimics that of immediately subjacent terrain. Inside the crater, it is relatively smooth with a few superposed craters ranging in size from the limiting resolution of the photographs up to roughly 10 km. Outside the crater rim, it assumes the pitted and highly irregular morphology of surrounding intercrater plains. A well-defined lineament trending N 60° W cuts those plains and a 30 km crater

to the east (Figure 19, arrows). No lateral displacement along this presumed fault trace is evident in the highest resolution (~300 m) images available.

Intracrater features elsewhere on Mercury are planimetrically arcuate or lobate. The arcuate scarp in Figure 20a is roughly 100-300 m high and cuts the floor of a 70 km crater at 30.5°S latitude, 34.5°W longitude. Figure 20b shows several low ridges on the smooth floor of a 85 km crater at 48°S, 19°W, which together define a lobate outline. Two prominent ridge-forms near the crater's southern rim meet at roughly 90 degrees to produce an angular trace in detail (Figure 20b). These intracrater forms are 2 to 5 km wide, with estimated maximum relief of 100-200 m. Shading relationships suggest that most are roughly symmetric in cross-section, implying flanking slopes of 2-10 degrees.

Finally, a few mercurian intracrater scarps bound lobes of material which extend outward from exterior slopes of fresh craters cutting rims of larger, degraded craters (Figure 21). Their morphology and distinctive association with large, overlapping craters suggests that they were produced by impact-induced sliding or flowage of material onto smooth floors of preexisting large craters. They almost certainly owe their origins to impact processes, not volcanism or tectonism, and are included here for completeness only.

Irregular Scarps of the Caloris Region

The Outgoing Quadrant of Mercury photographed by Mariner 10 is dominated by 1300 km Caloris Basin, and by associated plains inside and

outside the basin rim (Trask and Guest, 1975). Smooth plains inside the basin are cut by a complex group of ridges and troughs which define crudely polygonal patterns in plan view. Outside the basin rim, scarps and ridges ranging from planimetrically linear to curved to highly irregular forms cut smooth and hummocky plains units (Figure 4). For simplicity, these scarps, ridges, and troughs are grouped here as planimetrically irregular landforms. Caloris ridges and troughs are treated in subsequent sections on mercurian ridge and trough forms.

Figure 22 shows three high resolution photographs of east-facing scarps which cut smooth plains outside Caloris Basin at 30°N , 158°W ; 25°N , 154°W ; and 19°N , 156°W , respectively. They range from 50 to 100 km in length, and are estimated to be roughly 200 m high. All are roughly concentric with the rim of Caloris Basin to the west. A minor secondary scarp sub-parallel to the major feature bounds a 1-2 km hill in Figure 22b (arrow). The escarpment in Figure 22c divides southward into two scarps, parts of which are ridge-like in cross-section. All three features are characterized by sharp, well-defined bases and narrow (< 300 m), relatively steep faces.

Two west-facing scarps in the Caloris region are shown in Figure 23. The escarpment in Figure 23a cuts Caloris plains and the smooth floor of a 90 km crater without visibly altering surface morphology on either side of the scarp face. Inside the crater, the scarp is sinuous in plan view, with a relatively narrow, roughly planar face in cross-section. It becomes wider and topographically more prominent outside the crater, where its trace curves gently eastward. The scarp gives way to a ridge roughly 12 km wide near its southern end, where it is

superposed by a fresh, 20 km crater. The prominent escarpment in Figure 23b is similar, with a total length of roughly 65 km and estimated height of 100-300m. Planimetrically, this feature resembles Santa Maria Scarp (Figure 13), with two roughly linear segments joined by a curved segment. In cross-section, however, it appears to be distinctly more abrupt than Santa Maria, with a narrower, roughly planar (rather than convex) face.

RIDGES

Linear Ridges

Ridges of significant local relief constitute a small but important fraction of identifiable linear landforms on Mercury. Mirni Ridge at 37°S latitude, 40°W longitude is one example (Figure 24). This major mercurian ridge is planimetrically linear in extent but irregular in detail. At the resolution of available photography (~ 1 km), Mirni appears to start abruptly at the rim of a small crater at its northwest end (Figure 24b, A). It remains linear and continuous for roughly 100 km, gradually increasing in width from 3 to 7 km at point B. Mirni exhibits 0.5-1.0 km of local relief along most of its 350 km length, implying flanking slopes of 5-15 degrees. Near mid-reach, the ridge disrupts the wall and floor of a 45 km crater (Figure 24b, BC). The contact between ridge material and smooth plains flooring the remainder of the crater is sharp, but the temporal relationship between the two is ambiguous. Relative densities of superposed small craters on the plains and ridge as a whole suggest that the ridge predates the plains, however.

Southeast of point C, the feature broadens appreciably to a maximum width of 15 km, then narrows again before transecting a 50 km crater at D (Figure 24b). The ridge trend is seemingly extended southeastward by a series of coalescing pits which rim the crater wall (DE). Segment CD consists of a central, linear, rounded ridge perched atop a broader topographic rise bounded on the northeast by an abrupt escarpment. On the northwest, the transition to intercrater plains appears more gradual,

although this may be an illusion owing to differing lighting conditions.

Segment EF southeast of the second transected crater can be traced for roughly 40 km as a low linear escarpment before it is lost in surrounding intercrater plains. This escarpment and the ridgecrest of segment CD (Figure 24b) are offset roughly 10 km southwestward relative to the remainder of the ridge. Offset occurs along one of several linear scarps and ridges which intersect Mirni Ridge obliquely (Figure 24a, arrows).

A less prominent, much narrower, linear ridge-like form is shown in Figure 25. This NW/SE trending feature can be traced continuously for roughly 40 km (Figure 25b, AB), and extends at least 30 km further southeastward as a faint, discontinuous lineament. It intersects Discovery Scarp near the point where the scarp turns abruptly westward. A linear wall segment of a 40 km crater to the south is aligned with the ridge's trace. Maximum relief exhibited by this linear ridge is estimated to be roughly 100 m.

In addition to ridges developed in mercurian intercrater plains, an extensive system of linear ridges radiate from the rim of Caloris Basin (Figure 26; see also Figure 4). These are surrounded and seemingly embayed by smooth plains which form an annulus around the basin rim (Figures 3a and 4a). A few are relatively broad with flat tops and steep, planimetrically linear flanks. These are typically 5-15 km wide, and extend as projections from large irregular masses elevated above the Caloris smooth plains (Figure 26, arrows). Others further from the basin rim are smaller, with less relief and ragged outlines in detail.

The radial sculpture formed by these ridges extends roughly 1 basin diameter (1300 km) beyond the Caloris rim.

Irregular Ridges

Planimetrically irregular ridges and troughs developed in otherwise smooth plains inside Caloris Basin together form a pattern unlike any associated with other mercurian or lunar basins. Individual ridges differ greatly in plan (Figure 27), but together form a crude polygonal pattern. This pattern consists largely of trends concentric with the basin rim and radial from its center (Figure 4; Strom *et al.*, 1975). Ridges range in width from 1 to 12 km and the most prominent attain heights of roughly 500 m. The largest can be traced continuously for more than 300 km. When ridges inside Caloris are not terminated by fractures or other ridges, they generally narrow along their lengths as they gradually lose their topographic expression. Most are characterized by rounded crests and relatively gentle ($5-10^\circ$) flanking slopes which are convex upward in cross section. A few are topped by irregular troughs aligned along the ridge crests (Figure 27b, arrows).

Most ridges developed in plains outside Caloris Basin are crudely linear in plan, but sinuous or angular in detail (Figure 28). The example in Figure 28a is roughly 300 km long and 20-40 km wide. It transects a 225 km crater flooded by Caloris plains near 24°N latitude, 164°W longitude. The ridge in cross-section consists of a broad, crudely symmetric arch which reaches an estimated maximum height of 200-500 m. Its flanking slopes are relatively gentle ($< 5^\circ$) except near the base of the ridge, where they steepen to form a distinct escarpment perhaps

100 m high. The ridge in Figure 28b is similar in dimension and cross-section, but in plan its base lacks the small scale complexity of the example in Figure 28a. The ridge in Figure 28b turns abruptly 90° to the southeast near the bottom right of the image. Together with several smaller ridges in the area, this angular segment forms a crude rectilinear pattern, with trends radial from the center of Caloris Basin and concentric with its rim. Ridges such as those in Figure 28 are confined to relatively smooth plains around Caloris Basin, and generally do not extend into more heavily cratered terrain further from the basin (Figure 3).

TROUGHS

Linear Troughs

Elongate depressions are relatively abundant on Mercury, and can generally be classed as planimetrically linear or irregular. Linear or slightly curved depressions with scalloped walls and flat floors are widespread. Many are radial to nearby craters and transition into chains of elongate, shallow pits (Figure 29).

Another class of linear troughs is restricted to the hilly and lineated terrain unit mapped by Trask and Guest (1975). They are typically 40-140 km long, 5-15 km wide, and 100-500 m deep (Figure 30). Their walls appear scalloped at low resolution, and more detailed images reveal a series of projecting points and alternating indentations (Figure 31). Most troughs of this type are open-ended and gradually merge longitudinally with surrounding terrain.

Irregular Troughs

Smooth plains flooring Caloris Basin are cut by a group of planimetrically irregular troughs which combine to form a crude polygonal pattern. This pattern is dominated by a strong concentric trend and weaker radial trend (Figure 4; see Strom *et al.*, 1975). Individual troughs range up to 10 km in width and are estimated to be 100-500 m deep. High resolution photographs (Figure 32) reveal that the largest are flat-floored with abrupt, steep sides. Most are topographically closed, although some widen and gradually shallow to form open-ended depressions. In several instances, troughs cut across ridges inside

Caloris Basin (Figure 27a, arrows); the reverse is not observed
(Strom et al., 1975).

LINEAMENTS

Usage of the term "lineament" in this work follows that established by O'Leary et al. (1976): "A lineament is a mappable, simple or composite linear feature of a surface, whose parts are aligned in a rectilinear or slightly curvilinear relationship, and which differs distinctly from the patterns of adjacent features and presumably reflects a subsurface phenomenon." Most linear scarps, ridges, and troughs described earlier were included in global maps of mercurian lineaments shown in Figure 33. Linear troughs and ridges radial from craters and basins, linear segments of large, planimetrically lobate escarpments, and linear albedo markings such as crater rays were excluded.

Rims of many mercurian craters are distinctly polygonal in plan view (Figure 34), and linear segments of these were mapped in Figure 33 and included in azimuth frequency (rosette) diagrams for all mercurian lineaments in Figure 35.

Lineaments are well-developed in all intercrater plains and heavily-cratered regions on Mercury, but largely absent from smooth plains in and around Caloris Basin. Five principal trends can be identified in each latitude band plotted in Figure 35. Except for the trend at N 57°W, the azimuth of each closes toward due north as a function of latitude from equator to south pole. Spacecraft trajectory constraints precluded the acquisition of vertical or near-vertical photography suitable for reliable identification of surface lineaments in the north polar region.

Azimuth of the N 57°W trend remains constant irrespective of latitude. The trend is well developed between 20°N and 20°S, is most pronounced between 20°S and 50°S, and becomes significantly less prominent poleward of 50°S. The area of best development of the N 57°W system is roughly coincident with hilly and lineated terrain as mapped by Trask and Guest (1975), suggesting that hilly and lineated terrain may be genetically related to development or enhancement of the N 57°W lineament system.

SUMMARY**Scarps**

Scarps on Mercury have been grouped as planimetrically arcuate, lobate, or irregular. Large arcuate scarps cut intercrater plains and large craters without otherwise altering surface forms on either side of the scarp trace. They range from 100-500 km in length and are 0.2-1.1 km high. All are convex in plan as viewed from the downward side. Many are planimetrically complex in detail, with sinuous or irregular outlines locally. In cross-section, arcuate scarps are generally convex upward, and steepen from brink to base. Roughly 10 km dip slip displacement along one arcuate scarp is recorded by the offset rim of a transected crater. One example (Vostock) terminates and another (Discovery) abruptly changes direction at intersections with surface lineaments. Only a few large craters superpose mercurian arcuate escarpments, suggesting the scarps formed near the end of heavy meteoritic bombardment.

Large, lobate scarps consisting of two or more linear segments joined by curved segments cross intercrater plains and large craters on Mercury. Such scarps can be traced continuously for as much as 650 km, and are estimated to be 0.5-1.0 km high. One example transects arcuate Resolution/Adventure Scarp and obscures that feature and parts of the rims and floors of two large craters. In stereo images, obscured segments of the scarp and crater rims have topographic expression continuous with their unobscured extensions. Obscuration is not produced

by transection of other large craters by this and other lobate escarpments, which cut crater floors and rims without otherwise altering their morphology.

Escarps on smooth floors of large mercurian craters are typically irregular in plan. A few examples are linear, arcuate, or lobate. Intracrater scarps are tens to more than 100 km long and 100-500 m high. At least two such escarpments continue from crater floors across crater walls, but most do not extend outside craters onto surrounding intercrater plains. In one instance, intersection of two intracrater scarps causes one to become topographically subdued.

Planimetrically irregular scarps developed in Caloris plains are typically 50-100 km long and 100-300 m high. Most are roughly concentric with the rim of Caloris Basin; a few are radial from the basin's center. Some transition into ridge forms longitudinally.

Ridges

Large, planimetrically linear ridges cross intercrater plains on Mercury for hundreds of kilometers. One example disrupts two large craters before giving way to a low, linear escarpment. It consists of a central, rounded ridge roughly 350 km long and 0.5-1.0 km high with low, broad shoulders 20-40 km wide, bounded by relatively abrupt escarpments. A less prominent, much narrower linear ridge roughly 100 m high passes into a faint lineament which intersects arcuate Discovery Scarp near where that scarp abruptly changes direction. Finally, an extensive system of linear ridges radiate from the rim of Caloris Basin. Most

are relatively broad with flat crests and abrupt, planimetrically linear flanks.

On the floor of Caloris Basin, a group of irregular ridges define a crude polygonal pattern consisting largely of trends concentric with the basin rim and radial from the basin center. Most ridges inside Caloris are characterized by rounded crests and gentle, convex flanking slopes. Outside the basin rim, low ridges developed in Caloris plains are crudely linear in plan but irregular in detail. These consist in cross-section of broad, roughly symmetric arches with gentle flanking slopes which steepen near their bases. Most are oriented roughly concentric with the rim of Caloris Basin.

Troughs

Linear to slightly curved elongate depressions with scalloped walls and relatively flat floors are common on Mercury. Many are radial to nearby craters and transition into chains of elongate, shallow pits. Others are restricted to the hilly and lineated terrain unit, and contribute to a well-developed lineament trend in that region.

Inside Caloris Basin, planimetrically irregular troughs up to 10 km wide cut smooth plains to form a crude polygonal pattern dominated by trends radial from the basin center and concentric with its rim. This system of troughs transects a pattern of larger irregular ridges with similar planimetric distribution.

Lineaments

Linear scarps, ridges, troughs and crater wall segments on Mercury together define five principal lineament systems. One system is enhanced

in the hilly and lineated terrain unit, and is constant in azimuth irrespective of latitude. Azimuths of the other four systems close consistently toward north/south as a function of latitude from equator to south pole.

DISCUSSION

The following interpretive sections discuss relevant characteristics and potential origins of mercurian scarps, ridges, troughs, and other lineaments. Alternative explanations are explored, and preferred mechanisms and supporting evidence are identified. Large arcuate escarpments are treated first, followed by a discussion of the global mercurian lineament pattern. Origins of lobate and intracrater escarpments, linear ridges, and linear troughs are addressed in subsequent sections. Non-crater forms of the Caloris region are treated separately, and a speculative scenario for their production is outlined and discussed. A final synthesis section proposes a tentative volcanic/tectonic chronology for Mercury based on observations and interpretations presented earlier.

Arcuate Escarpments

Imposing relief (~1 km) and length (>100 km) of many arcuate escarpments on Mercury, their relatively steep faces, and transectional relationships to large craters support a tectonic origin as proposed by Strom *et al.* (1975). Foreshortening of Guido D'Arezzo crater by Vostock Scarp is interpreted to reflect roughly 10 km dip-slip movement along a thrust or high-angle reverse fault. Combined with arcuate scarps' convex outlines in plan, and convex upward profiles in cross-section, this suggests widespread compression shortly after the end of heavy bombardment on Mercury.

Strom *et al.* (1975) speculated that global compression owing to cooling of a presumed iron core was responsible for formation of

mercurian arcuate escarpments. They showed that a 1-2 km decrease in the mean radius of Mercury was sufficient to explain observed escarpments, and that this was a plausible result of early core cooling. Solomon (1976) suggested that lithospheric cooling was more likely responsible for arcuate scarp formation. He showed that current thermal models of Mercury predict roughly 2 km decrease in mean radius owing to lithospheric cooling after core formation. In either case, compressive stresses induced by shrinkage would be spherically symmetric, producing compressive fractures of random orientation. Tidal despinning by solar torques to reduce Mercury's equatorial oblateness would likewise produce compressive stresses equatorward of roughly 45° , but these would be oriented east-west and produce NW-NE linear shear fractures followed perhaps by north-south trending thrusts or high-angle reverse faults (Melosh, 1976a).

Azimuths of large arcuate scarps on Mercury range from roughly north-south (e.g., Discovery, Santa Maria) to east-west (e.g. Adventure). Maps of arcuate scarps in Figures 2b and 3b reveal no strong directional trends for those features. This is inconsistent with an origin for arcuate scarps through tidal despinning, and supports planetary shrinkage as a viable mechanism for their production. Core or lithospheric cooling is therefore regarded as the most likely explanation for arcuate scarp formation on Mercury. Solomon (1976) suggested that shrinkage began roughly 2 billion years after planetary accretion and continued at essentially a constant rate until present. This is not consistent with observed superposition of arcuate scarps by many craters.

up to 50 km in diameter, which suggests that most arcuate scarp formation occurred relatively early in Mercury's history. Small movements along arcuate scarps may have occurred much later, but available evidence suggests that contraction owing to cooling was largely complete on Mercury soon after the end of heavy bombardment.

Global Lineament System

A wide spectrum of mercurian landforms seemingly reflect structural control by preexisting crustal joints. Linear segments of crater walls have been, in many instances, visibly shaped by mass movements presumably controlled by preexisting linear fractures. Azimuths of linear segments of large lobate escarpments are consistent with trends defined by nearby lineaments, suggesting that the scarps formed along preexisting joints. Linear troughs in the hilly and lineated terrain unit are aligned along trends defined by morphologically diverse lineaments elsewhere. This global pattern of mercurian lineaments (Figures 33 and 35) most likely reflects modification of a global tectonic fabric developed in the early mercurian crust. Structural control of many large, degraded craters and basins with polygonal outlines suggests that the joint pattern was established well before the end of heavy bombardment on Mercury.

Effects of global flexing arising from changes in planetary rotation rate (Esclangon, 1932; Stokyo, 1936; Vening Meinesz, 1947), from movement of a planet's spin axis with respect to its crust (Vening Meinesz, 1947), or from planetary expansion or contraction (Havre, 1931; Usov, 1937) have been proposed to explain planetary lineament patterns.

Uniform planetary expansion or contraction such as might be caused by planetary thermal evolution (Solomon, 1976) is an spherically-symmetric process, and cannot account for preferential orientation of crustal fractures on Mercury. Vening Meinesz (1947) showed that planetary reorientation caused by movement of a planet's spin axis with respect to its surface could produce a pattern of NE and NW trending linear shear fractures, qualitatively consistent with that observed on Mercury. A possible cause of spatial reorientation of Mercury is basin excavation by large impacts. Isostatic rebound and probable extrusive igneous activity initiated by the basin forming event would allow tidal friction to eventually nearly restore Mercury's original orientation, however (Melosh, 1975). Crustal fractures established by temporary reorientation would be shifted as Mercury reassumed its original orientation. In this model, the symmetry and present orientation of well-developed NW and NE trends on Mercury would be fortuitous.

Flexing owing to tidal spindown is a process likely to have affected Mercury, and it more easily explains the planet's observed lineament pattern. Goldreich and Soter (1966) have shown that the present 2/3 spin-orbit resonance of the mercurian orbit (rotational period = 56.6 days; orbital period = 88 days) is a likely consequence of tides raised on Mercury by the Sun. For reasonable values of the planetary dissipation constant ($Q \sim 50$) and initial rotation period ($P_0 \sim 19$ hrs.), Mercury would despin to its present rotation rate in roughly 1 b.y.

Burns (1976) and Melosh (1976a) have studied stresses and associated fractures induced by tidal despinning. For a range of plausible planetary models, spindown induces compressive azimuthal (east-west) stresses

which always exceed induced meridional (north-south) stresses. For a planet with a thin (< 200 km) lithosphere, theory predicts stress differences up to several kilobars, sufficient to cause failure of terrestrial-type crustal rocks. Shear fractures begin at the equator where stress differences are largest. Laboratory studies of shear failure in terrestrial rocks predict linear fractures trending roughly N60°W and N60°E, in reasonable agreement with well developed lineament trends near the mercurian equator (Figure 35).

Poleward of roughly 45° latitude, theory predicts east-west trending tensional features which are not seen. These can be suppressed by a uniform compression caused by a slight (.1-.2%) decrease in planetary radius during the despinning process (Melosh, 1976a). It was inferred above that large arcuate escarpments on Mercury record such a compressional period. If compression continued after Mercury had been substantially despun, net horizontal compressive stresses may have exceeded vertical stresses, thereby causing arcuate thrust or high-angle reverse faults. At this point, if azimuthal stresses induced by despinning dominated those induced by uniform compression, resulting fractures would define a crude north-south (N45°W-N45°E) pattern. If uniform compressive stresses dominated, azimuths of induced fractures would be randomly distributed (Melosh, 1976a). The latter situation is favored for Mercury, where large arcuate scarps are randomly oriented. In either case, linear shear fractures would predate thrust or high-angle reverse faults. This is true for Mercury, where the pattern of linear crustal joints clearly predates many large polygonal craters,

and large arcuate scarps transect and therefore postdate most large craters.

In summary, tidal despinning and slight global contraction successfully explain the existence, orientation, and planimetric distribution of most lineaments on Mercury. This hypothesis explains the existence, orientation, and planimetric distribution of mercurian arcuate scarps, interpreted as thrust or high-angle reverse faults formed in response to compressional stresses induced primarily by global contraction. It further predicts the observed temporal relationship between mercurian arcuate scarps and lineaments. It fails to explain poorly developed N-S and N-NE global trends, and most trends' systematic shift toward due north with latitude from equator to south pole. This may reflect deficiencies in the model's analytic form, or unmodeled properties of the mercurian lithosphere. Nevertheless, qualitative agreement between theory and several key observations suggests that tidal despinning and global contraction have played important roles in shaping the mercurian landscape.

Lobate Scarps

Azimuths of linear segments of large, planimetrically lobate escarpments on Mercury (Figures 14-17) are consistent with trends defined by nearby lineaments (Figure 35), suggesting structural control of the scarps' planimetric forms. Combined with the scarps' steep faces and large dimensions, this suggests that they record regional uplift along a preexisting system of crustal joints.

The Gray Mountain segment of the East Kaibab Monocline provides a terrestrial example of this type of tectonic landform. The monocline extends roughly 250 km from the San Francisco Peaks volcanic field, Arizona, north across the Grand Canyon and along the east side of the Kaibab Plateau to Bryce Canyon National Park, Utah (Figure 36). It is downthrown 0.4-1.5 km on the east side. Associated graben, faults, and aligned cinder cones together define distinct N, NW, and NE trends (Babenroth and Strahler, 1945). E.M. Shoemaker (personal communication, 1976) suggests that these relationships reflect structural control by linear faults which cut Precambrian basement beneath the Colorado Plateau.

The planimetrically lobate Gray Mountain segment of the East Kaibab Monocline (Figure 37) consists of two roughly linear parts, each approximately 30 km long. These join to form a single escarpment roughly 0.5 km high. The East Kaibab Monocline as a whole is comparable in size, and its Gray Mountain segment is similar in configuration, to large lobate escarpments on Mercury (Figures 14-17). The relationship of the East Kaibab Monocline to displacements along preexisting linear fractures suggests that a similar origin may apply to the mercurian features. Displacements on Mercury may have been in response to stresses induced by large basin formation (Schultz and Gault, 1975), by planetary cooling (Solomon, 1976), or by tidal despinning (Burns, 1976; Melosh, 1976a).

Obscuration of topographically continuous segments of two large craters and an arcuate escarpment by the northern segment of a lobate escarpment in Figure 17 distinguishes that segment from its westward

extension and from the lobate scarp shown in Figures 14 and 15. The northern segment's broad, planar face, gentle slope, and lobated outline in detail further distinguish it from planimetrically arcuate mercurian escarpments. Satisfactory explanation of this unique escarpment is a necessary part of any successful theory for lobate scarp formation on Mercury.

The distinctive character of the lobate escarpment in Figure 17 may be a primary feature of its mode of origin, or it may reflect modification of what was once a more typical mercurian scarp form. A potential explanation of the first type is that obscuration was produced by ground motion along a low-angle thrust fault which intersects the surface at FBGH (Figure 17b; Malin, 1976). In this view, segments AB, CD, and HI may represent transverse tear faults formed in response to eastward thrusting of the block bounded at E-I. Marked differences in small-scale planimetric outline, transverse slopes, and transectional relationships to large craters between N-S trending and E-W trending segments are interpreted to reflect differences between dip-slip motion on the thrust fault and strike-slip motion on the tear faults.

Although this scenario successfully explains the overall character of features in Figure 17, it has several shortcomings in detail. Topographic continuity of obscured crater rims with their unobscured extensions requires that horizontal movement on the presumed thrust fault has been relatively minor. Lack of discernible offset of large craters near D and H (Figure 17b) indicates that strike-slip movement

on presumed tear faults has likewise been small. It seems unlikely that ground motion associated with such minor thrusting could be responsible for intense modification of obscured landforms. Similar obscuration is never associated with large arcuate scarps on Mercury even though dip-slip movement on one example (Vostock) has foreshortened a large crater by roughly 10 km. Finally, this model does not explain the planimetrically linear front of the hypothesized thrust sheet, or the arcuate traces in plan of presumed tear faults at AB and CD (Figure 17b).

An alternate explanation for the escarpments in Figure 17 attributes the unique character of segment FGH to secondary modification of a preexisting scarp form. (Malin, 1976). In this view, the present lobate form in Figure 17 was originally analogous to the lobate escarpment in Figures 14 and 15. Both formed by uplift along intersecting linear elements of the global mercurian joint pattern. The arcuate escarpment in Figure 17 was at that time continuous and similar in form and origin to Hero Scarp (Figure 5). Segment FGH of the lobate scarp (Figure 17) later provided surface access for volcanic material which superposed parts of the arcuate scarp and two large craters, thereby subduing their morphology. The preexisting lobate scarp caused materials emplaced to the east to form a gentle ramp to surrounding intercrater plains. Accumulation along linear vents produced a low, discontinuous ridge at the top of that ramp, near the original trace of the lobate escarpment. Stereo images suggest that erupted material conformed in large part to underlying topography. This suggests that volcanic ash, not lava, may have been the primary erupted constituent.

This tectonic/volcanic scenario is consistent with the general character of the landscape in Figure 17, and also explains: 1) the arcuate trace in plan of scarp ABCD (Figure 17b); 2) the lobate trace of scarp FGHI and the trends of segments FG and HI; 3) obscuration of parts of an arcuate escarpment and two large craters; and 4) marked differences in transectional relationships to large craters between segments FG and HI (Figure 17b). Potential shortcomings include:

- 1) absence of associated volcanic landforms such as cones or domes;
- 2) similar small crater densities (implying similar ages) on inter-crater plains throughout the region; and 3) lack of a discernible western boundary to hypothesized volcanic deposits originating from vents near segment FG (Figure 17b). Nevertheless, volcanic modification of preexisting landforms successfully explains many key observational constraints, and is regarded to be a more promising hypothesis than purely tectonic origin for the features in Figure 17.

Obscuration of parts of a 200 km double ring basin and 80 km crater in Figure 15 may also reflect burial by volcanic materials. Lineaments within the obscuring material contribute to the global pattern, and may be crustal fractures which served as vents for plains-forming eruptions. The suggestion by Malin (1976) that this relationship could reflect intense surface modification preferentially on one side of tectonic escarpments is regarded as unlikely, for reasons outlined earlier. In

this case, obscuring material is distinguished from its surroundings by the former's lower albedo (Dzurisin, 1976) and highly pitted, irregular surface. Differences in composition and texture may account for this distinction, and are consistent with a volcanic origin for obscuring material.

Irregular Intracrater Scarps

Strom *et al.* (1975) suggested that most intracrater scarps on Mercury are fronts of relatively viscous volcanic flows extruded from vents on large crater floors. They cited as supporting evidence restriction of scarps to crater floors, diversion of an intracrater scarp around central peaks (Figure 18 AB), and an inferred mantling relationship at the intersection of two intracrater scarps (Figure 18, F). Those authors further suggested that the irregular escarpment in Figure 19 most likely bounds a volcanic flow, since it abuts and then parallels a crater wall.

It was noted earlier, however, that the scarp diverted around central peaks in Figure 18 continues onto the surrounding crater wall at both ends. This is clearly inconsistent with an origin by extrusion from vents on the crater floor. Extrusion from vents on the crater walls is also precluded, because terraces immediately below the scarp trace on opposite sides of the crater show no evidence of being overrun by lava. In addition, sources on the east and west walls could

not explain preferential accumulation of lava on the northern crater floor. A tectonic origin is therefore favored for this intracrater scarp.

It was noted above that the surface above the irregular escarpment in Figure 19 mimics that of immediately subjacent terrain, changing from smooth and flat inside the crater to pitted and irregular in adjacent intercrater plains. If this escarpment bounds a volcanic flow, then the flow is draped over and preserves underlying topography. This seems unlikely, because relief of the scarp exceeds that of pits and knobs in nearby intercrater plains. A more plausible explanation is that the feature is a tectonic escarpment which cuts crater floor material and intercrater plains without otherwise modifying the surface morphology of either. Thus, two intracrater scarps cited by Strom et al. (1975) as examples of potential volcanic flow fronts are more likely of tectonic origin.

Finally, the mantling relationship involving two intracrater scarps (Figure 18, CD and EFG) invoked by Strom et al. (1975) to support a volcanic origin for those escarpments can also be understood if both scarps are tectonic features. In this view, faulting first elevated the northeastern part of the crater floor to produce scarp CD (Figure 18). This was followed by flooding of the southwestern portions of the crater to a level somewhat below the brink of scarp CD. Differences between brecciated crater floor material and competent volcanic flows account for the distinction in surface morphology between parts of the crater floor separated by scarp CD. Finally, faulting along

EFG (Figure 18) produced a second escarpment which cut across scarp CD, but was poorly preserved in brecciated floor material northeast of point F. Evidence for poor preservation of tectonic escarpments in brecciated material elsewhere on Mercury was presented in an earlier discussion of Discovery Scarp.

In summary, several intracrater scarps on Mercury are demonstrably of tectonic origin, and no example exists which requires an alternate, perhaps volcanic, explanation. Tectonism is thus the preferred mechanism for production of most mercurian intracrater scarps. Restriction of scarps inside craters may indicate that stress fields responsible for scarp formation were local in extent and centered below the confining craters. Deformation of crater floors may have resulted from intrusion of magma into, or withdrawal of magma from, impact-produced breccia underlying large craters. Schultz (1974) concluded that many floor-fractured craters on the Moon have been deformed tectonically during mare formation. Although mercurian floor-fractured craters do not resemble their lunar counterparts in detail, the hypothesis of mare-like, plains-forming volcanism on Mercury as outlined by Murray et al. (1975) and Strom et al. (1975) suggests that a similar model may apply to Mercury.

Linear Ridges

The azimuth of linear Mirni Ridge (Figure 24) is aligned with a global N57°W. lineament trend, suggesting structural control of the ridge trace. The feature could not have been produced by surface modification of a linear fault scarp, since no net vertical displacement

occurs across the ridge. The ridge's setting in an expanse of otherwise undisturbed intercrater plains, and its extremely large length/width ratio suggest that it is probably not a fault block (horst). Tectonic folding seems an unlikely cause for the same reasons.

If the ridge has evolved from an original crustal fracture, then one plausible but speculative explanation of its present form invokes lava extrusion to form an accretionary ridge along the trace of the fracture. This mode of origin is consistent with: 1) agreement between the ridge's azimuth and a global lineament trend at N57°W; 2) partial obscuration of a large preexisting crater by the ridge; and 3) symmetry of the ridge in cross-section. Flanking slopes of 5-15 degrees along the ridge are comparable with slopes of terrestrial basaltic shields such as Mauna Loa on Hawaii, suggesting that formation of Mirni Ridge by lava extrusion would not require unreasonable composition and/or viscosity for mercurian magma. The series of coalescing pits along the trace of the ridge may be endogenic collapse features analogous to terrestrial pit craters in volcanic areas. Finally, a group of smaller linear ridges and scarps which intersect the large ridge obliquely and offset it near mid-reach may be younger en echelon faults, some of which have served as extrusion sites. These do not fit the global lineament pattern shown in Figure 35, and hence may be relatively local features created in response to ridge formation.

The narrow, linear ridge-form in Figure 25 is similarly best understood as a volcanic feature. If mercurian intercrater plains reflect early resurfacing of most of the planet by volcanic materials

(Trask and Guest, 1975; Murray et al., 1975), preexisting crustal fractures probably served as conduits for transport of such material to the surface. This suggests that ancient dikes which served as feeders for fissure eruptions during intercrater plains formation may be relatively common on Mercury. The ridge form in Figure 25 is roughly 40 km long, perhaps 100 m high, and is part of a well-developed global lineament trend. The feature's extremely small width/length ratio and the lack of similar landforms nearby suggest that the ridge did not form through regional folding or faulting (i.e. horst formation). It resembles in scale and morphology some of the largest dikes exposed on Earth, such as those associated with eroded Tertiary volcanic complexes in Britain (Richey, 1948). Erosion to expose the mercurian feature may have been associated with formation of the hilly and lineated terrain unit to the northeast. Where it is best developed, this unit is characterized by intense modification of preexisting landforms (Trask and Guest, 1975). Scarcity of exposed dikes on Mercury may reflect resolution constraints of available photography, or may indicate that post-intercrater plains erosion on most of Mercury has been relatively minor (see Malin and Dzurisin, 1976). Alternatively, most mercurian intercrater plains may have formed by crustal melting (Murray et al., 1975; Malin, 1976) rather than by extrusion from depth.

Linear Troughs

Linear to slightly curved closed depressions with scalloped walls, many of which are radial from large craters and transitional into discrete, slightly elongate pits (Figure 29) resemble similar depressions on the Moon (Figure 38). They most likely represent

coalesced secondary craters formed by impact of associated clumps of debris ejected from large primary impacts (Shoemaker, 1962; Gault et al., 1975). Most isolated examples not clearly associated with nearby large craters are probably secondary chains from remote impacts, although alternate tectonic, volcanic, or erosional origins for some cannot be ruled out.

Linear troughs in mercurian hilly and lineated terrain also have scalloped walls, and high resolution photographs of Arecibo Valley reveal a series of projecting points and alternating indentations suggestive of sculpturing by mass movements. Azimuths of these troughs are in every case consistent with trends of the global lineament pattern, even though a few are seemingly radial from large craters (Figures 30, 33, 35). This suggests that the orientations of most troughs in hilly and lineated terrain reflect structural control by linear crustal joints.

Strom et al. (1975) proposed that these troughs are graben formed in response to regional tensional stresses. However, Trask and Guest (1975) noted that many crater rims in the area have been broken up into hills and depressions, suggesting intense modification by some erosional process. It seems likely that the same erosional process may have attacked nearby crustal joints to produce the observed pattern of linear troughs. In this view, troughs are secondary erosional landforms created by preferential erosion along preexisting fractures. A few may be secondary crater chains modified by the process responsible for development of hilly and lineated terrain.

Rejuvenation of crustal fractures by tensional stresses is neither required nor precluded. This interpretation is favored over extensional faulting because it invokes only observed modification of preexisting surface features, and does not require an unobserved and unspecified source of tensional stress restricted to hilly and lineated terrain.

Resolution constraints in available photography preclude unambiguous identification of the specific erosional process responsible for hilly and lineated terrain. Schultz and Gault (1975) suggested that antipodal focusing of seismic energy derived from the Caloris impact may have been responsible for development of hilly and lineated terrain. Local rejuvenation of preexisting fractures by this mechanism may account for enhancement of the N57°W lineament trend in the area. However, erosive capability of impact-induced shaking is difficult to evaluate. Photographs of the eastward extension of hilly and lineated terrain beyond the evening terminator seen by Mariner 10 may be required to further specify the source of intense surface modification recorded by this distinctive terrain unit.

Scarps, Ridges, and Troughs of the Caloris Region

Plains in and around 1300 km Caloris Basin on Mercury are crossed by numerous scarps, ridges, and troughs of diverse morphologies. These landforms are treated together because their close geographic association with Caloris suggests a common genetic link to the basin-forming event. Linear ridges radiating from the Caloris rim are discussed first, followed by a unified treatment of planimetrically irregular scarps, ridges, and troughs developed in smooth plains in and around the basin.

I. Linear Ridges Outside Caloris Basin

A system of ridges radiating from the rim of Caloris Basin (Figures 4 and 26) is reminiscent of similar forms around Imbrium and Orientale basins on the Moon (Figure 39). Faulting and sculpturing by basin ejecta are two currently favored mechanisms believed responsible for ridge and trough formation around lunar basins. Melosh (1976b) has suggested from theoretical considerations that stress relaxation associated with basin excavation could produce radial tensional joints extending several radii from basin rims. Vertical movement on such joints could account for some linear ridges around Caloris, but the ragged and discontinuous outlines of most suggest an alternate, non-tectonic origin. Embayment by younger smooth plains of material ejected radially by the Caloris impact is one plausible explanation. In this view, radial ridges are the unflooded remnants of a radial ejecta facies around Caloris which was originally similar in form to well-documented radial facies around other mercurian and lunar basins (Gault *et al.*, 1975). Alternatively, the ridges may be erosional remnants of a surface sculptured by low-angle ballistic ejecta or gas-charged fluidized ejecta (Eggleton and Schaber, 1972) associated with the Caloris impact. Subsequent flooding by smooth plains could then have produced the morphologies and embayment relationships seen in Figure 26. In either case, deposition or erosion associated with the Caloris basin-forming event is regarded to be more consistent with the morphology of these ridges than a purely tectonic explanation.

II. Irregular Scarps, Ridges, and Troughs of the Caloris Region

Planimetrically irregular ridges and troughs inside Caloris Basin are judged to be most likely of tectonic origin. Erosion along pre-existing zones of weakness to produce troughs, or around relatively competent areas to produce ridges, is an alternate explanation. However, craters of comparable age on Caloris plains show no evidence of shallowing since formation (Malin and Dzurisin, 1976), indicating that only mild erosion has occurred in the Caloris region since smooth plains emplacement. Other explanations include cooling fractures and pressure ridges in volcanic materials. These are common features in terrestrial lava flows, but they do not attain the dimensions of troughs and ridges inside Caloris.

From transectional relationships between ridges and troughs, and from photometric evidence suggesting a significant slope inward toward the center of Caloris, Strom et al. (1975) inferred that regional subsidence produced radial and concentric compressive stresses responsible for the pattern of ridges inside the basin. Subsidence was followed in their model by central uplift to produce a pattern of extensional fractures. Although it is non-unique, the following generalized model for subsidence followed by uplift successfully accounts for the morphology, orientation, and relative age of features developed on the floor of Caloris Basin.

Murray et al. (1975) concluded from crater frequency relationships that some smooth plains outside Caloris are younger than the basin and smooth plains comprising its floor. Accordingly, they rejected the

suggestion that smooth plains outside Caloris were emplaced as fluidized ejecta from the basin-forming event, and opted for later volcanic emplacement. Subsidence owing to magma withdrawal from beneath Caloris Basin to form smooth plains outside may have caused surface buckling under compressive stresses to form radial and concentric ridges on the basin floor. These ridges resemble many lunar mare ridges in large aspect, lacking only the central highly deformed crests seen on many lunar examples (Figure 40). Conel (1969) cited truncation of a 600 m crater at the base of a mare ridge in Mare Humorum as evidence for the ridge's tectonic origin, and concluded that some mare ridges formed by surface buckling in response to compressive stresses. A similar origin may apply to the ridges inside Caloris. Planimetrically irregular scarps and ridges outside Caloris Basin may have formed when newly-emplaced volcanic plains subsided under their own weight (see Maxwell et al., 1975; Bryan, 1973; Baldwin, 1963).

Finally, irregular troughs inside Caloris may be extensional fractures formed in response to central uplift caused by isostatic readjustment to basin excavation. There is theoretical evidence (Baldwin, 1963) that mass deficiencies caused by excavation of large basins on the Moon may have been at least partly compensated by upward movement of relatively high density mantle material. Several authors have suggested that large positive gravity anomalies over some lunar basins are best explained by models including such mantle response (Bowin et al., 1975; Wise and Yates, 1970). This subsurface mass redistribution would likely produce uplift of overlying surface materials in an area roughly confined to the basin rim. Resulting

tensional stresses would produce extensional fractures if the strength of near surface materials was exceeded. Absence of similar trough patterns in lunar basins may reflect rheologic differences between lunar and mercurian mantle materials, which determine the rate of mantle response to basin excavation. Alternatively, temporal relationships between basin formation, mantle response, and basin filling may have differed on the two bodies.

In summary, the following speculative sequence is qualitatively consistent with morphologic observations and planimetric distribution of scarps, ridges, and troughs in and around Caloris Basin. The pattern of irregular ridges inside the basin probably formed in response to regional subsidence, perhaps caused by magma withdrawal from beneath Caloris. Surface extrusion of that magma outside Caloris soon after basin formation formed smooth plains which subsided under their own weight to produce radial and concentric scarps and ridges. Finally, uplift within Caloris caused by subsurface mass redistribution in response to basin excavation may have produced a pattern of extensional fractures which cut preexisting ridges.

SYNTHESIS

This final section summarizes preferred mechanisms for formation of scarps, ridges, troughs, and other lineaments on Mercury, and outlines a tentative chronology for that planet's surface evolution (Figure 41). Genesis mechanisms are in many instances nonunique, and alternate explanations are not precluded. The chronology is offered as a working hypothesis to serve as a framework for future topical studies of mercurian non-crater landforms.

After formation of a solid lithosphere on Mercury, but before the end of heavy meteoritic bombardment, tidal spindown and global contraction owing to cooling combined to produce a global pattern of linear crustal joints. Contraction continued after Mercury had been substantially despun, inducing large compressive stresses responsible for development of planimetrically arcuate thrust or high-angle reverse faults. Final movement along these fractures post-dated the formation of most large craters. Stresses induced by tidal spindown, planetary cooling, or large impacts locally rejuvenated elements of the global tectonic fabric to uplift areas between intersecting linear joints. The resulting escarpments assume a lobate outline in plan view. Mass movements from crater walls originated along elements of the global joint system to produce craters with linear wall segments and, in some instances, with polygonal outlines.

Throughout this period, intercrater plains formed by extrusion from linear crustal fractures or by local surface melting. Accumulation

of volcanic materials along some fractures created large linear ridges. Erosion subsequently exposed linear dikes which served as feeders for plains-forming fissure eruptions. Superposition of large craters and arcuate escarpments by intercrater plains is rare, suggesting that most intercrater plains were emplaced before the end of heavy bombardment and before most arcuate scarp formation.

The Caloris basin-forming event was a significant milestone in the surface evolution of Mercury. Deposition of, or erosion by, ejected material produced a pattern of linear ridges which radiate from the basin rim. Soon after basin excavation, fluid material covered its floor to form smooth plains. Volcanic extrusion from depth is the preferred mechanism for emplacement of these plains, although impact generated melt and ejecta fallback are plausible alternatives. A system of planimetrically irregular ridges inside Caloris probably formed in response to compressive stresses owing to regional subsidence, perhaps induced by magma withdrawal from beneath to form younger volcanic plains outside the basin rim. Gravitational readjustment to emplacement of plains material outside Caloris may be responsible for scarp and ridge formation there. Finally, continuing isostatic adjustment to basin excavation may have caused central uplift of plains inside Caloris to produce a system of extensional fractures which transect the previously established pattern of ridges.

At roughly the same time, intense modification of preexisting landforms occurred in a region roughly antipodal to Caloris Basin to produce a distinctive terrain unit characterized by scattered hills and large,

linear, open-ended troughs with scalloped walls. Preferential erosion along preexisting lithospheric fractures is the mechanism preferred for linear trough formation.

Planimetrically irregular scarps and ridges developed in smooth plains inside craters are relatively young, tectonic landforms formed in response to local stresses, perhaps induced by subsurface magma movements. The period since smooth plains emplacement on Mercury has apparently been characterized by relatively light cratering and only mild landform degradation.

Preservation of clues to this tortuous history on the present surface of Mercury suggests that similar processes may have acted on other terrestrial bodies. Recently acquired Viking photographs of Mars can provide an important observational test of the tidal spindown hypothesis for creation of planetary lineament patterns. Mars has presumably not been spun down by solar torques (Goldreich and Soter, 1966), and therefore should not exhibit a consistent pattern of surface lineaments similar to that identified on Mercury. Earth, however, has certainly been substantially despun through tidal interactions with its moon. Careful examination of the effect of continental drift is required before evidence for a terrestrial tectonic fabric can be reliably evaluated. If arcuate escarpments on Mercury formed in response to planetary cooling and contraction, their absence on the Moon and Mars has implications for relative thermal evolution on those bodies. Comparative studies of Caloris and similarly-sized lunar basins may shed additional light on the origin of basin-associated scarps, ridges,

and troughs, and on such fundamental questions as the relative importance of volcanic filling and mantle rebound as sources for positive gravity anomalies over lunar basins. Finally, comparisons of generalized evolutionary histories for Mercury, Mars, and the Moon may eventually provide important insights into the early evolution of our turbulent Earth.

REFERENCES

- Arthur, D.W.G., (ed.) The System of Lunar Craters, Quadrant I, Contrib.
Lunar and Planet. Lab (Univ. Ariz.) No. 3, 1963.
- Babenroth, D.L. and A.N. Strahler, Geomorphology and Structure of the
East Kaibab Monocline, Arizona and Utah, Geol. Soc. Am. Bull., 54,
107-150, 1945.
- Baldwin, R.B., The Measure of the Moon, University of Chicago Press,
Chap. 9, pp. 188-196, 1963.
- Bowin, C., B. Simon, and W.R. Wollenhaupt, Mascons: A Two-Body Solution,
Jour. Geophys. Res., 80, 4947-4955, 1975.
- Bryan, W.B., Wrinkle Ridges as Deformed Surface Crust on Ponded Mare
Lava, Proc. Lunar Sci. Conf. 4th, 93-106, 1973.
- Burns, J.A., Consequences of the Tidal Slowing of Mercury's Rotation,
Icarus, 28, 453-458, 1976.
- Conel, J.E., Structural Features Relating to the Origin of Lunar Wrinkle
Ridges, Space Programs Summary 37-56, v. III, Jet Propulsion Labora-
tory, Pasadena, CA., pp. 58-63, 1969.
- Dzurisin, D., Geologic Significance of Photometric Variations on Mercury,
Ph.D. Thesis, Part 2, California Institute of Technology, 1976.
- Eggleton, R.E. and G.G. Schaber, Cayley Formation Interpreted as Basin
Ejecta, Apollo 16 Prelim. Sci. Rept., NASA SP-315, 29-7-29-16, 1972.
- Esclangon, E., Remarques au Sujet de la Note de M.N. Stokyo, "Sur les
de'placements périodiques des continents," Comptes rendus Acad. Sci.
Paris, 194, 2227, 1932.

- Gault, D.E., J.E. Guest, J.B. Murray, D. Dzurisin, M.C. Malin, Some Comparisons of Impact Craters on Mercury and the Moon, Jour. Geophys. Res., 80, 2444-2460, 1975.
- Goldreich, P., and S. Soter, Q in the Solar System, Icarus, 5, 375-389, 1966.
- Havre, N., Le Terre est un Astre Pulsatile, Béranger, Paris and Liege, 80 pp., 1931.
- Malin, M.C., Observations of Intercrater Plains on Mercury, Geophys. Res. Letters, 3 (in press), 1976.
- Malin, M.C. and D. Dzurisin, Landform Degradation on Mercury, the Moon, and Mars: Evidence from Crater Depth/Diameter Relationships, J. Geophys. Res., 1976 (in press).
- Maxwell, T.A., Farouk El-Baz, and S.H. Ward, Distribution, Morphology, and Origin of Ridges and Arches in Mare Serenitatis, Geol. Soc. Am. Bull., 86, 1273-1278, 1975.
- Melosh, H.J., Mascons and the Moon's Orientation, Earth and Planetary Sci. Lett., 25, 322-326 (1975).
- Melosh, H.J., Global Tectonics of a Despun Planet, submitted to Icarus, 1976a.
- Melosh, H.J., On the Origin of Fractures Radial to Lunar Basins, Proc. Lunar Sci. Conf. 7th, in press, 1976b.
- Murray, B.C., R.G. Strom, N.J. Trask, D.E. Gault, Surface History of Mercury: Implications for Terrestrial Planets, J. Geophys. Res., 80, 2508-2514, 1975.

O'Leary, D.W., J.D. Friedman, H.A. Pohn, Lineament, Linear, Lineation:
Some Proposed New Standards for Old Terms, Geol. Soc. Am. Bull.,
87, 1463-1469, 1976.

Pike, R.J., Depth/Diameter Relations of Fresh Lunar Craters: Revision
from Spacecraft Data, Geophys. Res. Letters, 1. (7), 291-294, 1974.

Pohn, H.A. and T.W. Offield, Lunar Crater Morphology and Relative Age
Determination of Lunar Geologic Units - Part I: Classification,
U.S. Geol. Surv. Prof. Paper 700-C, 153-162, 1970.

Richey, J.E., British Regional Geology, Scotland: The Tertiary Volcanic
Districts, 2nd ed., His Majesty's Stationery Office, Edinburgh,
1948.

Schultz, P.H., Floor- Fractured Lunar Craters, Lunar Science V,
681-683, 1974.

Schultz, P.H. and D.E. Gault, Seismic Effects from Major Basin Formation
on the Moon and Mercury, The Moon, 12, 159-177, 1975.

Sharp, R.P., Mars: Troughed Terrain, Jour. Geophys. Res., 78, 4063-4072,
1973a.

Sharp, R.P., Mars: Fretted and Chaotic Terrains, Jour. Geophys. Res., 78
4073-4083, 1973b.

Sharp, R.P., Mars: South Polar Pits and Etched Terrain, Jour. Geophys.
Res., 78, 4222-4230, 1973c.

Sharp, R.P., and M.C. Malin, Channels on Mars, Geol. Soc. Am. Bull., 86,
593-609, 1975.

Shoemaker, E.M., Interpretation of Lunar Craters, in Physics and
Astronomy of the Moon, ed. Z. Kopal, Chap. 8, pp. 283-359, 1962.

Solomon, S.C., Some Aspects of Core Formation in Mercury, Icarus, 28
509-522, 1976.

Stokyo, N., Sur L'Irregularité de la Rotation de la Terre, Comptes Rendus
Acad. Sci. Paris, 203, 39, 1936.

Strom R.G., N.J. Trask, J.E. Guest, Tectonism and Volcanism on Mercury,
J. Geophys. Res., 80, 2478-2507, 1975.

Trask, N.J. and J.E. Guest, Preliminary Geologic Terrain Map of Mercury,
J. Geophys. Res., 80, 2461-2477, 1975.

Ussov, M.A., Compression and Expansion in the History of the Earth,
Internat. Geol. Cong., 17th Sess. (Leningrad), Abstr. Papers, 1,
144, 1937.

Vening Meinesz, F.A., Shear Patterns of the Earth's Crust, Trans.. Geol.
Soc. Am., 28, 1-61, 1947.

Wise, D.V. and M.T. Yates, Mascons as Structural Relief on a Lunar
"Moho", Jour. Geophys. Res., 75, 261-268, 1970.

FIGURE CAPTIONS

Part 1

Figure 1 - These examples of mercurian scarps, ridges, and troughs illustrate a classification system for noncrater landforms based on planimetric form. Scarps on Mercury are grouped as planimetrically arcuate (A), lobate (B), or irregular (C). Mercurian ridges and troughs are generally linear (D,F) or irregular (E,G) in plan view. Combined with descriptions of detailed morphology and transectional relationships, this scheme effectively distinguishes several landform types suitable for independent discussion and interpretation. Where present, arrows mark the trace of the feature under consideration. For these and all subsequent Mariner 10 images, FDS 26000-28000 = Mercury I Incoming; FDS 0-100 = Mercury I Outgoing; FDS 164000-169000 = Mercury II; FDS 526000-530000 = Mercury III.

Figure 2 - (a) This mosaic of Mariner 10 images shows the Incoming Quadrant of Mercury photographed by the spacecraft during its first encounter with the planet on March 29, 1974. Mean resolution of individual frames comprising the mosaic ranges from 1-3 km. The evening terminator occurs at roughly 11°W longitude in this view. The prominent rayed crater near the center of the mosaic is 65 km Kuiper Crater.

Figure 2 - (b) Map showing the orientation and distribution of scarps, ridges, and troughs in the Incoming Quadrant of Mercury (Figure 2a). See key for explanation of map symbols.

Figure 3 - (a) Photomosaic of Mariner 10 images of the Mercury I Outgoing Quadrant, with 1300 km Caloris Basin near the equator and bisected by the morning terminator ($\sim 191^{\circ}$ W longitude). Mean photographic resolution is roughly 2 km.

Figure 3 - (b) Map of scarps, ridges, and troughs in the Outgoing Quadrant of Mercury, illustrating the predominance of trends radial from the center of Caloris Basin (inset) and concentric with the basin rim. Note the absence of planimetrically arcuate escarpments (line and barb symbol; see key) developed in relatively smooth plains in and around Caloris. The area designated Caloris Plains in the figure includes smooth plains, hummocky plains, and Caloris lineated terrain units of Trask and Guest (1975).

Figures 2b and 3b, Key - Explanation of map symbols used in Figures 2b and 3b.

Figure 4 - (a) Mosaic of high resolution (0.3-1.0 km) Mariner 10 images of 1300 km Caloris Basin. An intricate system of well-developed ridges and troughs developed in otherwise smooth plains inside the basin is clearly visible. Note also the pattern of ridges which radiate outward from the basin rim, best developed in the upper right of the image.

Figure 4 - (b) Maps of scarps, ridges, and troughs in the Caloris region of Mercury by Strom et al. (1975). Note the predominance of trends radial from the basin center and concentric with its rim at all scales and for each landform type. Strom et al. (1975) indicate that relative crater ages portrayed in the figure are based on local superpositional and transectional relationships.

Figure 5 - (a) Large arcuate escarpment which crosses relatively smooth plains and transects several large craters near 57° S, 173° W. Mariner 10 FDS 166842.

(b) Sketch map of above, showing the major escarpment (line and barb) giving way to a ridge in midreach (EF). Arrow indicates smaller crater (~ 10 km) which may be disrupted by the escarpment. Lines with bar and ball mark nearby, less prominent escarpments developed in relatively smooth polar plains (pp). Crater symbols $c_5 - c_1$ indicate relative crater morphology, with c_5 = freshest and c_1 = most degraded. This scheme is not intended to strictly reflect relative crater age.

Figure 6 - Photomosaic (a) and sketch map (b) of a region centered near 63° S, 55° W. Note the interruption at B of arcuate Resolution Scarp (AB) by a broader, lobate escarpment marked FGHI. Adventure Scarp (CD), roughly 125 km west of Resolution, continues that scarp's arcuate trend, and

Figure 6 - stereo images (Figure 7) reveal that the two are topographically continuous along obscured segment BC. Polar plains = pp, intercrater plains = ip. Mariner 10 FDS 166614 and 166620.

Figure 7 - Stereo images of the Adventure/Resolution region of Mercury, showing that those scarps are subdued but topographically continuous through an area bounded by part of a broader, planimetrically lobate escarpment in the upper right portion of the photographs. Note also the continuity of a large (~80 km) crater rim transected and obscured by the lobate escarpment near the upper right corner. A low, linear ridge is developed in plains immediately behind this segment of the lobate scarp. Apparent relief is greatly exaggerated; maximum relief of Adventure and Resolution scarps is estimated to be 0.5-1.0 km. Mariner 10 FDS 166679 (left) and 27403 (right).

Figure 8 - Computer-generated photomosaic (a) and sketch map (b) of compoundly arcuate Discovery Scarp and surrounding terrain. Discovery crosses intercrater plains for nearly 500 km, and transects large craters near D and E without otherwise altering their morphology. Arrows indicate a less prominent, subparallel escarpment which is well developed in intercrater plains (ip) and floor material of a 130 km crater, but loses its topographic expression in the crater's continuous ejecta deposits. Interruption of Discovery Scarp between points B and C may likewise reflect material differences between

Figure 8 - intercrater plains and crater ejecta. Mosaic includes
(cont.) Mariner 10 FDS 528881-528884, 27386, 27393, 27398, and
27399.

Figure 9 - Stereo images of the southern arcuate segment of Discovery Scarp. Plains immediately southeast of the escarpment are seen to slope gently toward the scarp face to form a broad, asymmetric trough. Note the abrupt change in direction of the scarp's trace at its intersection with a ridge-like lineament near the bottom right of the images. Mariner 10 FDS 166613 (left) and 27399 (right).

Figure 10 - Mercury III high resolution frame 528884 of central Discovery Scarp. Upper arrow indicates domical hill with central depression perched near the brink of the scarp. Lower arrow shows irregular, rimless depression with smooth floor which occupies a similar position with respect to Discovery. Photographic resolution (2 picture elements) is roughly 700 m.

Figure 11 - Mariner 10 frame 27380, centered near 38° S, 19° W, provides evidence of roughly 10 km dip-slip movement along Vostock Scarp (AB), as recorded by the foreshortened rim of Guido D'Arezzo Crater in the upper left portion of the image. Vostock seemingly loses much of its topographic expression at its intersection with a north-trending lineament at B. Nearby escarpments developed in intercrater plains material (ip) are curved in plan view, and some have convex-upward

Figure 11 - faces in profile which steepen from brink to base. Most (cont.) arcuate scarps on Mercury exhibit similar characteristics.

The southernmost extension of highly modified hilly and lineated terrain (hlt, see Trask and Guest, 1975) is visible in the upper part of the frame.

Figure 12 - High resolution view (FDS 27464) of Vostock Scarp inside Guido D'Arezzo Crater, with arrows to terrace-like lineaments developed on the scarp face. An irregular escarpment opposes Vostock near its brink in the southern part of the crater. Note scattered hills and highly modified escarpments which characterize the hilly and lineated terrain unit extending into the frame from the north.

Figure 13 - Santa Maria Scarp. Note alternating linear and curved segments, and lobated trace of the scarp in detail. Rounded brink and abrupt basal nickpoint are characteristic of large, arcuate escarpments on Mercury. Arrow marks crater wall material which may have been mobilized by scarp formation. Picture width = 240 km; north approximately toward top; FDS 27448.

Figure 14 Mosaic (a) and sketch map (b) of Mariner 10 FDS 166590 and 166591. Arrows mark trace of large, planimetrically lobate escarpment which crosses intercrater plains (ip) for roughly 500 km. Linear segment CD is roughly parallel to a distinct lineament which intersects a degraded 80 km crater 100 km to the northeast, and segment DE is roughly collinear with a

Figure 14 - north-trending lineament extending from the northern rim
(cont.) of a double-ring basin near the top of the image. Azimuths
of segments AB, CD, DE, and both lineaments are consistent
with trends defined by a global system of lineaments.
Note obscuration of southern rim of the double-ring basin,
shown at higher resolution in Figure 15.

Figure 15 - High resolution view of planimetrically lobate escarpment
and surrounding intercrater plains. Note angular to
irregular outline of the scarp in detail. Arrows to
obscured segments of a 200 km double-ring basin and 80 km
crater. Obscuration occurs in plains material characterized
by highly pitted surface and seemingly lower albedo
relative to nearby intercrater plains and smooth plains
inside the basin. Mariner 10 FDS 166649 and 166650.

Figure 16 - Stereo images of large lobate escarpment and partly obscured
double-ring basin. Note that the basin rim is topographi-
cally continuous through the visually obscured area. Plains
immediately behind the lobate escarpment are seen to slope
gently down from the scarp brink to form a broad asymmetric
ridge. (a) Mariner 10 FDS 166649 (left) and 166591 (right).
(b) FDS 166649 (left) and 27301 (right).

Figure 17 - Photomosaic and sketch map of a planimetrically lobate
escarpment which transects arcuate Resolution Scarp near
62°S, 53°W (B). The escarpment is interrupted by a younger,
25 km crater at F, but transects and obscures two larger
craters near G. Segment FG forms the boundary between

Figure 17 - intercrater plains (ip) and less heavily cratered polar (cont.) plains (pp) to the east. This reach of the lobate scarp is characterized by a broad, gently-sloping face and lobated outline in detail. The scarp becomes more prominent and changes character to the southwest, where it exhibits a steeper, convex-upward face in profile. Segment HI cuts a 50 km crater near H without otherwise modifying the crater's morphology. Mariner 10 FDS 166679 and 166686.

Figure 18 - Mariner 10 frame 27428, with four examples of planimetrically irregular intracrater scarps on Mercury. Scarp AB in the upper left cuts crater wall and floor material of an 80 km crater, and diverts around a group of central peaks. Scarp EG cuts smooth plains inside a 90 km crater to the east. It loses much of its topographic expression northeast of its intersection at F with scarp CD. Note the difference in surface roughness between crater floor materials separated by scarp CD. The escarpment labeled H is atypical in that it begins in smooth intracrater plains, but continues across the crater rim into surrounding intercrater plains. A high resolution view of this example is provided in Figure 19.

Figure 19 - This high resolution (~300 m) Mariner 10 image shows an irregular escarpment which cuts smooth crater floor material and surrounding intercrater plains. The scarp parallels the crater's southern rim for nearly 20 km before swinging

Figure 19 - north across the crater floor. It crosses the northern
(cont.) rim of the crater without interruption, then gradually diminishes. A less prominent, west-facing scarp opposes the main feature inside the crater to form a flat-topped ridge roughly 20 km wide. Note that the morphology of plains immediately behind the larger escarpment mimics that of immediately subjacent terrain. Arrows mark prominent lineament which cuts a degraded crater in the upper right.

Mariner 10 FDS 27471.

Figure 20 - (Left) Planimetrically arcuate escarpment cutting smooth plains material inside a 70 km crater in the Incoming Quadrant of Mercury. (Right) Group of low ridges developed in smooth plains on the floor of an 85 km crater, which together form a crude lobate outline. Note the angular trace in detail of the ridge near the craters southern rim.

Figure 21 - Three examples of intracrater escarpments which bound lobes
(cont.) of material extending outward from exterior slopes of fresh craters that cut rims of large, degraded craters. This material has apparently been mobilized by flowage or sliding across flat floors of large craters by subsequent impacts on their rims.

Figure 22 - Scarps cutting Caloris plains. These east-facing escarpments cut relatively smooth plains which form an annulus around 1300 km Caloris Basin to the west. All are roughly concentric with the basin rim. Arrow in (b) marks a low

Figure 22 - secondary escarpment at the base of a rounded hill.

(cont.) Strom et al. (1975) note that the large escarpment in (b) forms the boundary between smooth plains to the west and smooth plains with scattered hills to the east. (a) FDS 44; (b) FDS 47; (c) FDS 49.

Figure 23 - (a) Mosaic of Mariner 10 FDS 60 and FDS 63, showing a prominent west-facing escarpment cutting Caloris plains and smooth floor material of a 90 km crater. Note change in morphology as the feature crosses the crater's southern rim. Outside the crater, the scarp gives way to a broad ridge roughly 12 km wide near its southern end. Where it cuts smoother plains inside the crater, the feature is narrower and topographically less prominent with a sinuous trace in plan view. Mass movement features are clearly visible on the wall and floor of a fresh, 20 km crater which interrupts the feature near the bottom of the image.

(b) This escarpment developed in Caloris plains is roughly 65 km long and 100-300 m high, with an abrupt, seemingly planar face. The rim of Caloris Basin is roughly 380 km to the west of the scarp. Mariner 10 FDS 72.

Figure 24 - Mirni Ridge. This planimetrically linear feature consists of a broad, rounded ridge which disrupts two large craters (BC and DE) before giving way to a low escarpment southeastward (EF). Maximum relief is estimated to be 0.5-1.0 km. Note the chain of coalescing pits which rim a 50 km crater

Figure 24 - (DE) transected by Mirni. Arrows indicate two low ridges (cont.) (left) and two escarpments (right) which intersect the central ridge obliquely. The ridge crest is seemingly offset roughly 10 km southwestward along the scarp marked by the third arrow from the left. Mariner 10 FDS 27420.

Figure 25 - (a) A narrow, NW/SE trending linear ridge is marked by arrows in this enlargement of Mariner 10 frame 27399. The ridge can be traced for roughly 40 km, and its trend is extended an additional 30 km southeastward by a low, irregular escarpment. Discovery Scarp abruptly changes direction near its intersection with the projected trend of the linear ridge.
(b) Sketch map of image at left, showing southern arcuate segment of Discovery Scarp (arrow), and narrow linear ridge with nearby escarpments (AB).

Figure 26 - Group of broad, flat-topped ridges radiating from north-eastern rim of Caloris Basin (rim at lower left). Arrows mark linear ridge segments which extend from large irregular masses of material embayed by relatively smooth Caloris plains. Mariner 10 FDS 193.

Figure 27 - (a) Mariner 10 frame 106 showing plains inside Caloris Basin with planimetrically irregular ridges and troughs. Some troughs transect ridges (arrows), but the reverse is not observed.

Figure 27 - (b) Southeastern floor of Caloris Basin, with well-developed
(cont.) pattern of irregular ridges and troughs. Arrows mark
ridges with troughs at their crests. Mariner 10 FDS 110.

Figure 28 - Ridges developed in plains outside Caloris Basin. The example in (a) is morphologically similar to many lunar mare ridges, lacking only the narrow crestal ridge seen on many lunar examples (see Figure 40). The ridge in (b) is dimensionally and morphologically similar, but in detail lacks the planimetric complexity of the ridge in (a). Both consist in cross-section of broad, crudely symmetric arches which reach maximum heights of 200-500 m, and steepen in profile from crest to base. Upper image = Mariner 10 FDS 191; lower image = FDS 120.

Figure 29 - These Mariner 10 photographs include examples of linear, topographically closed depressions which commonly radiate from fresh mercurian craters, and presumably owe their origin to secondary impacts. Note the progression outward from basin rims in (b) from linear troughs with scalloped walls, to elongate depressions formed by coalescing pits, to groups of discrete pits radial from basin rims. Top image of Kuiper Crater = mosaic of FDS 27362 and 27363; bottom = orthographically projected version of FDS 150.

Figure 30 - Intense modification of preexisting landforms to produce scattered hills and linear, open-ended troughs characterizes this distinctive terrain unit which extends from

Figure 30 - roughly 20° S to 40° S and from 35° W eastward into the
(cont.) evening terminator (11° W) as photographed by Mariner 10.

High resolution views presented in Figure 31 are outlined in white.

Figure 31 - Two high resolution views of linear troughs developed in the hilly and lineated terrain unit. Arrows mark alternating projections and indentations suggestive of mass movements from trough walls. Left (Arecibo Valley) = FDS 528848; right = FDS 27422.

Figure 32 - High resolution (~800 m) Mercury III image of planimetrically irregular troughs developed in plains inside Caloris Basin. Note steep walls and seemingly flat floors which characterize most troughs not obscured by shadows. Most examples narrow and become less deep near their ends. The prominent trough slightly above and left of center curves markedly as it cuts across a smaller, linear ridge. Mariner 10 FDS 529055.

Figure 33 - (a) Mercurian lineaments - Incoming Quadrant. Map includes most planimetrically linear scarps, ridges, troughs, and crater wall segments. Scarps confined inside craters, troughs radial from craters, and linear segments of lobate escarpments were excluded. Azimuth-frequency diagrams are provided in Figure 35.

(b) Mercurian lineaments - Outgoing Quadrant. Note relatively poor development in Caloris Plains. As outlined

Figure 33 - here, Caloris Plains includes smooth plains, hummocky plains, (cont.) and lineated terrain units as mapped by Trask and Guest (1975).

Figure 34 - Examples of mercurian craters with distinctly polygonal outlines, presumably reflecting structural control by preexisting lithospheric fractures. Top = FDS 74; bottom = FDS 27427.

Figure 35 - Azimuth-frequency (rosette) diagrams of mercurian lineaments in three latitude bands. Incoming and Outgoing Quadrants were combined to improve statistics; no large differences were observed when quadrants were plotted separately. Upper, solid portions show total number of lineaments in each 5° azimuth band; total length of lineaments (km) in each band is plotted in the lower, stippled portions. $N57^{\circ}W$ trend remains constant in azimuth irrespective of latitude. Its region of best development coincides with that of the hilly and lineated terrain unit in the Incoming Quadrant. Four other trends close consistently toward north-south as a function of latitude from equator to south pole.

Figure 36 - Generalized map of East Kaibab Monocline, after Babenroth and Strahler (1945). Arrow indicates Gray Mountain segment shown at higher resolution in Figure 37.

Figure 37 - Enlargement of Landsat image showing planimetrically lobate Gray Mountain segment of East Kaibab Monocline (arrows). Compare with lobate mercurian escarpment shown in Figures 14 and 15. Babenroth and Strahler (1945) note that associated graben, faults, and aligned cinder cones together define distinct N, NW, and NE trends which reflect Precambrian basement structure. Colorado River and Grand Canyon are at top, cones of the San Francisco Peaks volcanic field near Flagstaff, Arizona are visible at lower right. Landsat image E-1104-17382-7 01, MSS Band 7.

Figure 38 - High resolution Lunar Orbiter IV image of northeastern Copernicus, illustrating outward progression from linear troughs to coalescing secondary pits to distinct craters radiating from the central, primary crater. Compare with mercurian examples in Figure 29. Lunar Orbiter IV frame 121 H2.

Figure 39 - Comparison of 1300 km Caloris Basin on Mercury (left) and 900 km Orientale Basin on the Moon. Note radial facies immediately outside the most prominent rim in both cases. Large ridges are seemingly better developed in the mercurian example, but this may reflect in part embayment by younger Caloris plains which emphasizes high-standing terrain. Deposition of, or erosion by, low-angle ejecta is the preferred mechanism to explain radial sculpture in both cases. Left = mosaic of Mariner 10 Outgoing frames;

Figure 39 - right = Lunar Orbiter IV frame 186M. Images are to same scale; north is approximately toward top.

Figure 40 - (a) Oblique view of southwestern Mare Imbrium looking north across a series of mare ridges and young lava flows. Note the central, narrow ridges developed at the crests of broader, rounded arches which are roughly symmetric in profile. Apollo 15 metric camera frame AS-15-1554.

Figure 40 - (b) Vertical view of mare ridges in Mare Serenitatis. With exception of narrow crestal ridge, note similarity to mercurian example in Figure 28a. Apollo 17 metric camera frame AS-17-0599.

Figure 41 - Generalized outline of mercurian surface evolution as inferred from studies of scarps, ridges, troughs, and other lineaments. Lengths of individual lines are not intended to indicate absolute time; lines illustrate sequential relationships only. Relative timescale at the bottom is entirely qualitative, and is included only to suggest that much of mercurian surface evolution outlined above occurred relatively early in the planet's history.

SCARPS

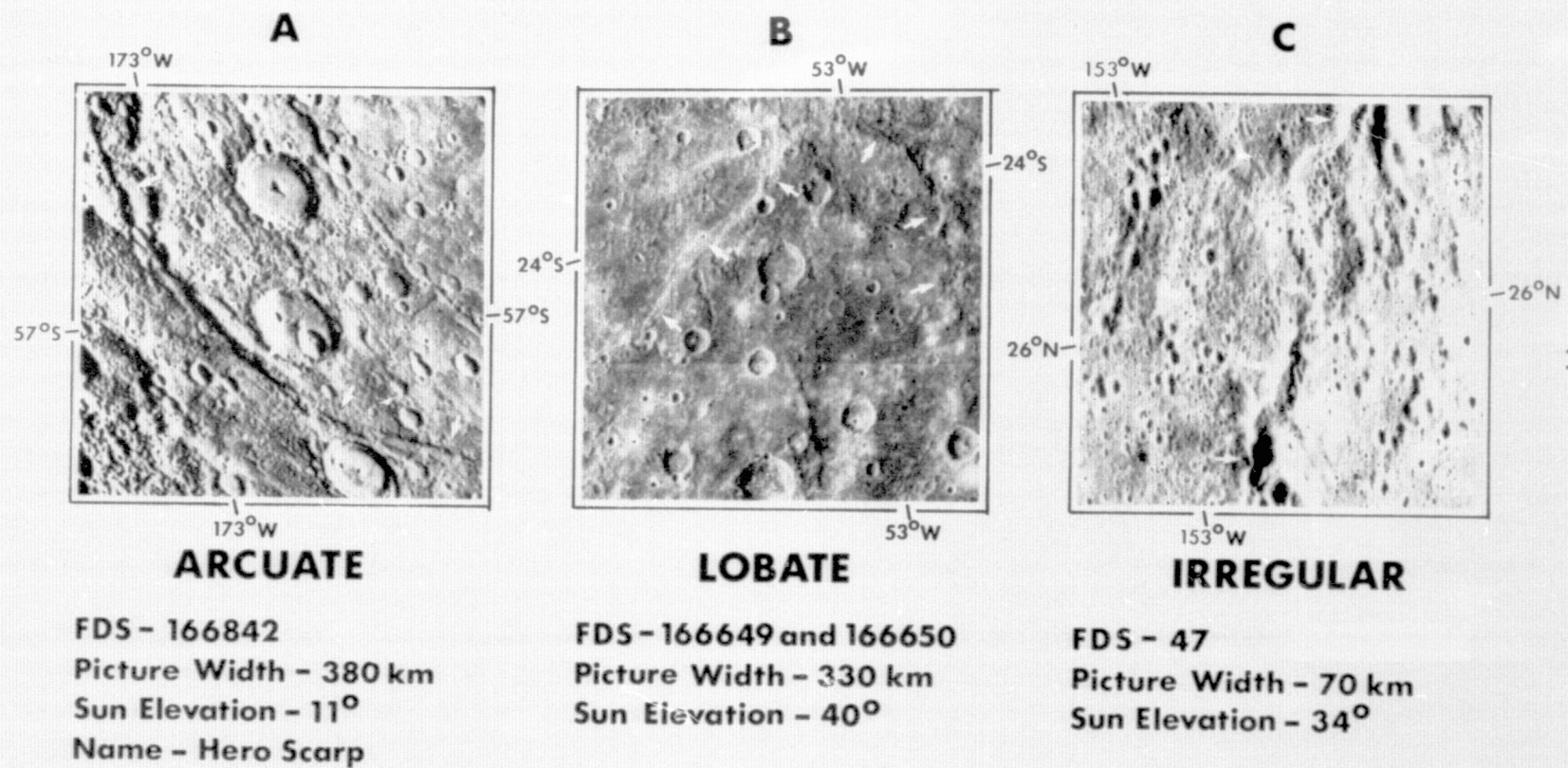
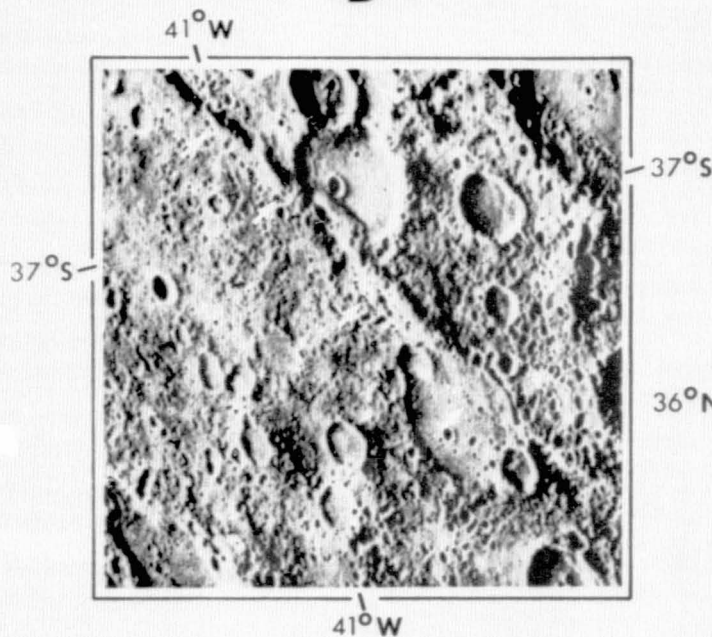


Figure 1

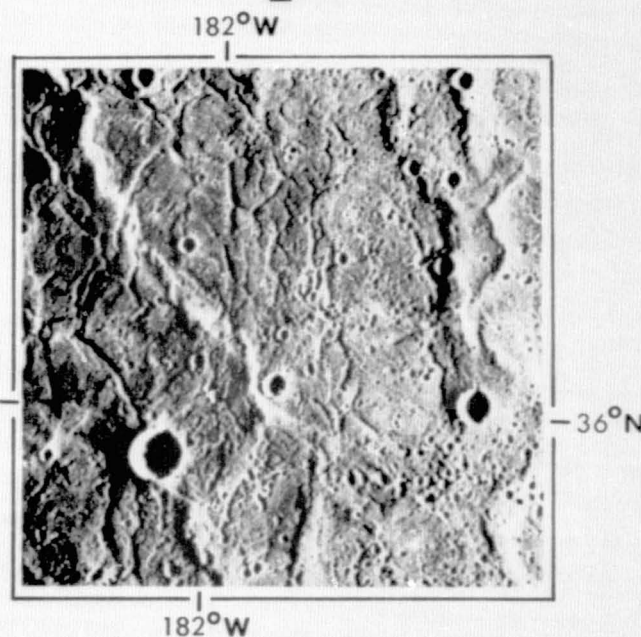
RIDGES

D



LINEAR

E



IRREGULAR

FDS - 27420

Picture Width - 250 km

Sun Elevation - 26°

Name - Mirni Ridge

FDS - 106

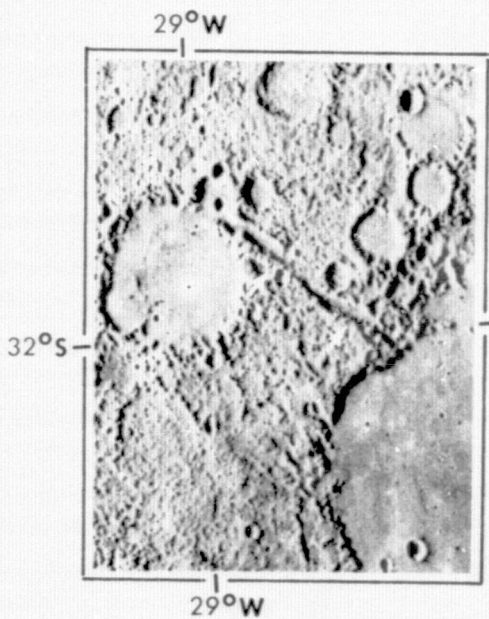
Picture Width - 160 km

Sun Elevation - 9°

Figure 1

TROUGHS

F



LINEAR

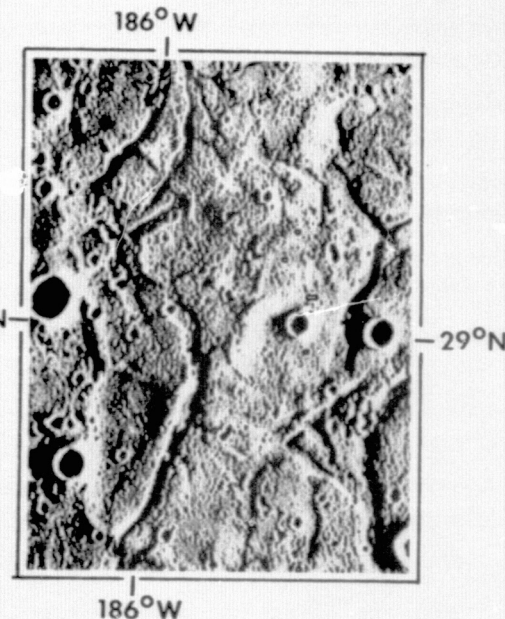
FDS - 27370 and 27371

Picture Width - 315 km

Sun Elevation - 19°

Name - Arecibo Valley

G



IRREGULAR

FDS - 529055

Picture Width - 95 km

Sun Elevation - 4°

Figure 1

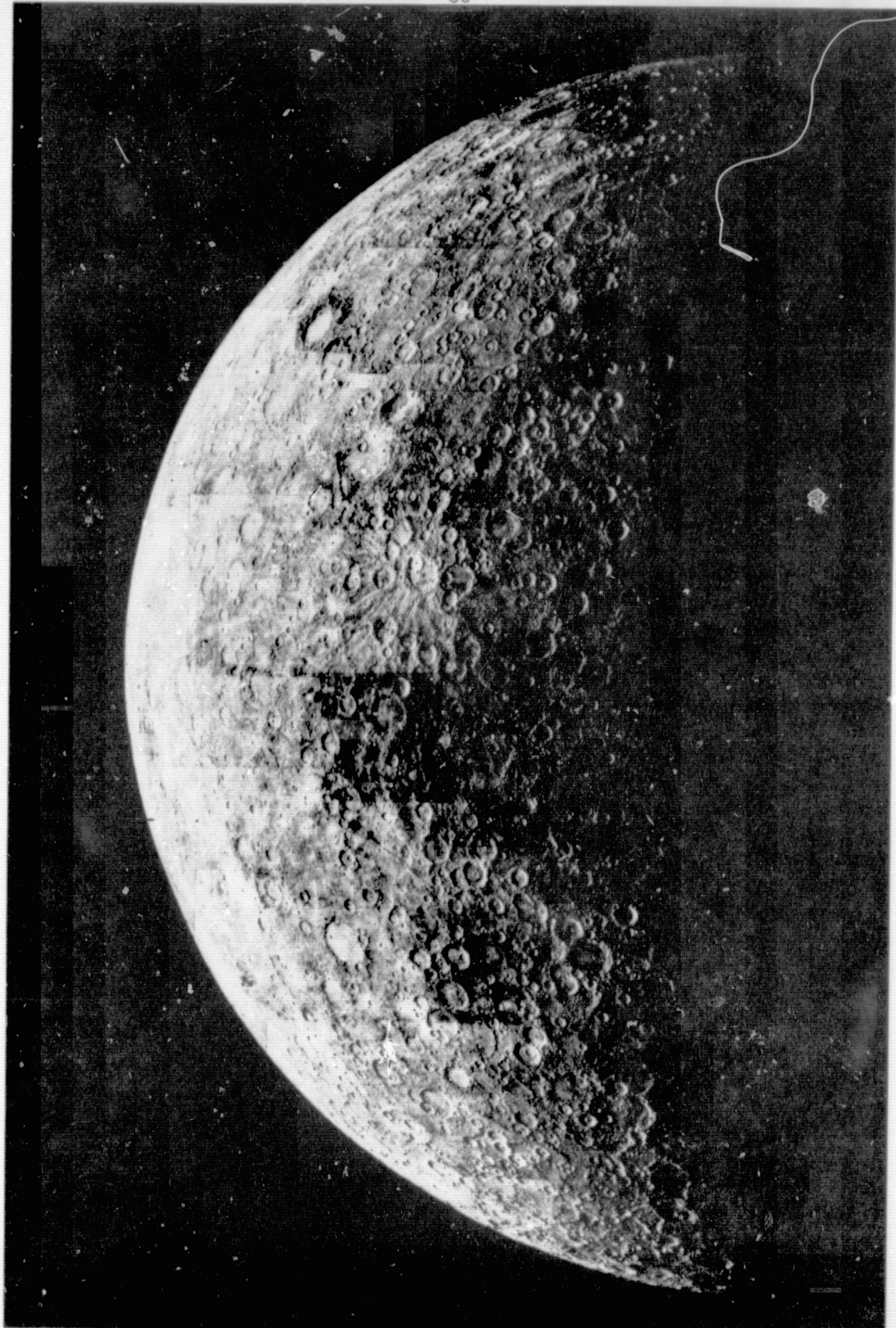


Figure 2a

SCARPS, RIDGES, and TROUGHS Incoming Quadrant

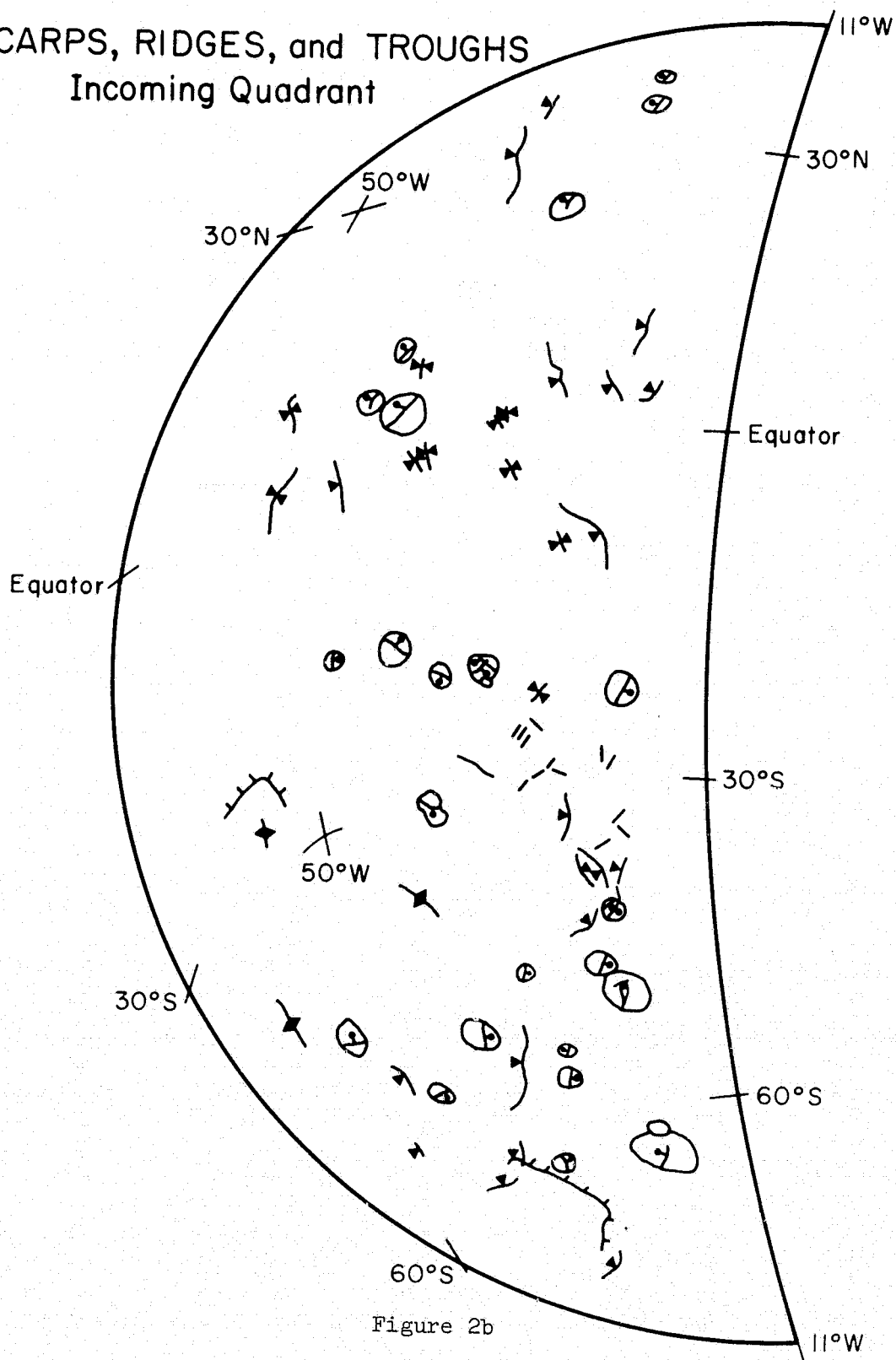


Figure 2b

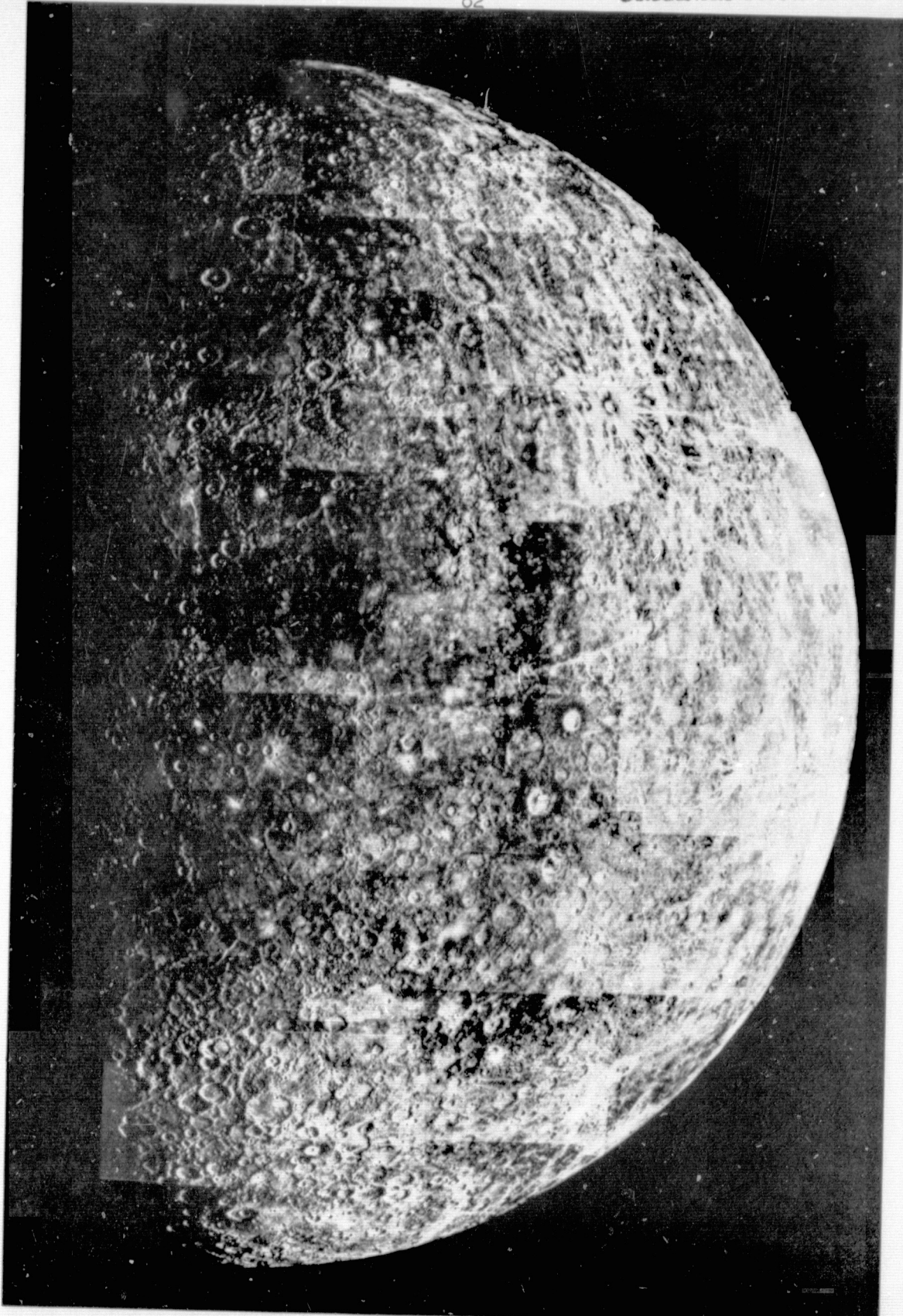
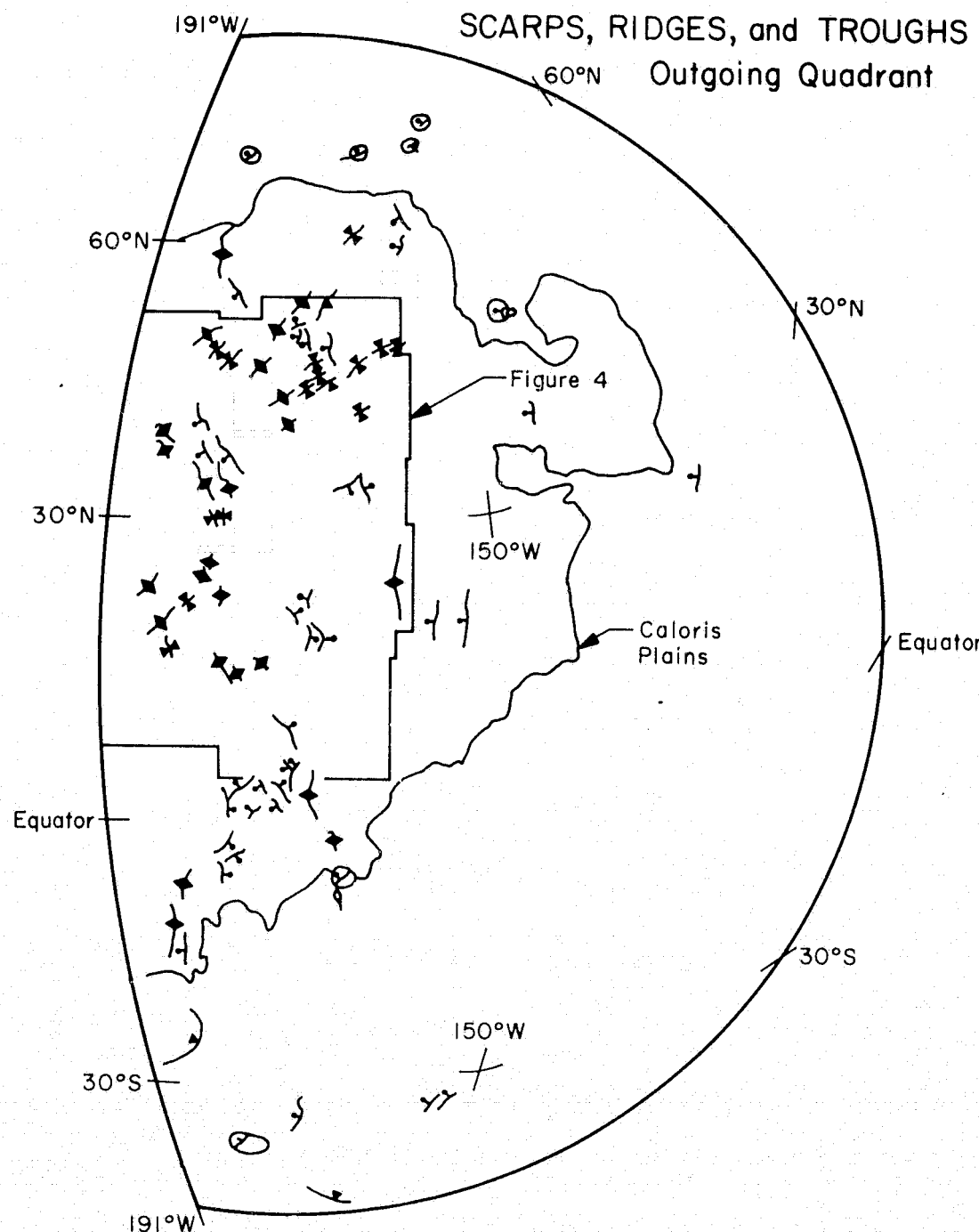


Figure 3a



84
KEY

Figures 2b and 3b

SCARPS



Arcuate

*Line at base of scarp
Barb points downslope*



Lobate

*Line at base of scarp
Hachures on down side*



Irregular

*Line at base of scarp
Bar and ball on down side*



Irregular Intracrater

RIDGES



Linear

Line marks crest



Irregular

TROUGHS



Linear

Line marks center



Linear

Hilly and lineated terrain

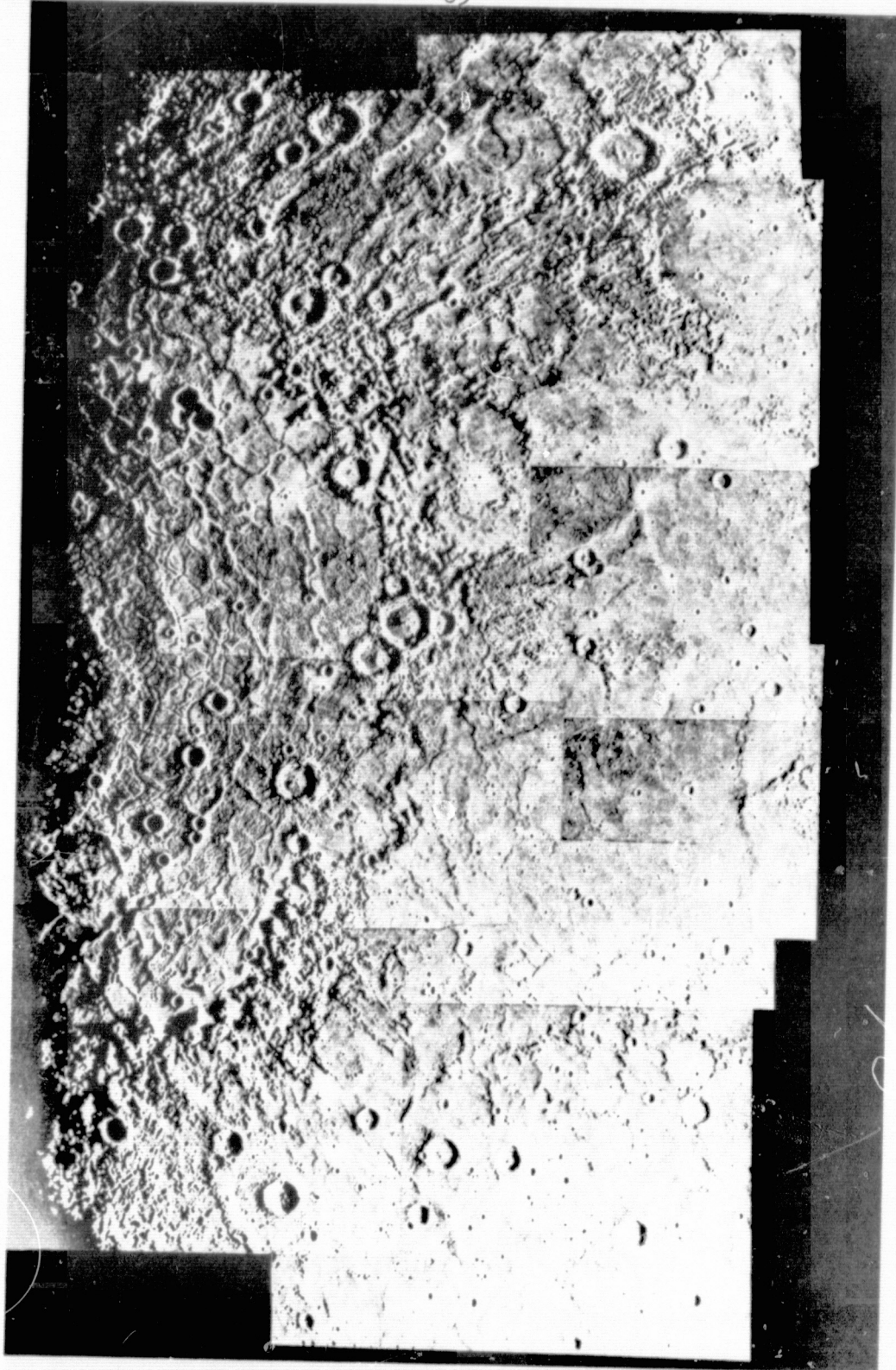


Figure 4

a

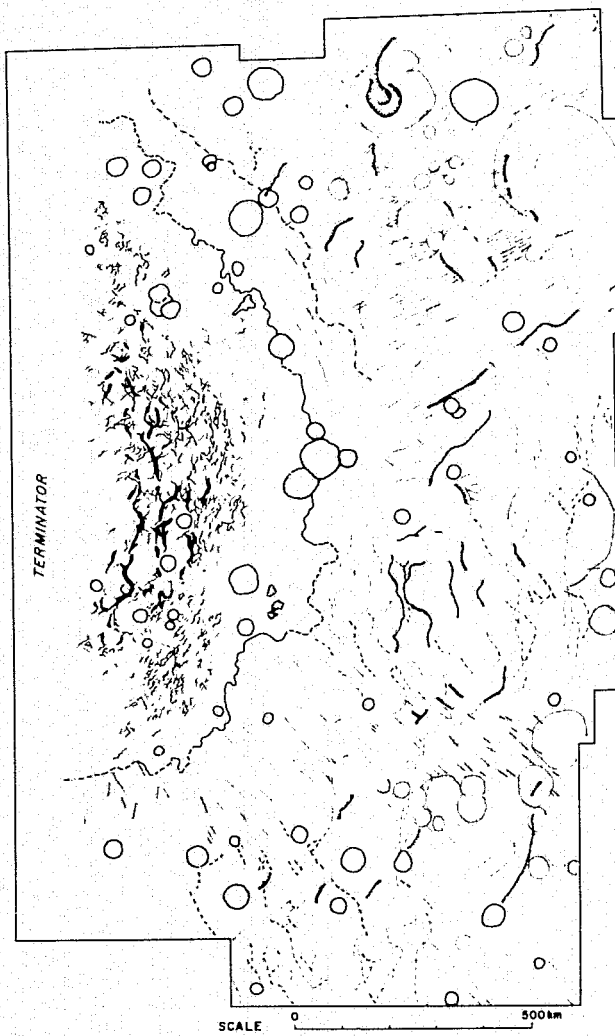
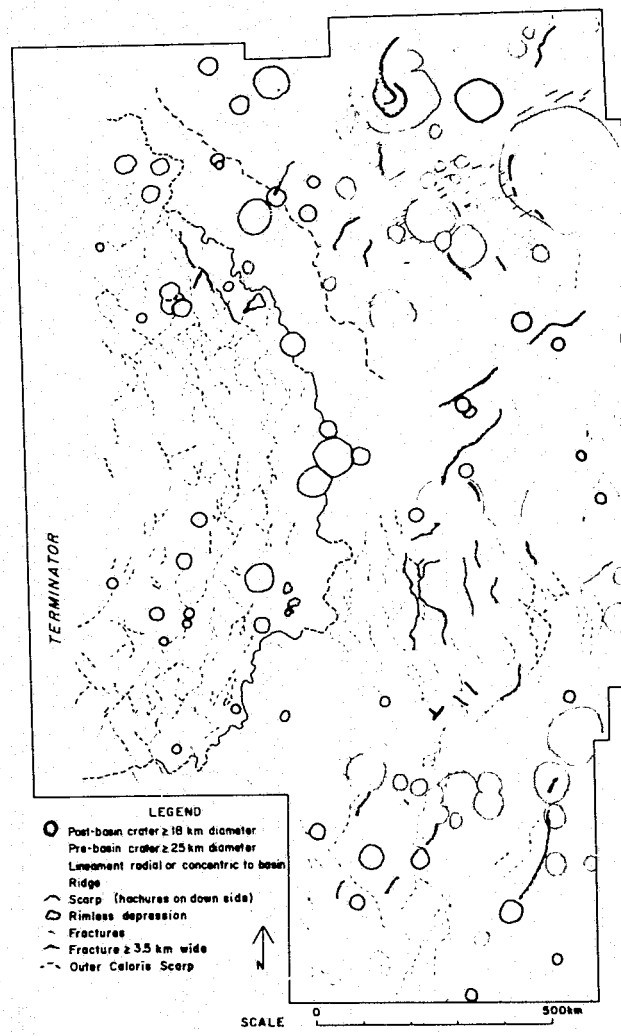


Figure 4

b



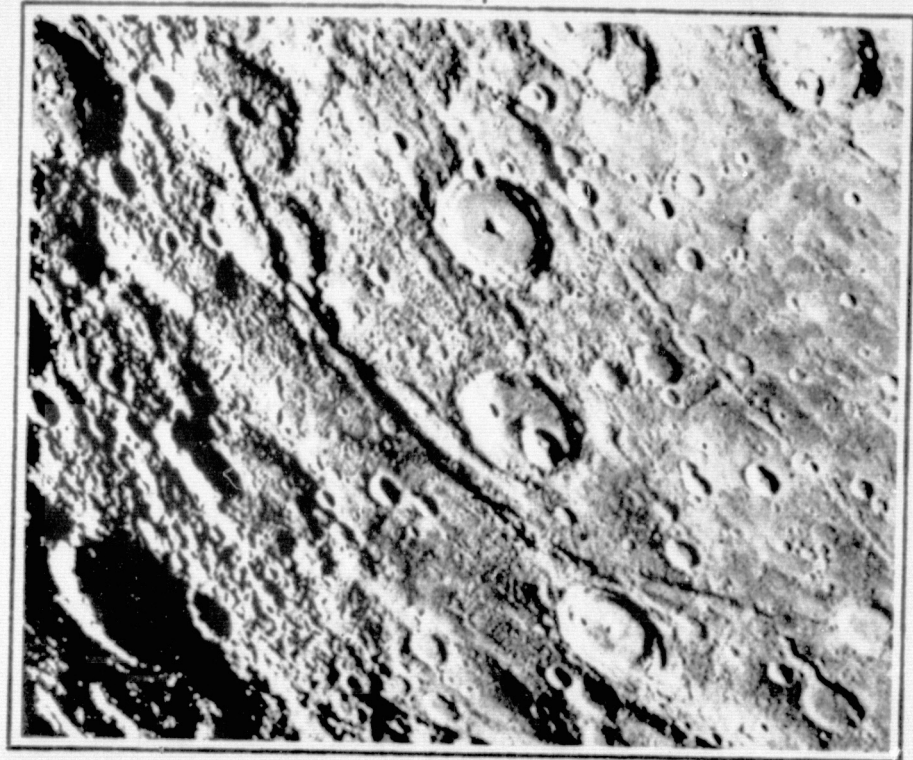
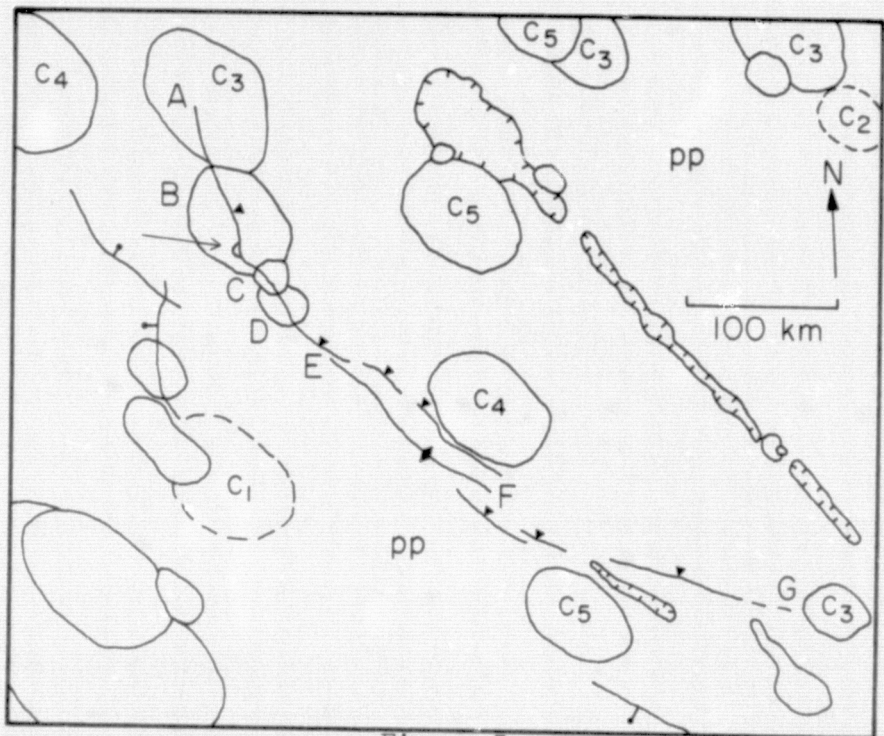
**a**

Figure 5

b

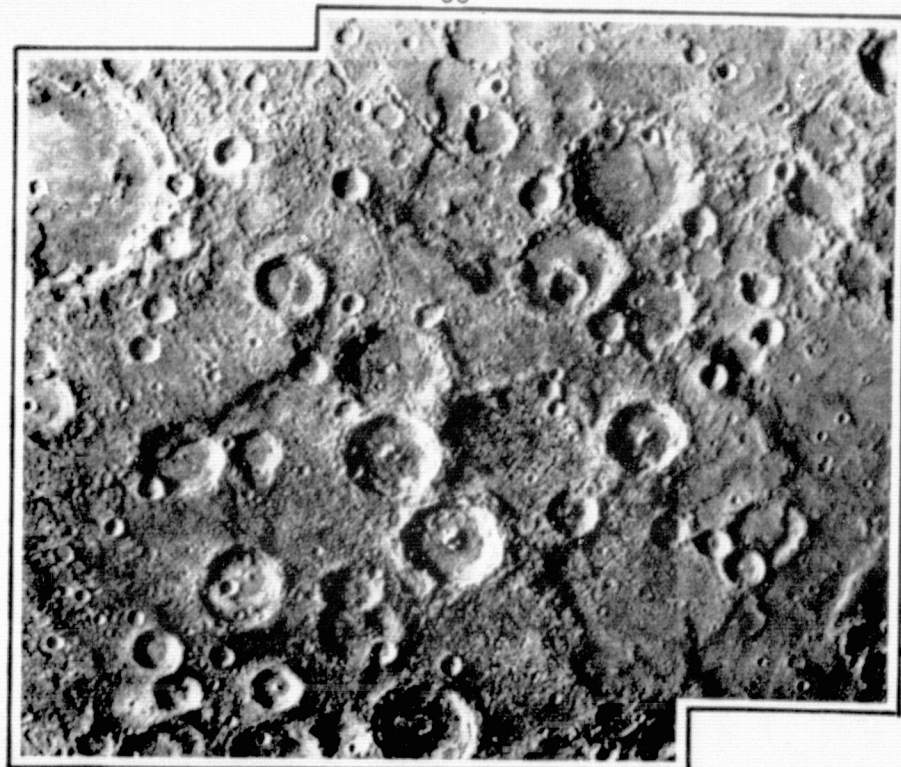
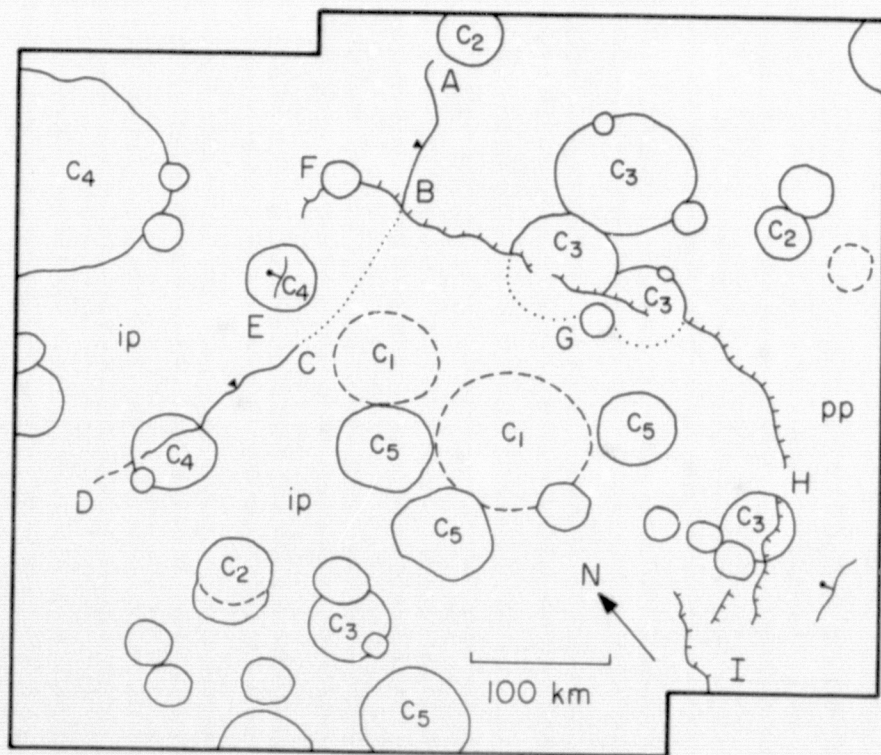
**a**

Figure 6

b

REPRODUCIBILITY OF THE
ORIGINAL PAGE IS POOR

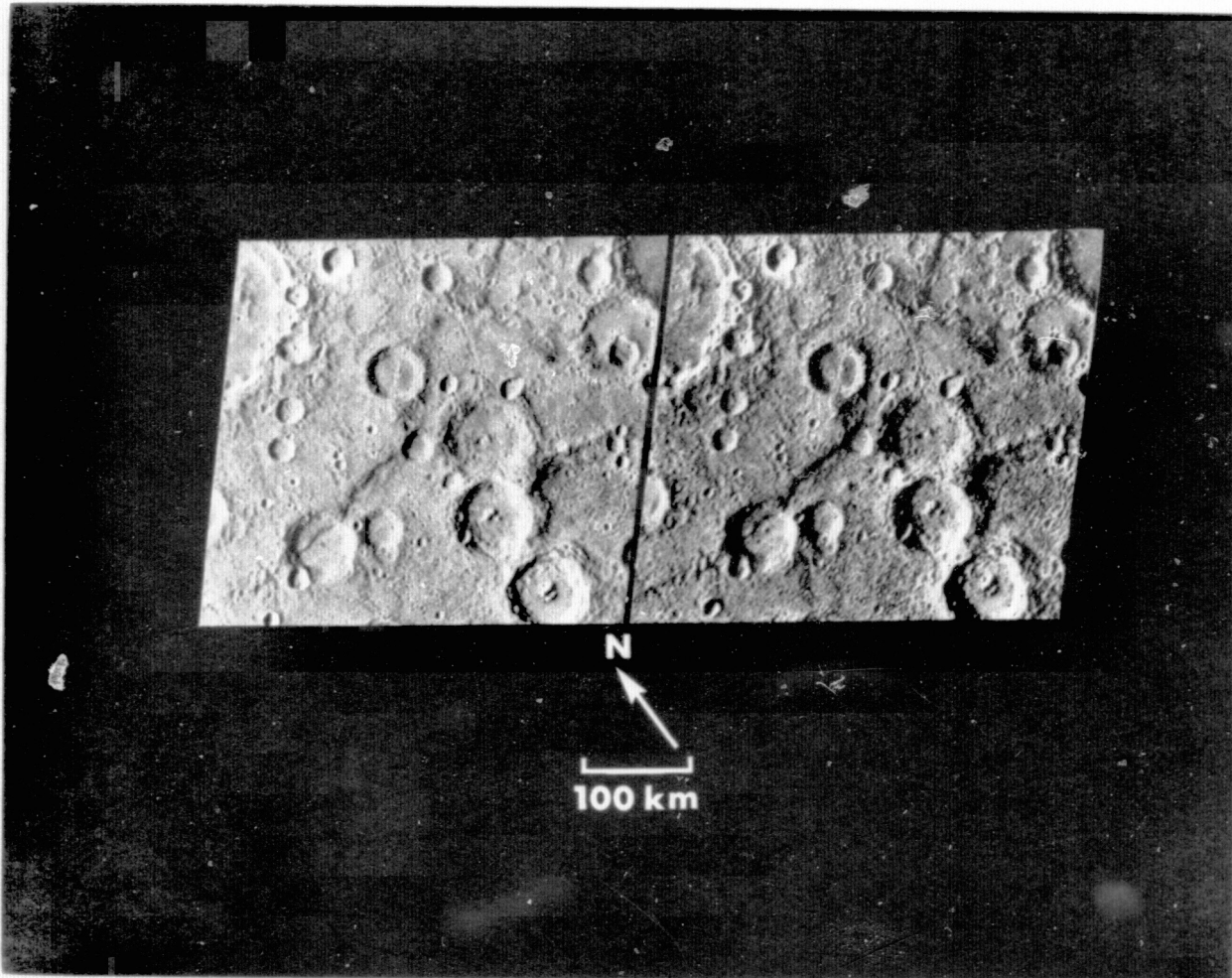


Figure 7

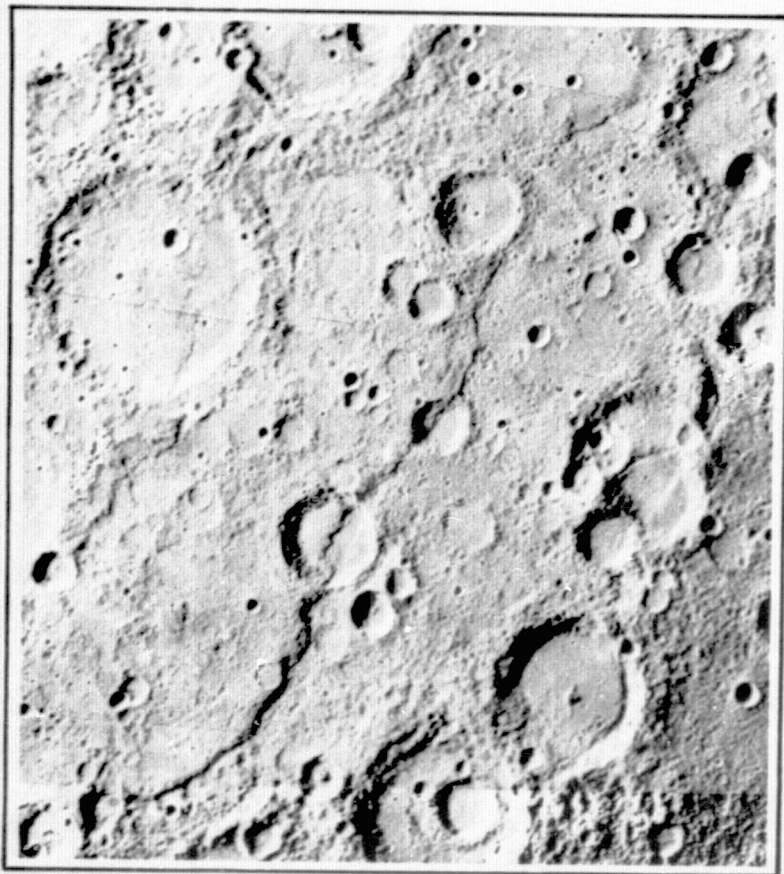
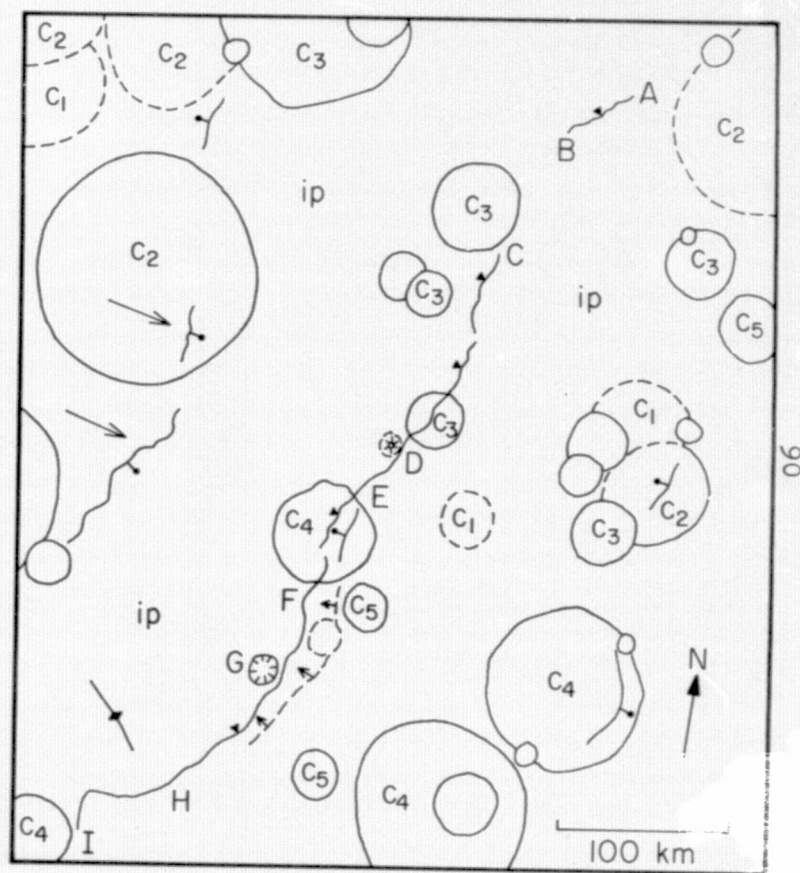
**a****b**

Figure 8

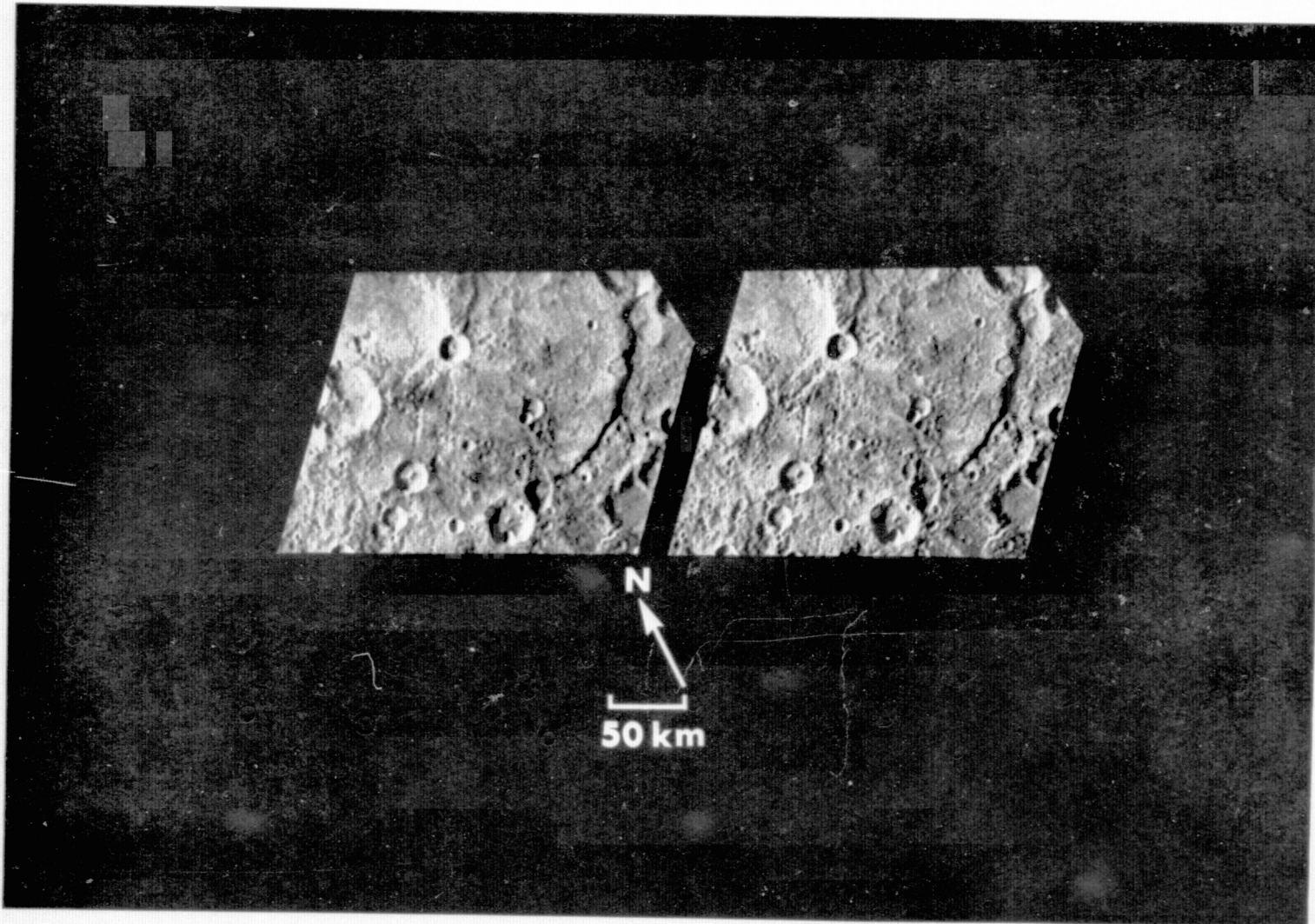
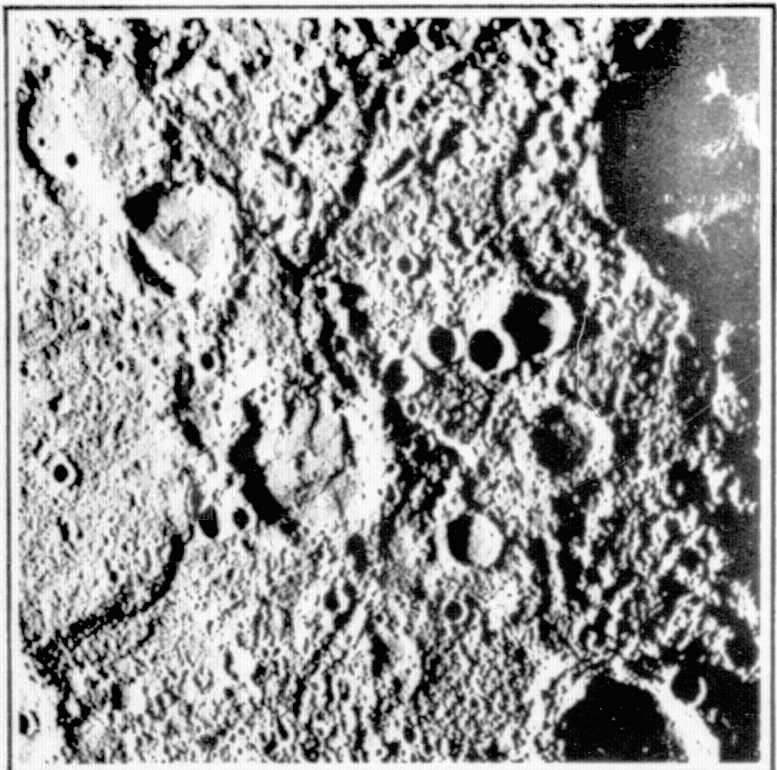


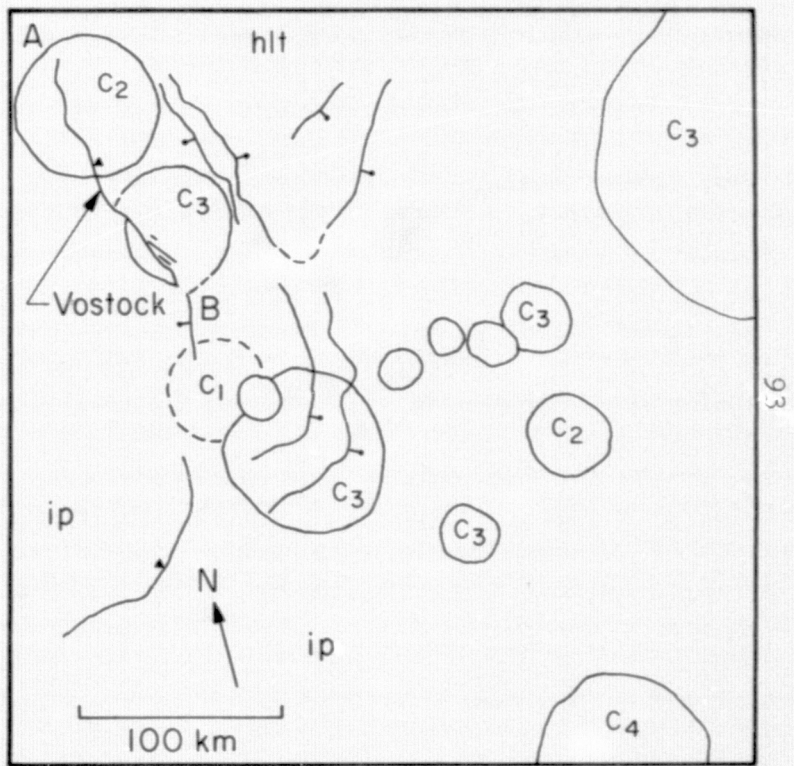
Figure 9



Figure 10



a



b

Figure 11

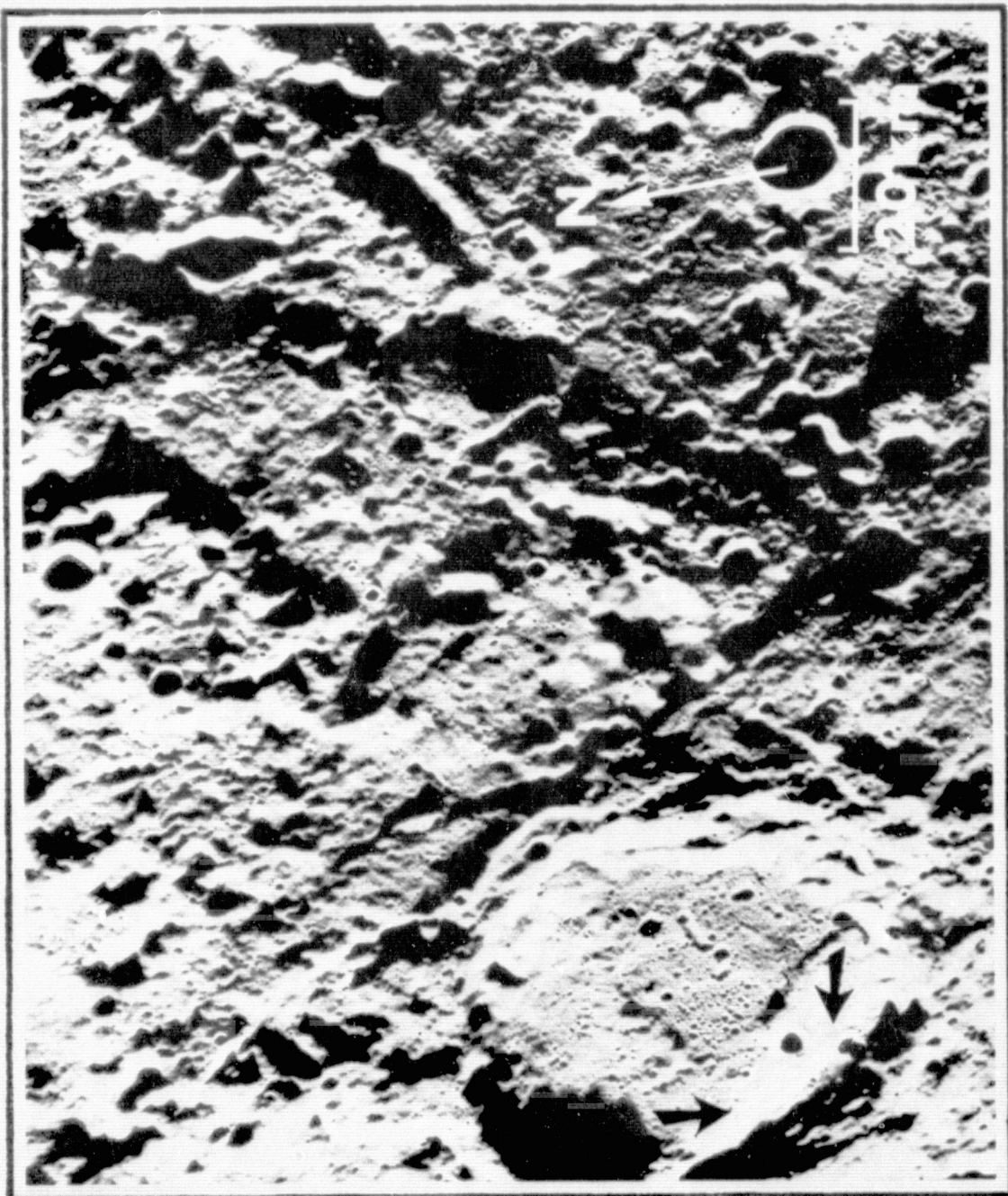


Figure 12

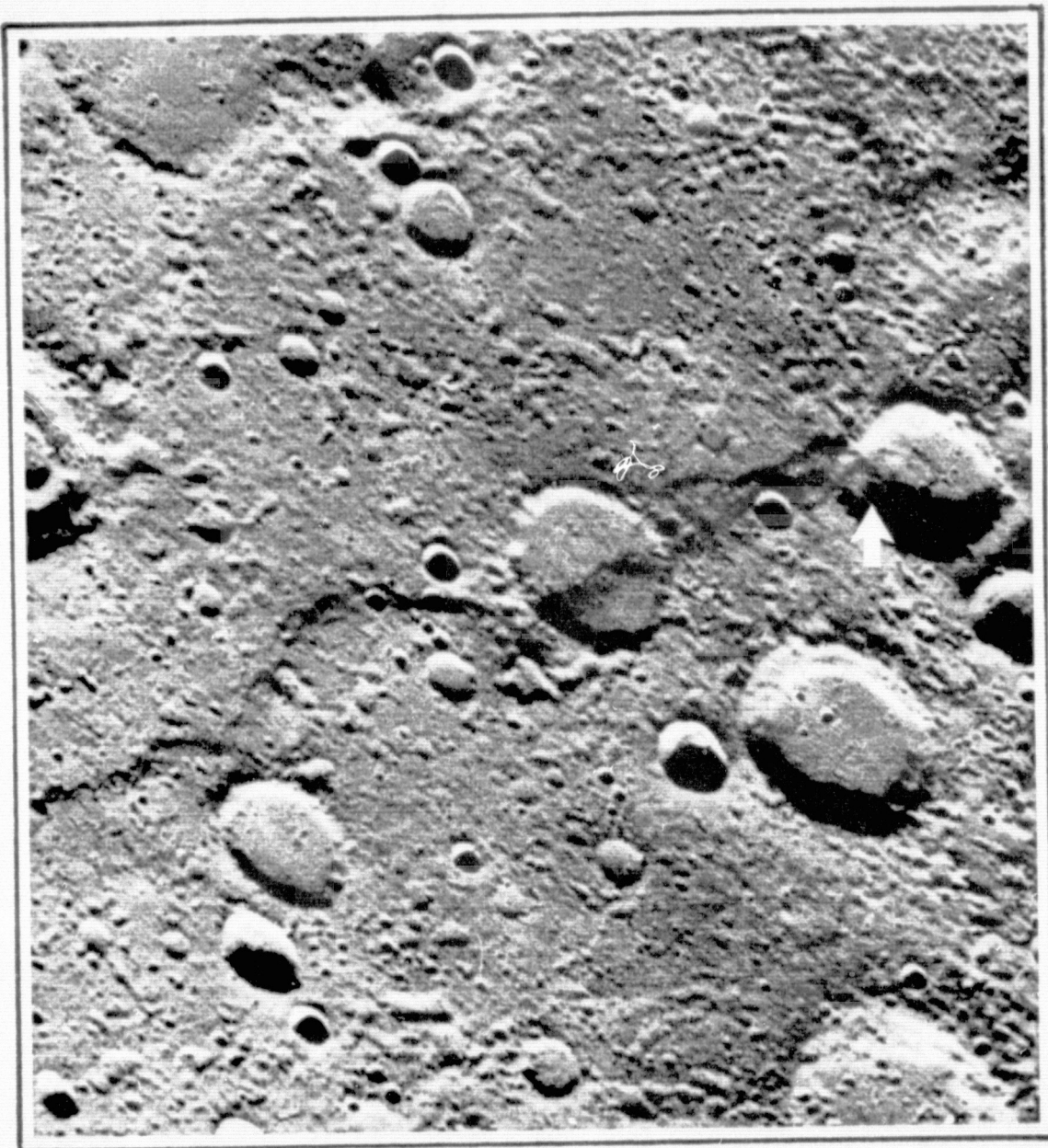


Figure 13

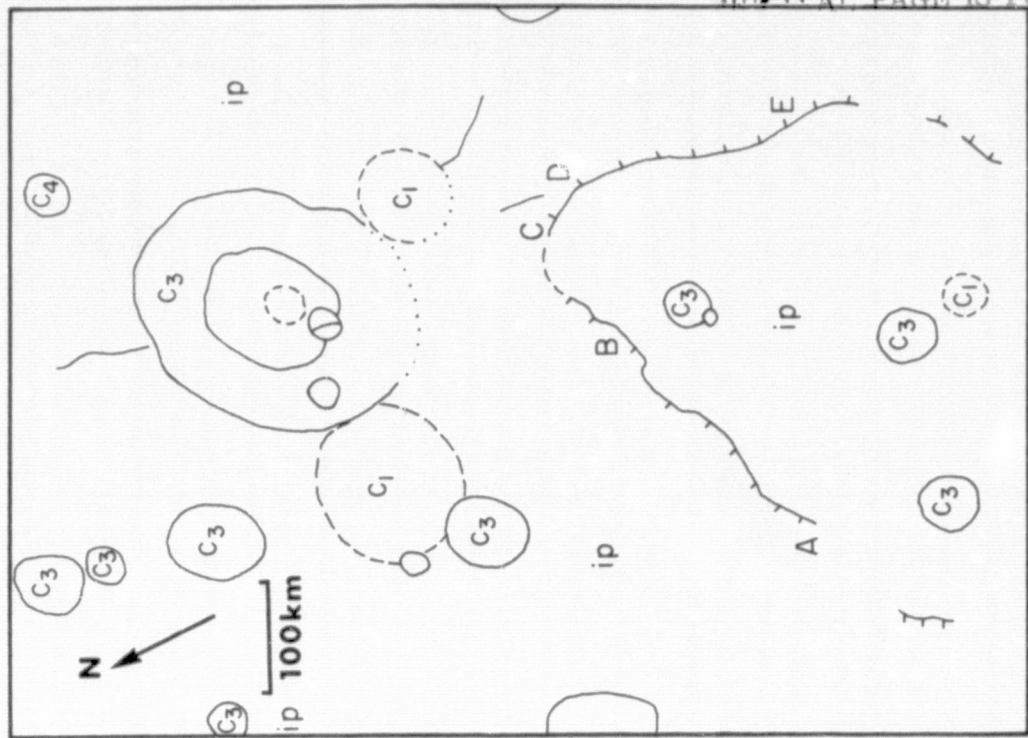
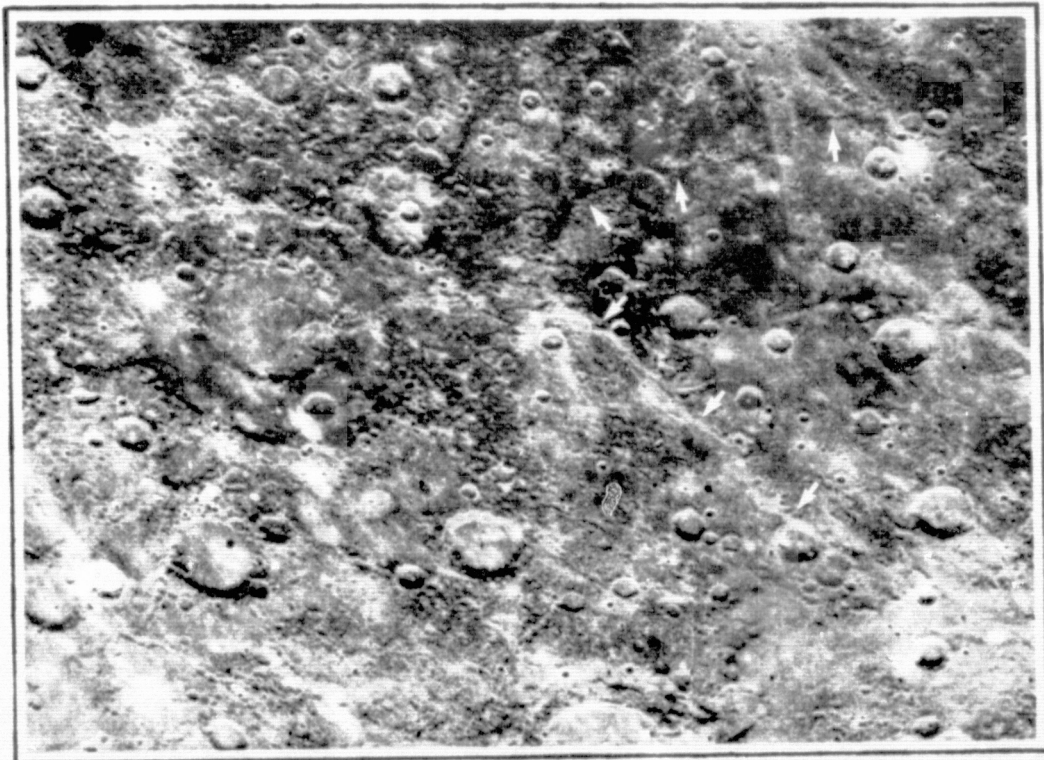
**b****c**

Figure 14

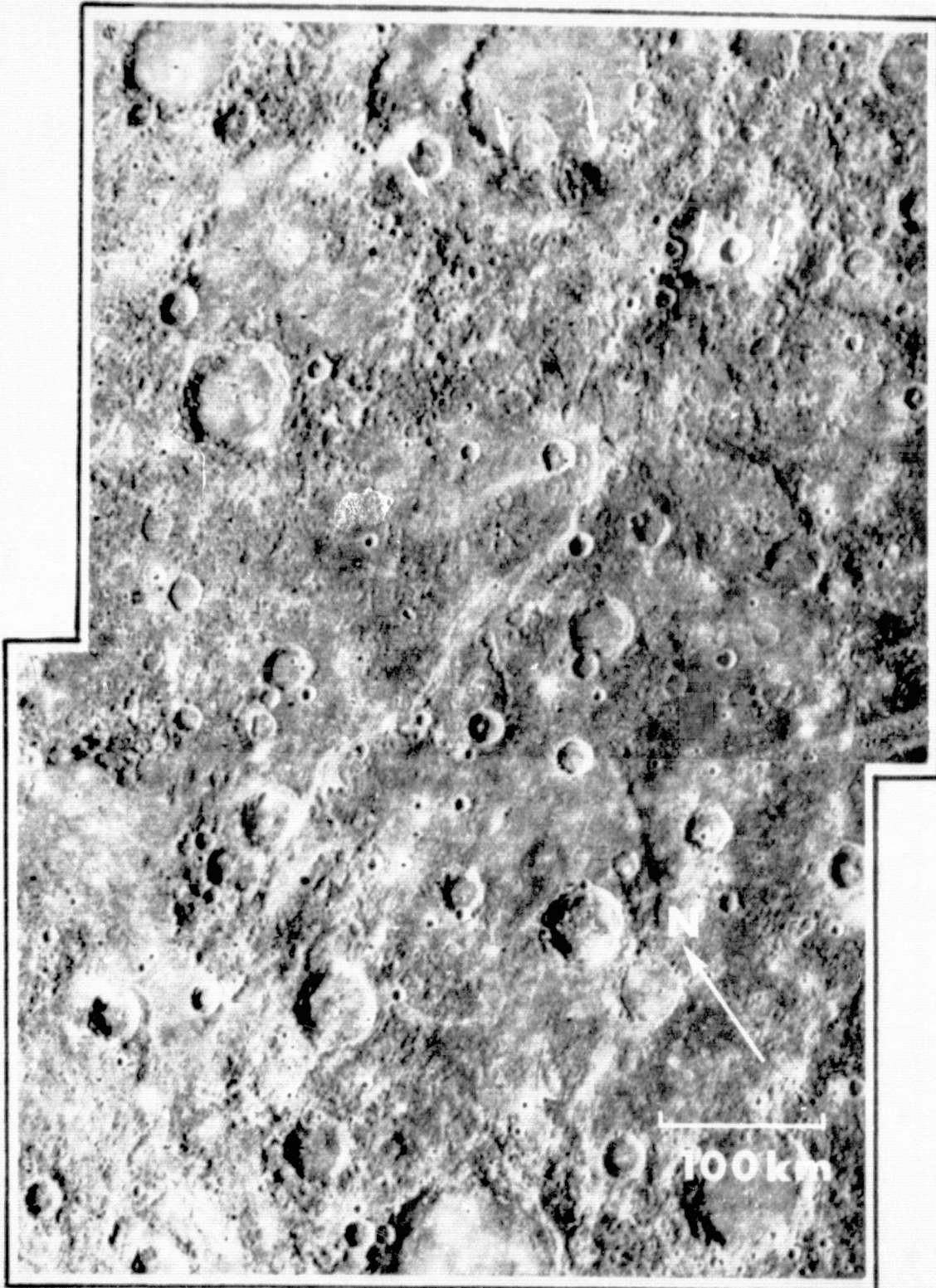


Figure 15

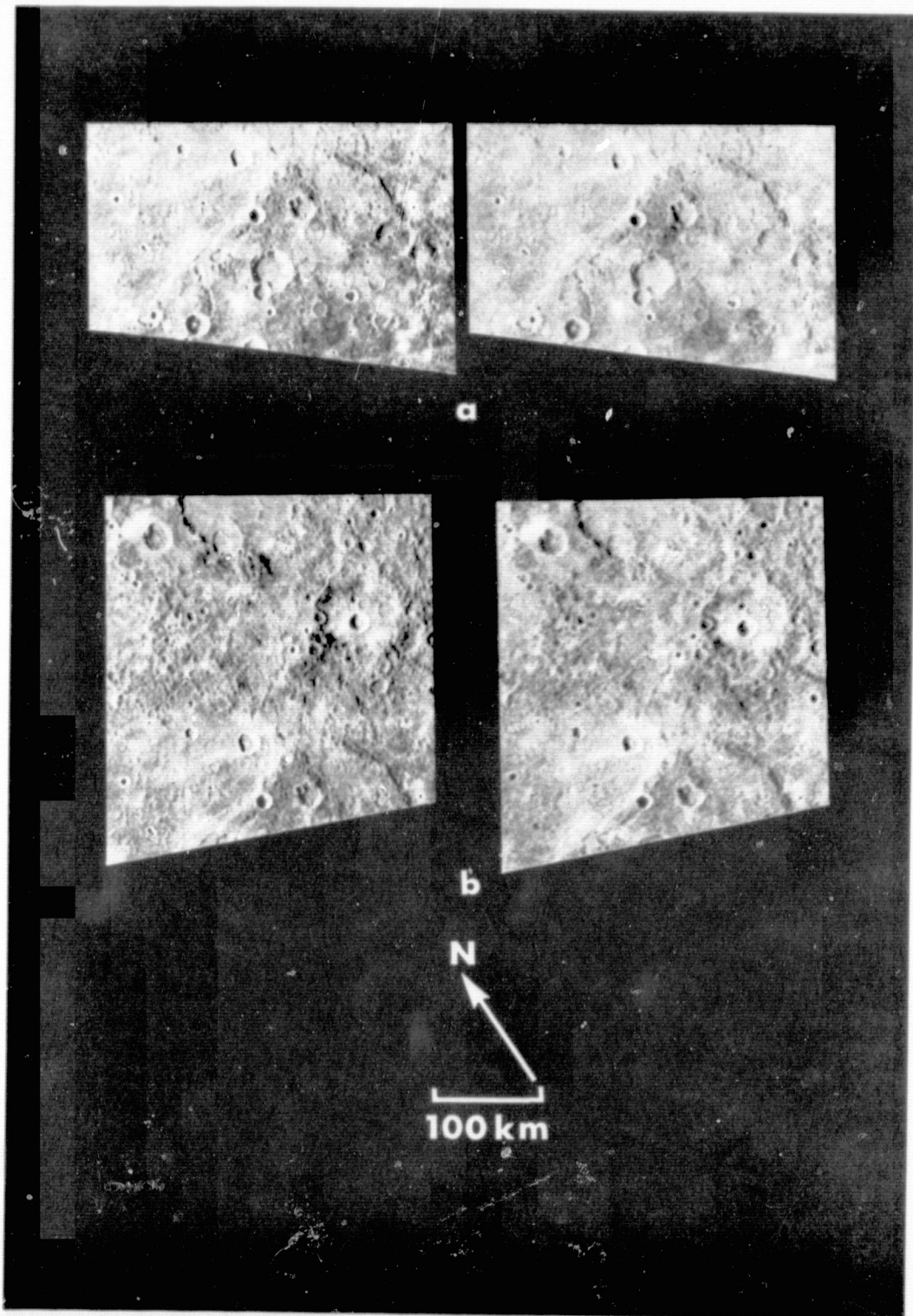
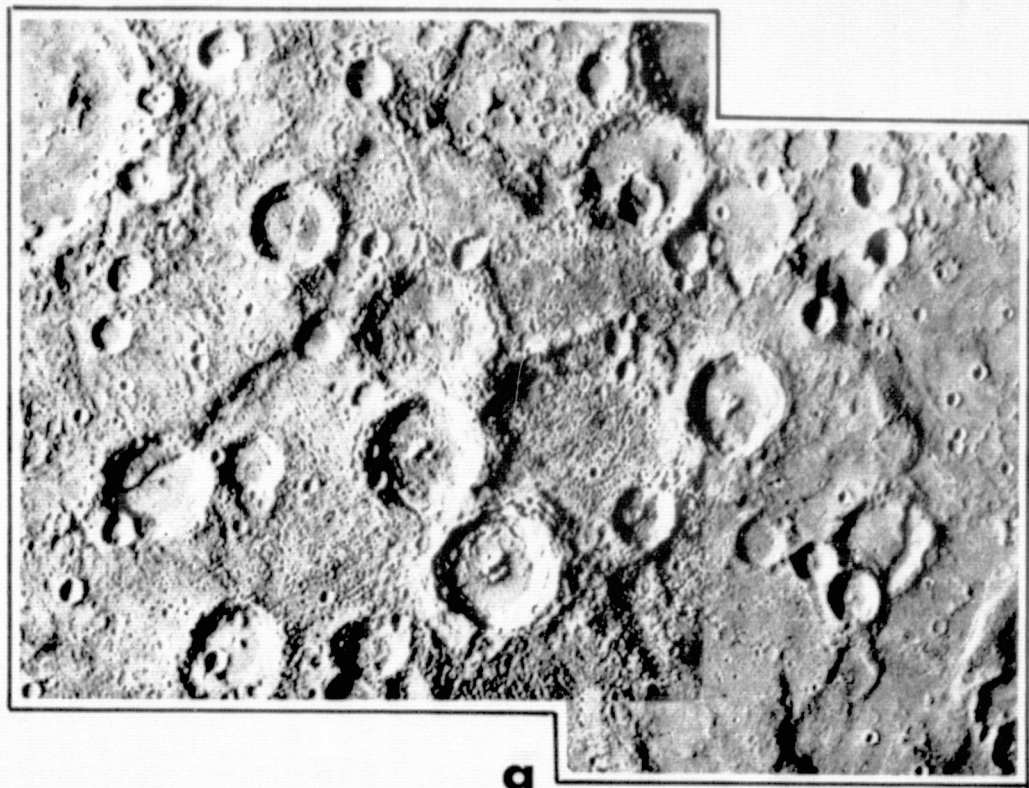
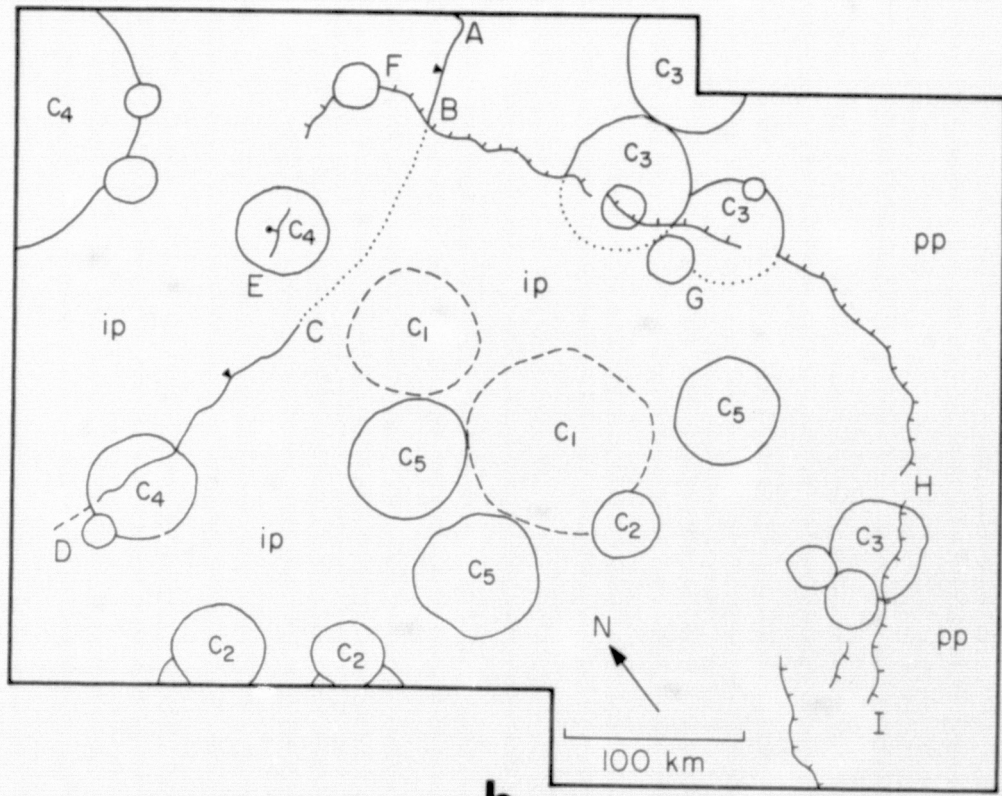


Figure 16



a



b

Figure 17

100

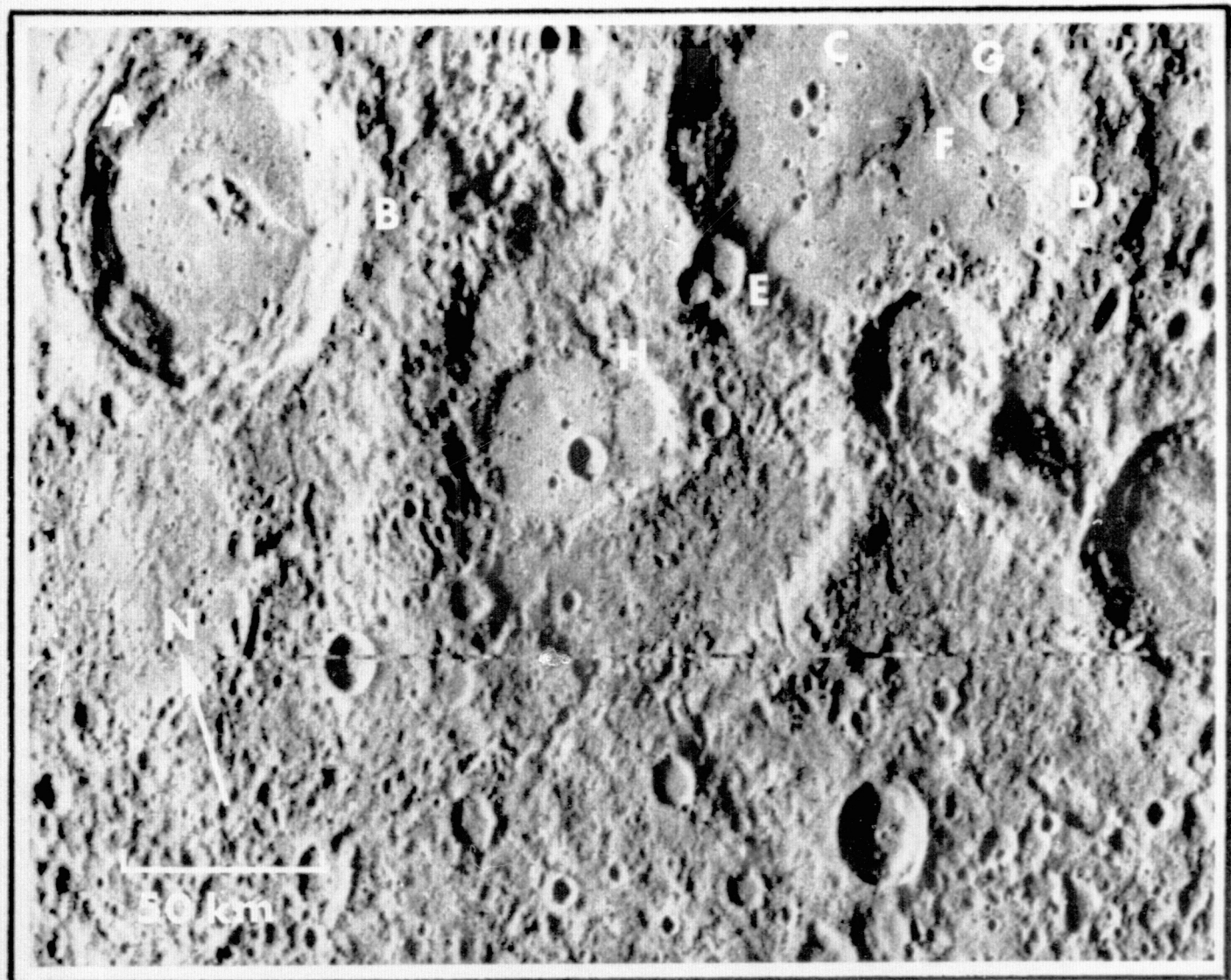


Figure 18

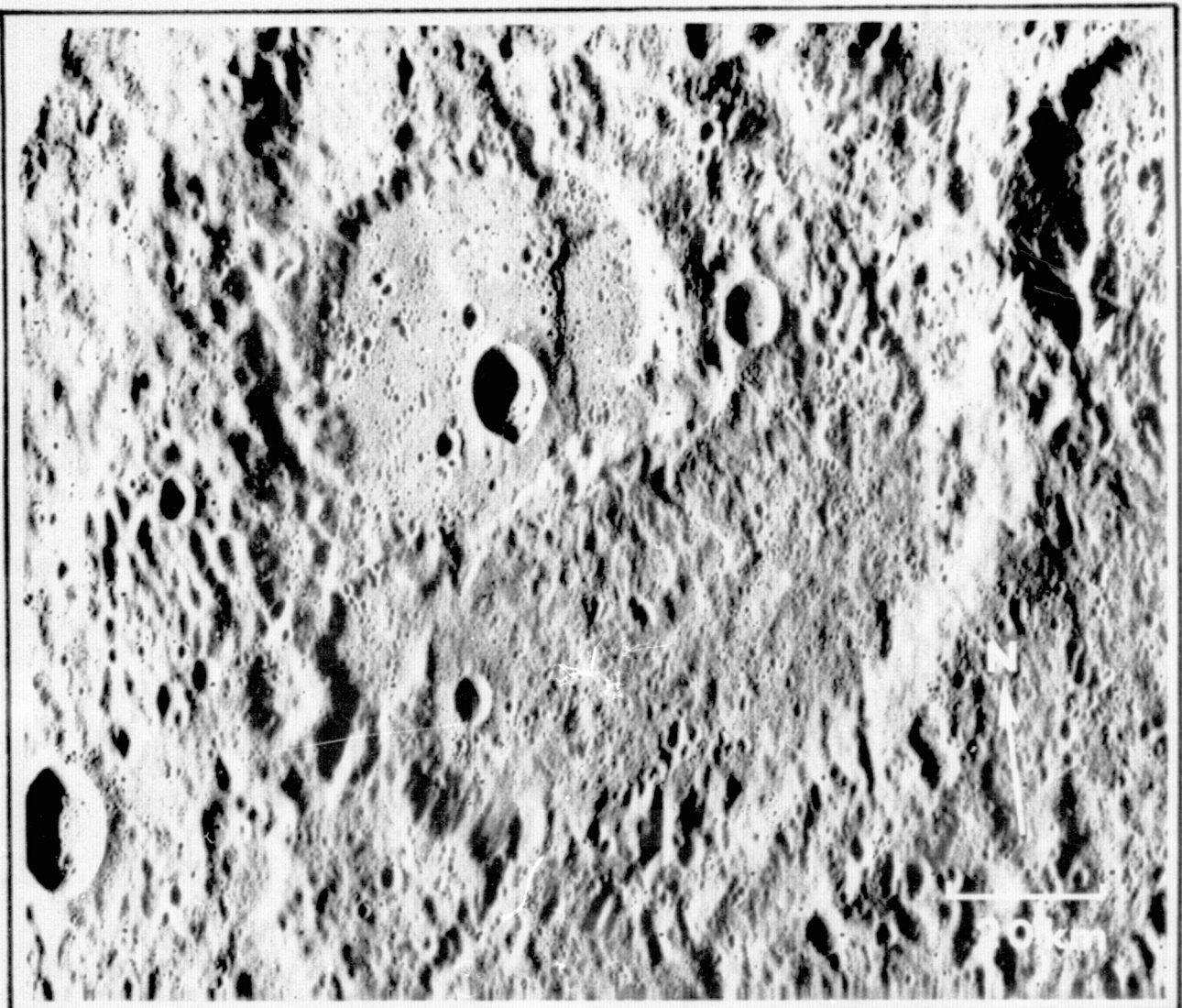


Figure 19

INTRACRATER FEATURES



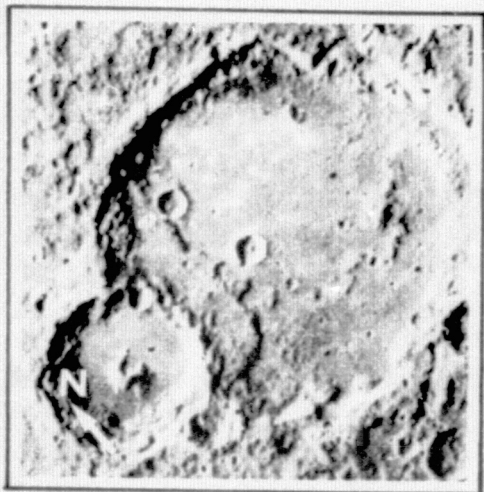
FDS-27379
Lat - 30°S
Long - 35°W
Picture Width - 260km



FDS-27392
Lat - 48°S
Long - 19°W
Picture Width - 190km

Figure 20

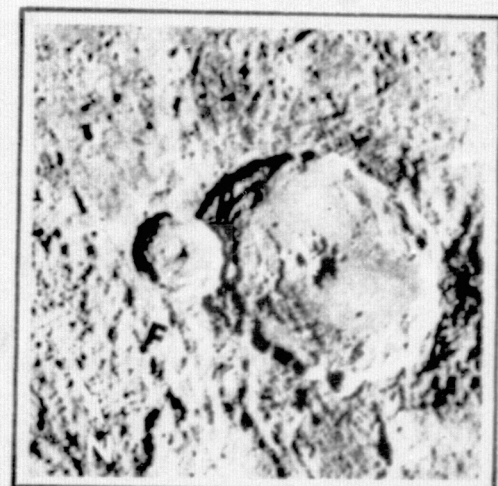
INTRACRATER FEATURES



FDS - 166673
Lat - 59°S
Long - 63°W
Picture Width - 170 km



FDS - 27420
Lat - 40°S
Long - 45°W
Picture Width - 160 km



FDS - 151
Lat - 49°N
Long - 140°W
Picture Width - 180 km

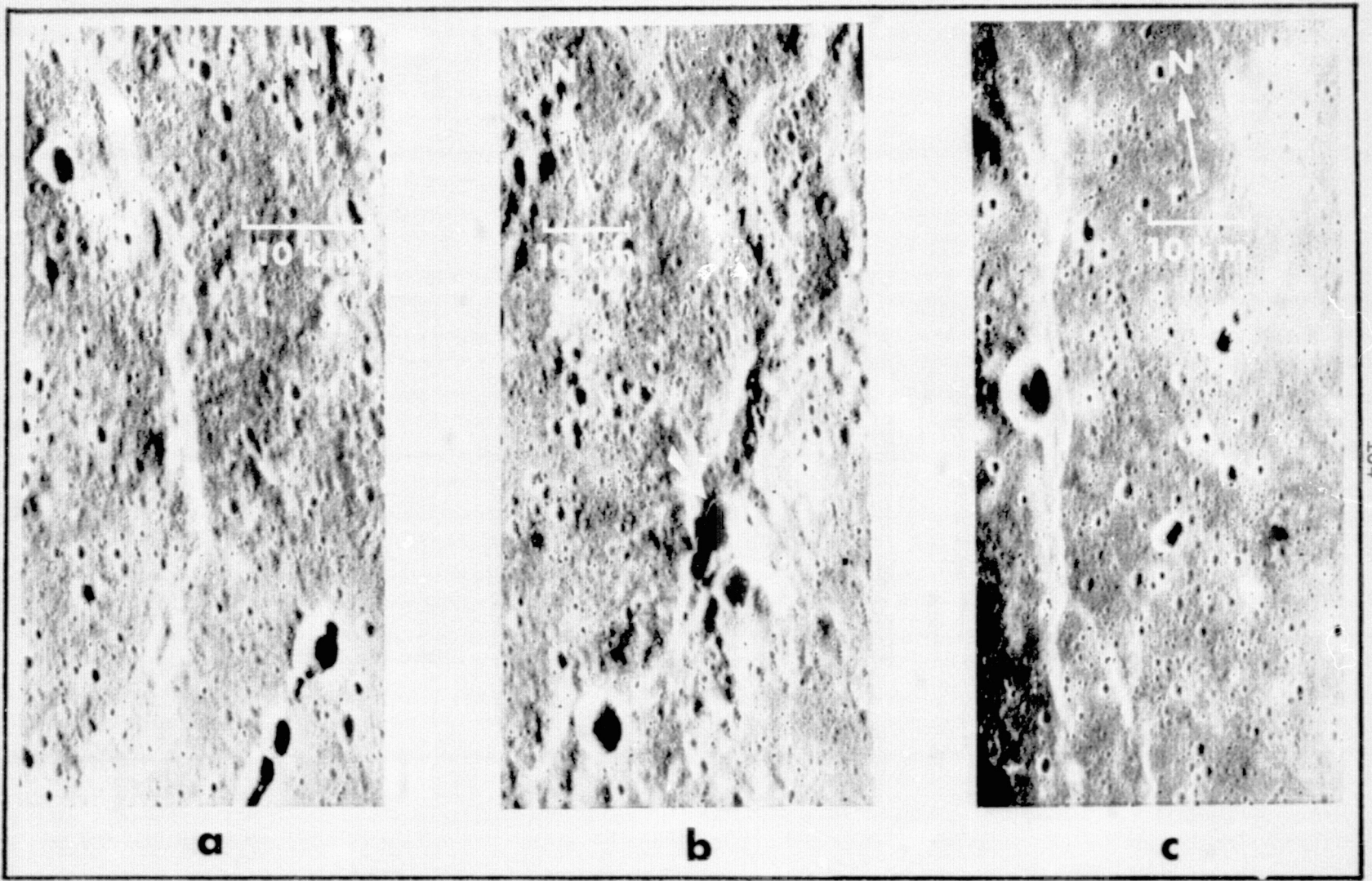


Figure 22

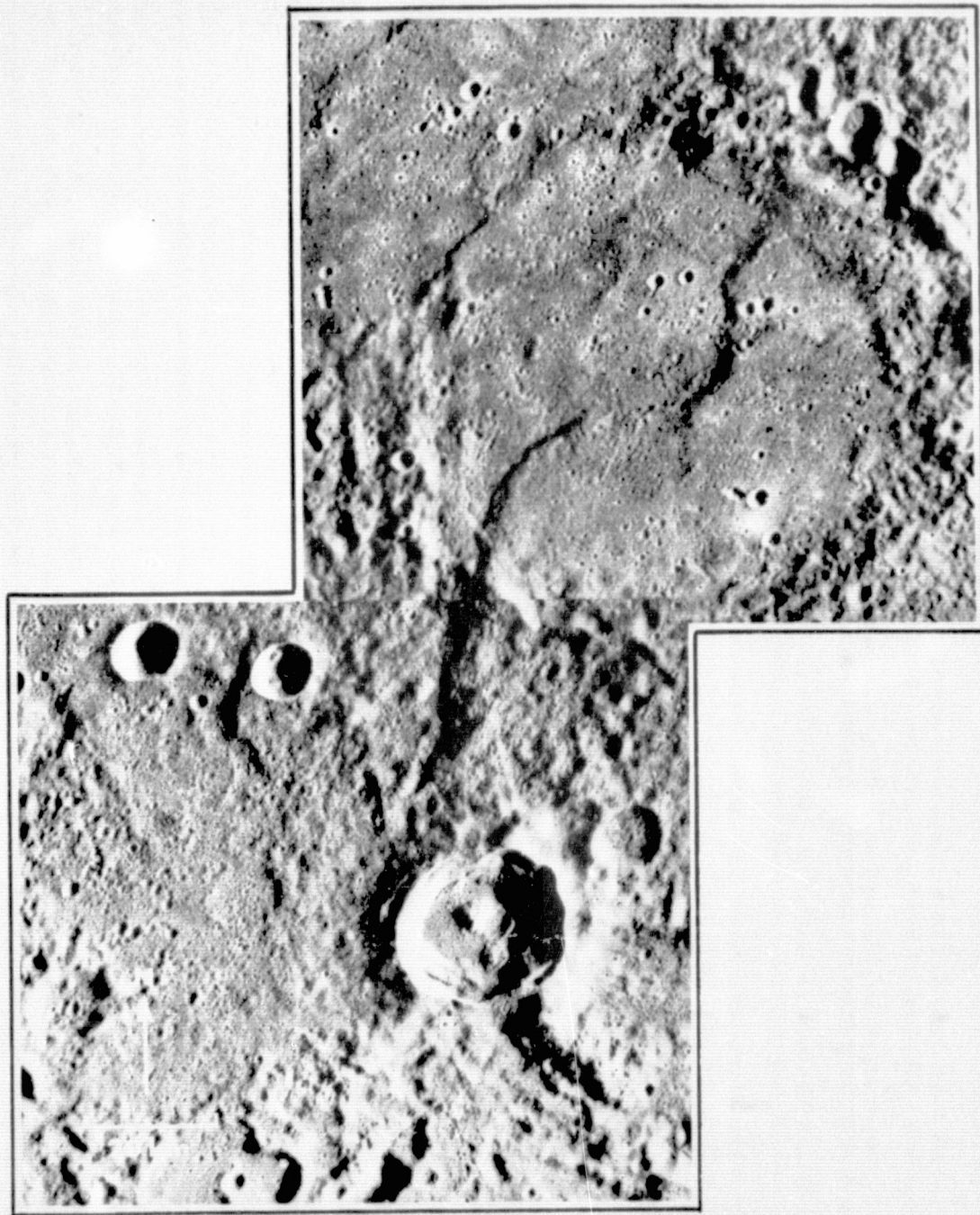


Figure 23

a

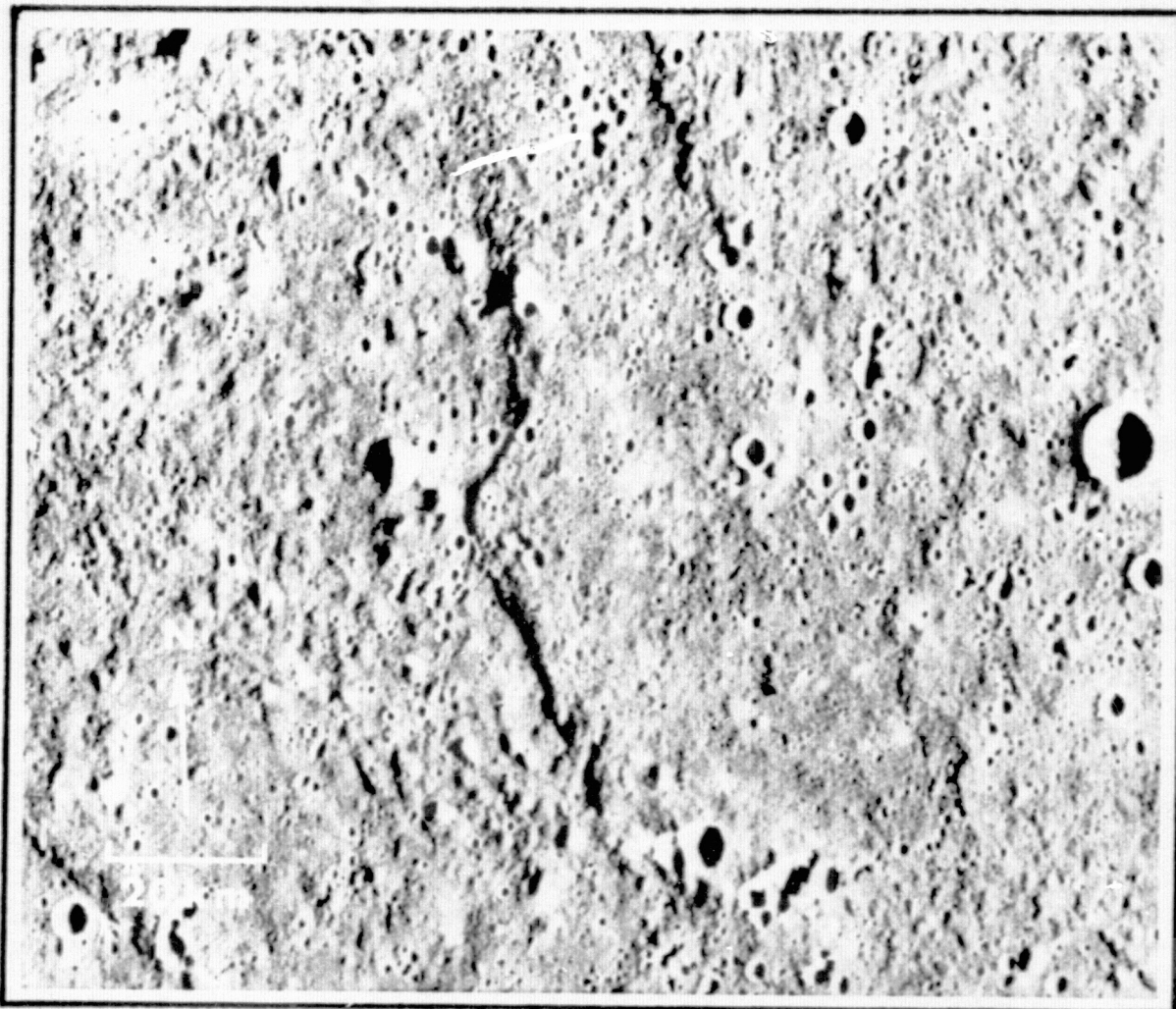
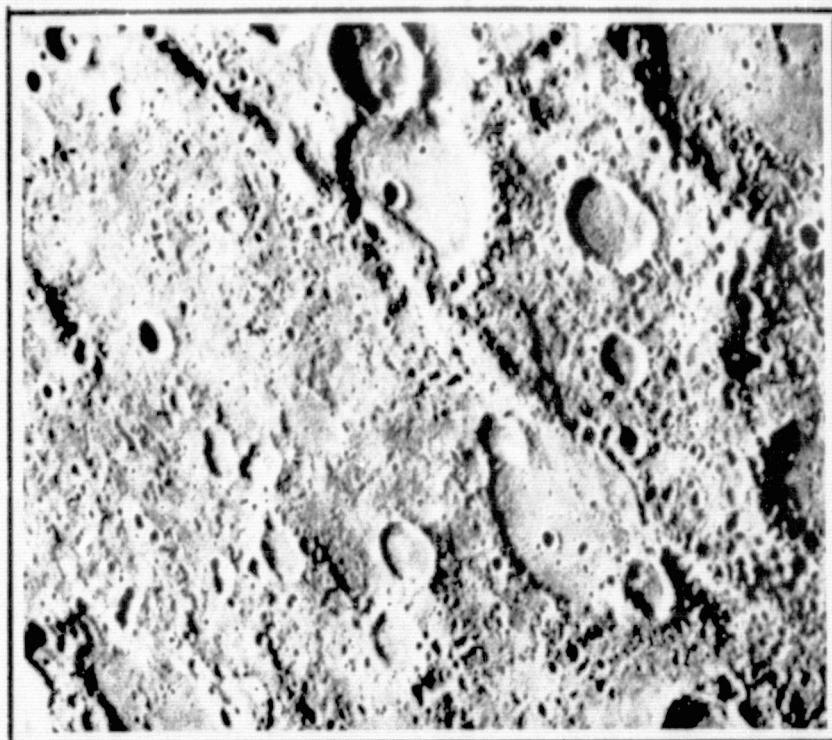


Figure 23

b



a

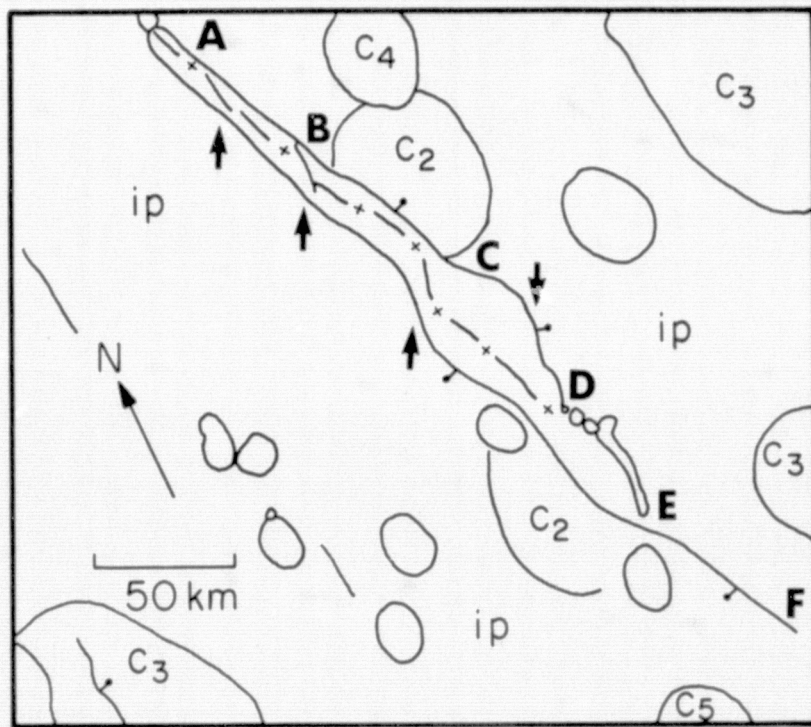
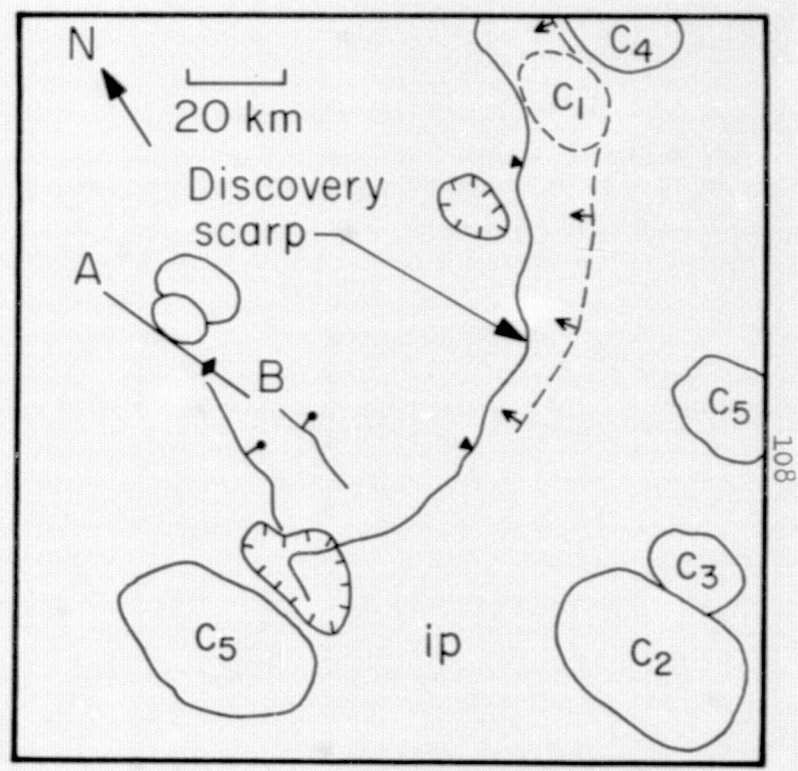


Figure 24

b



a



b

Figure 25

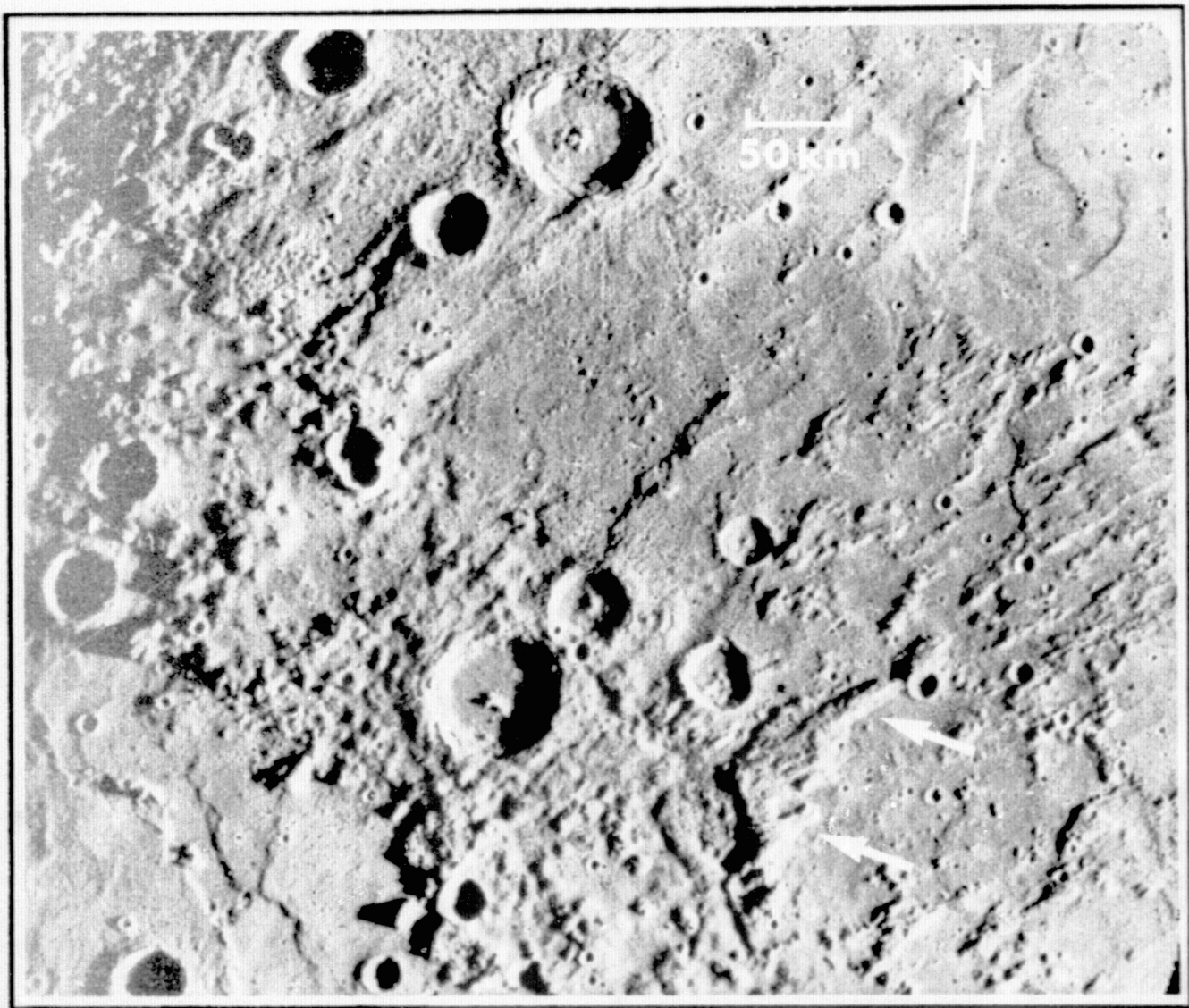
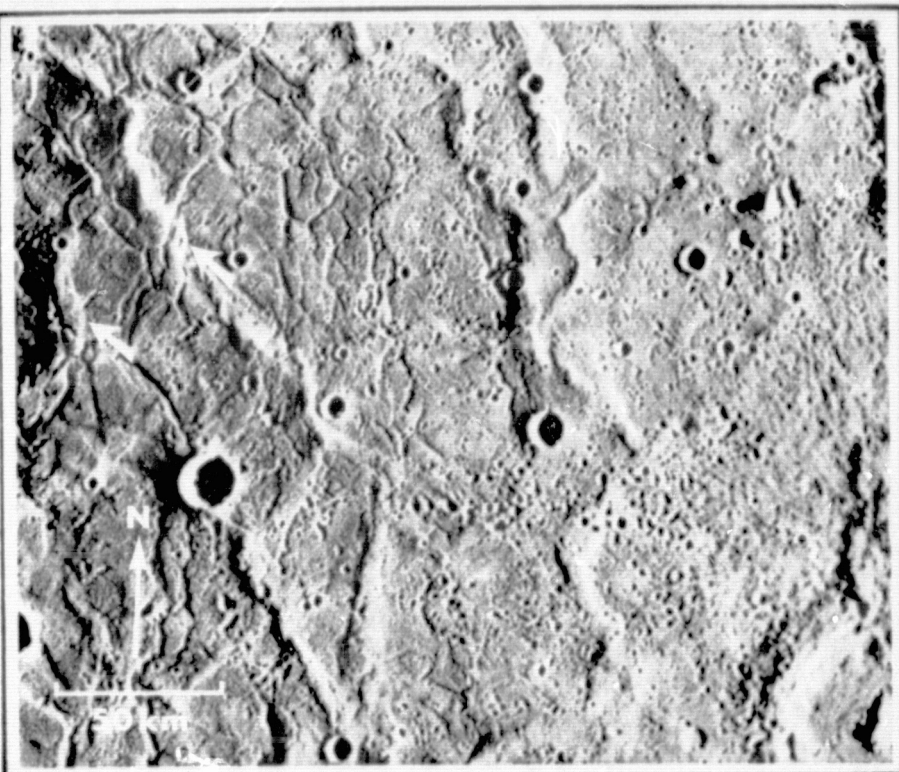
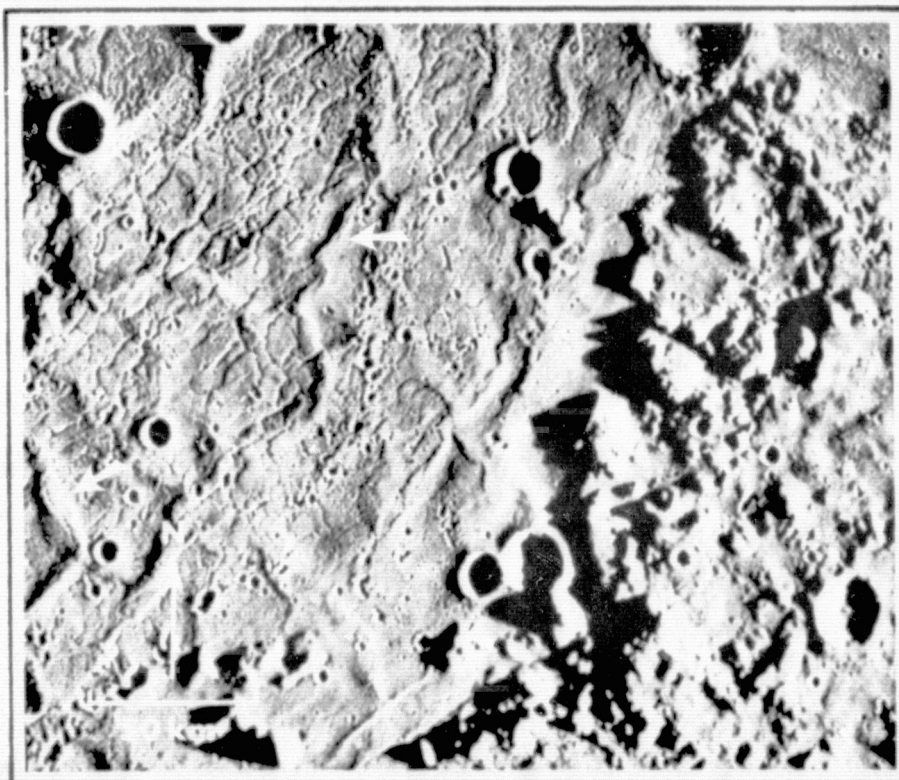


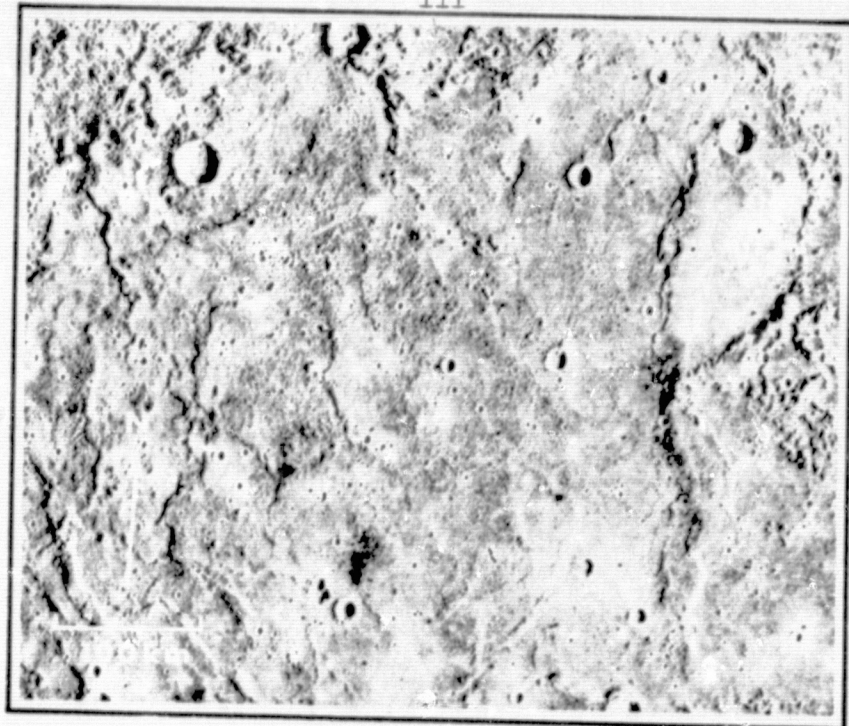
Figure 26



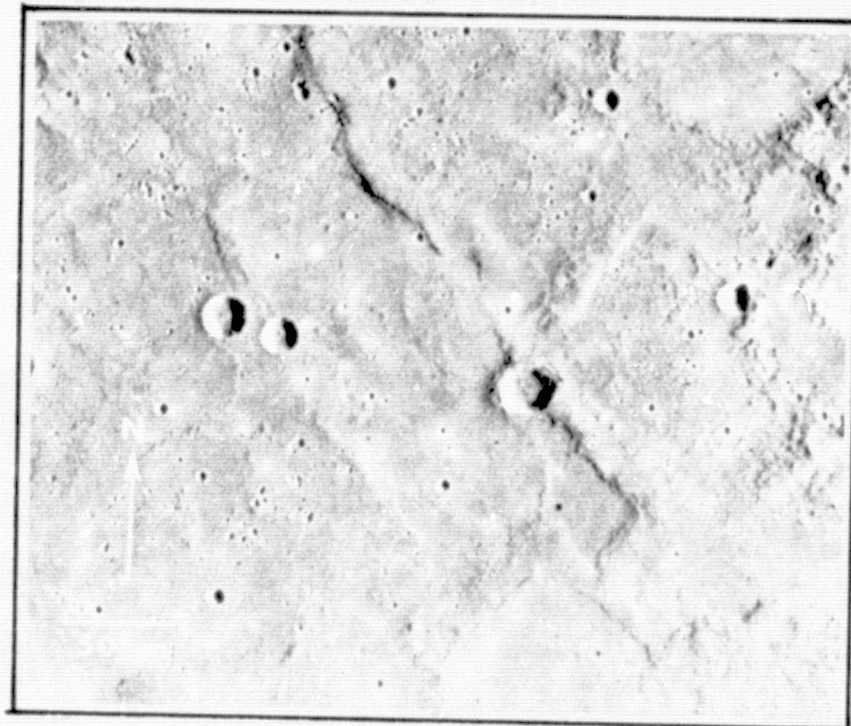
a

b
Figure 27

111



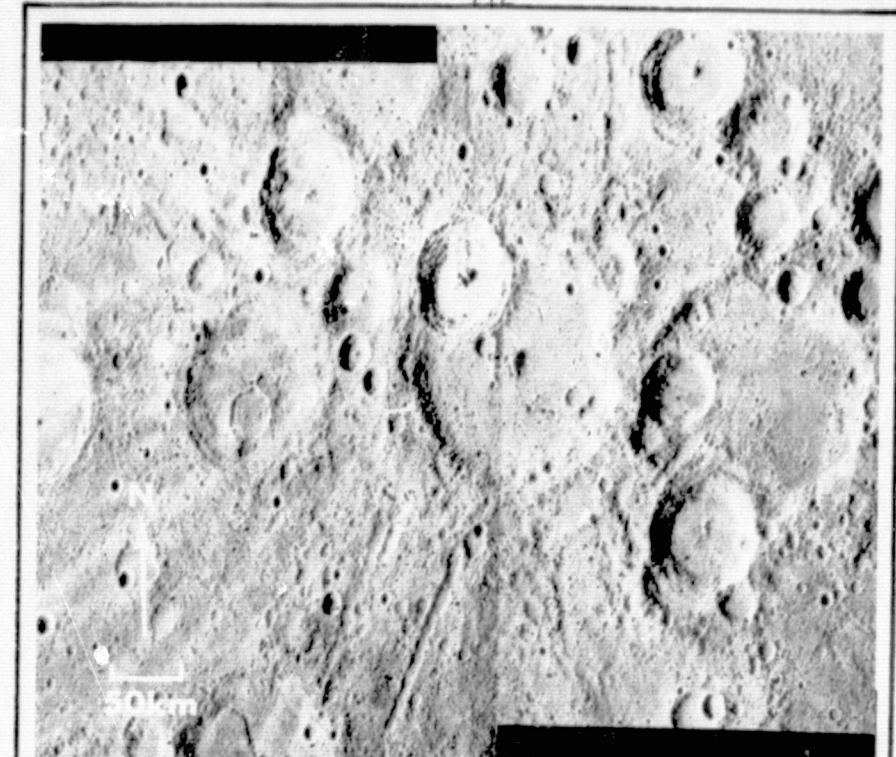
a



b

Figure 28

112



a

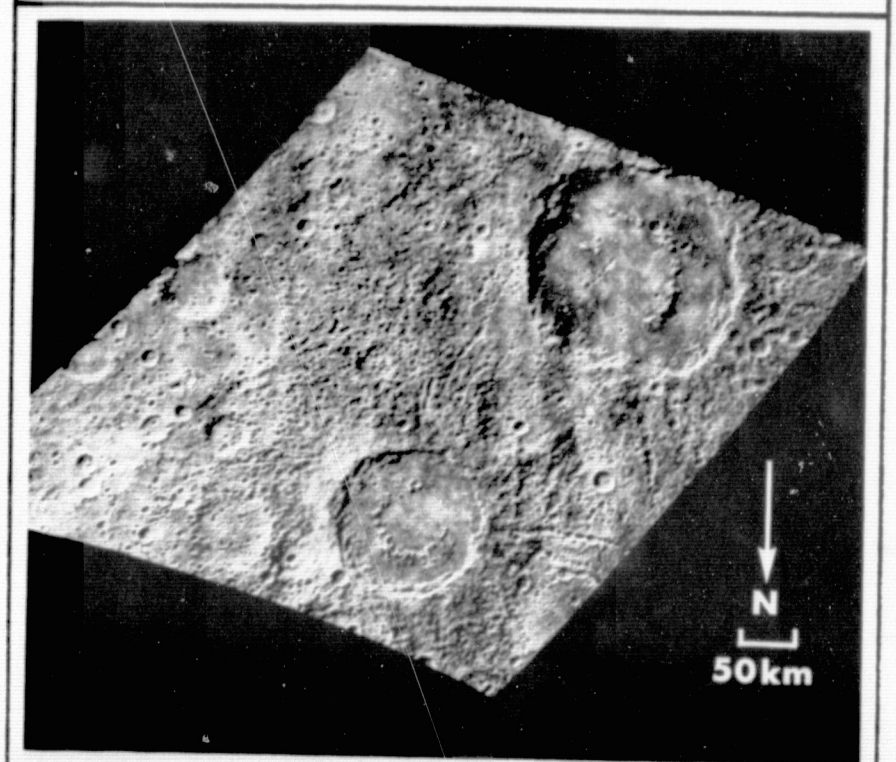


Figure 29

b

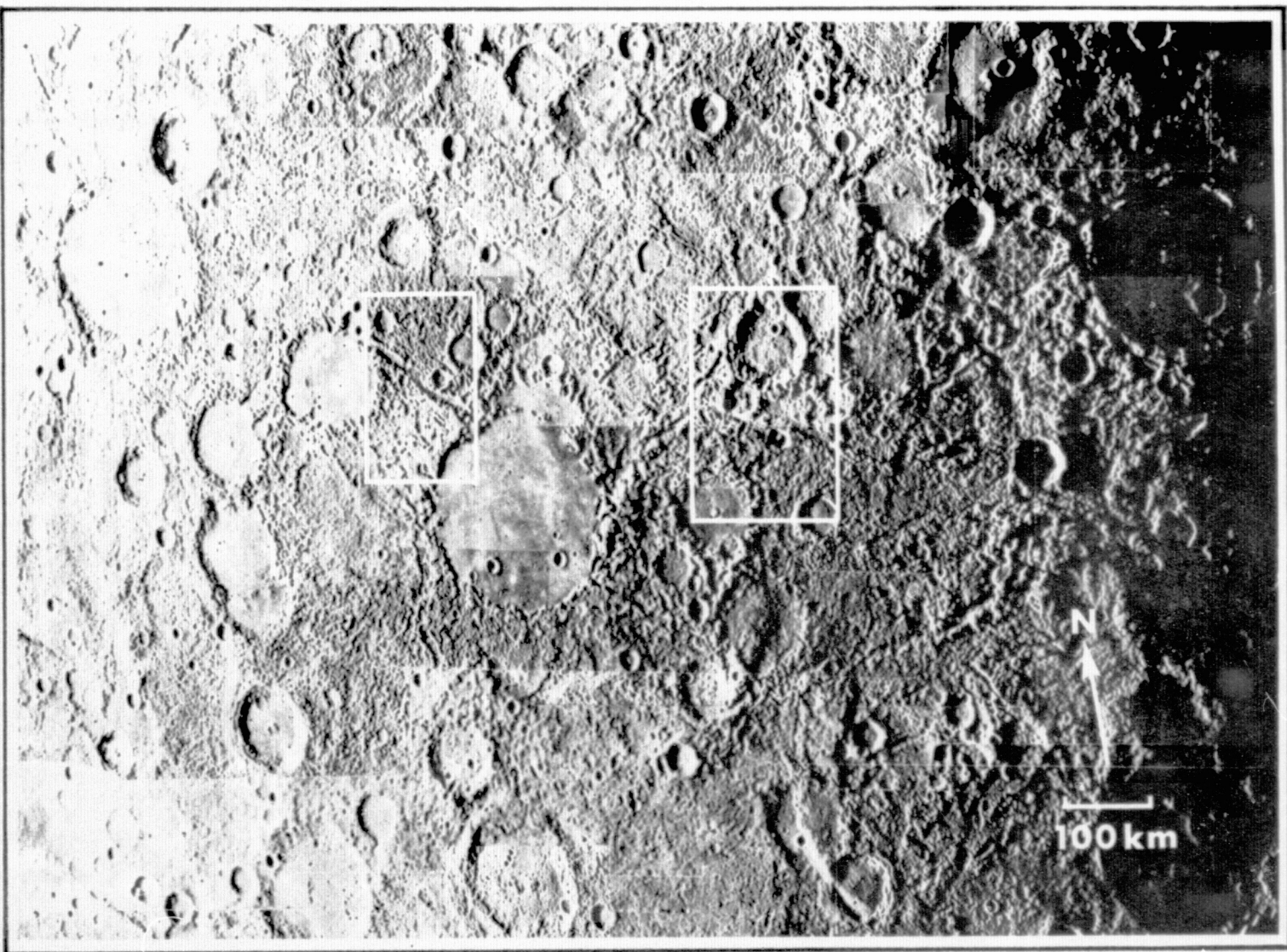


Figure 30

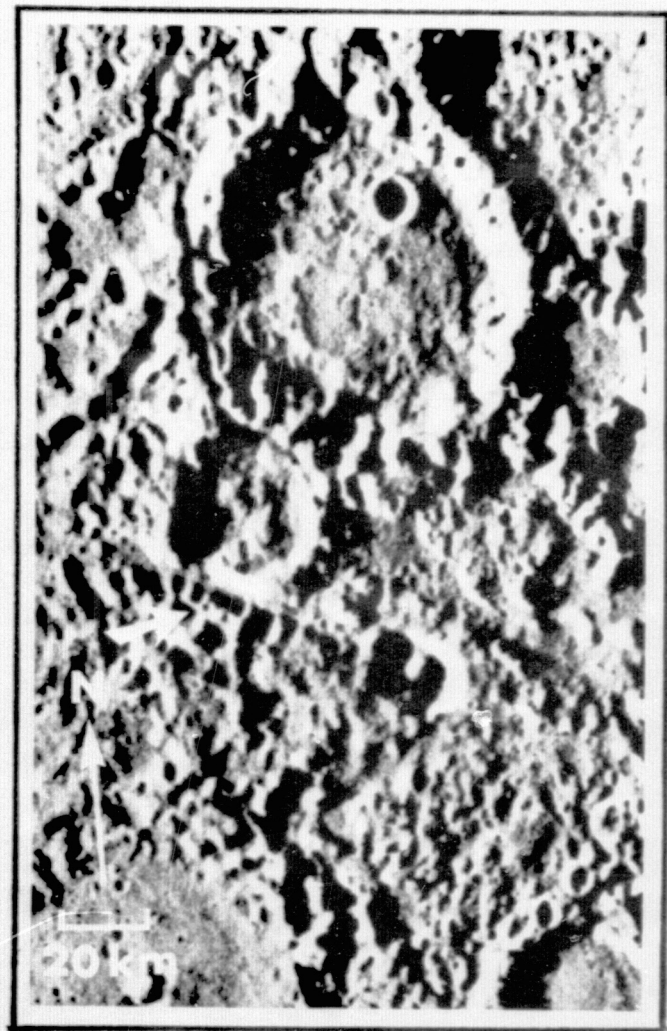
**a****b**

Figure 31

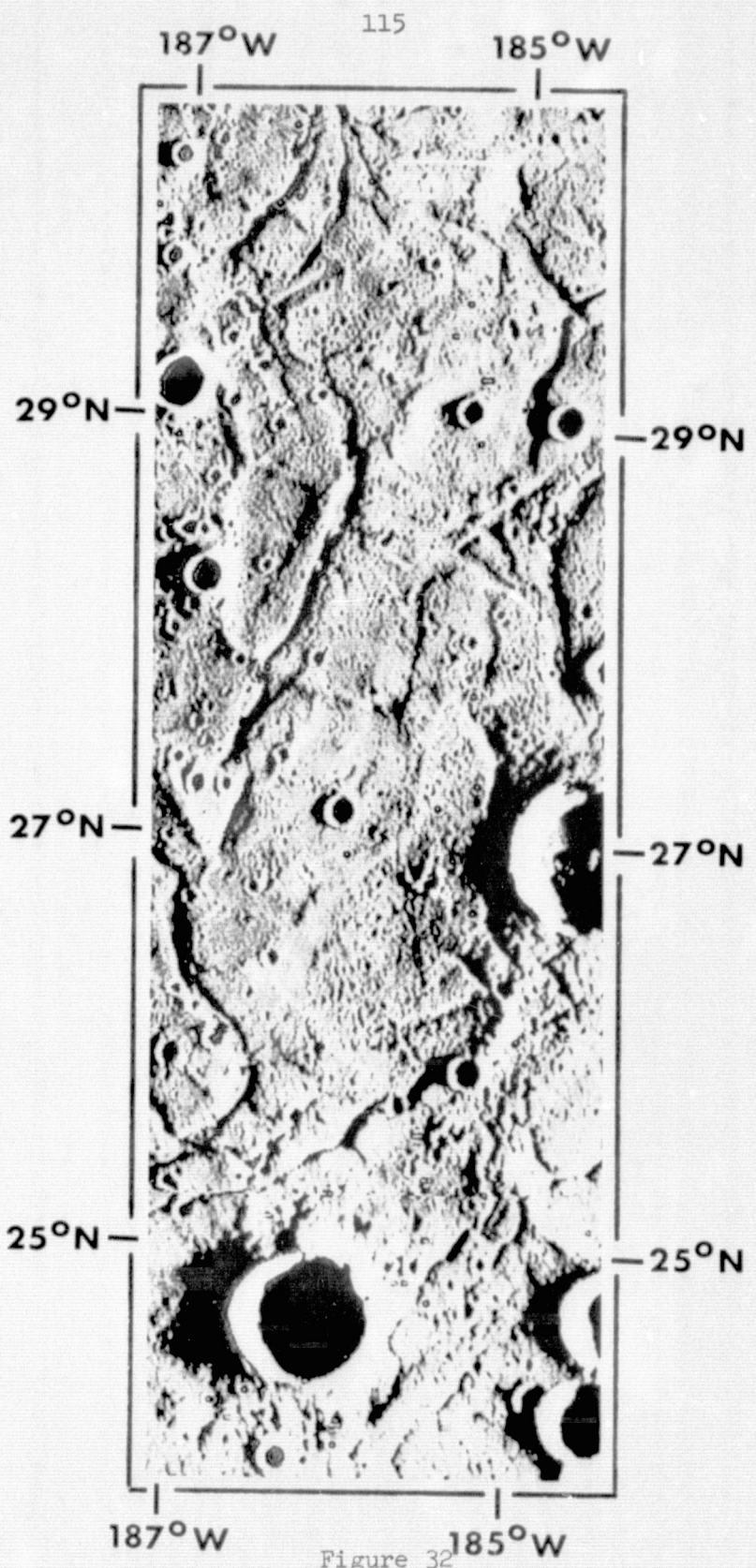
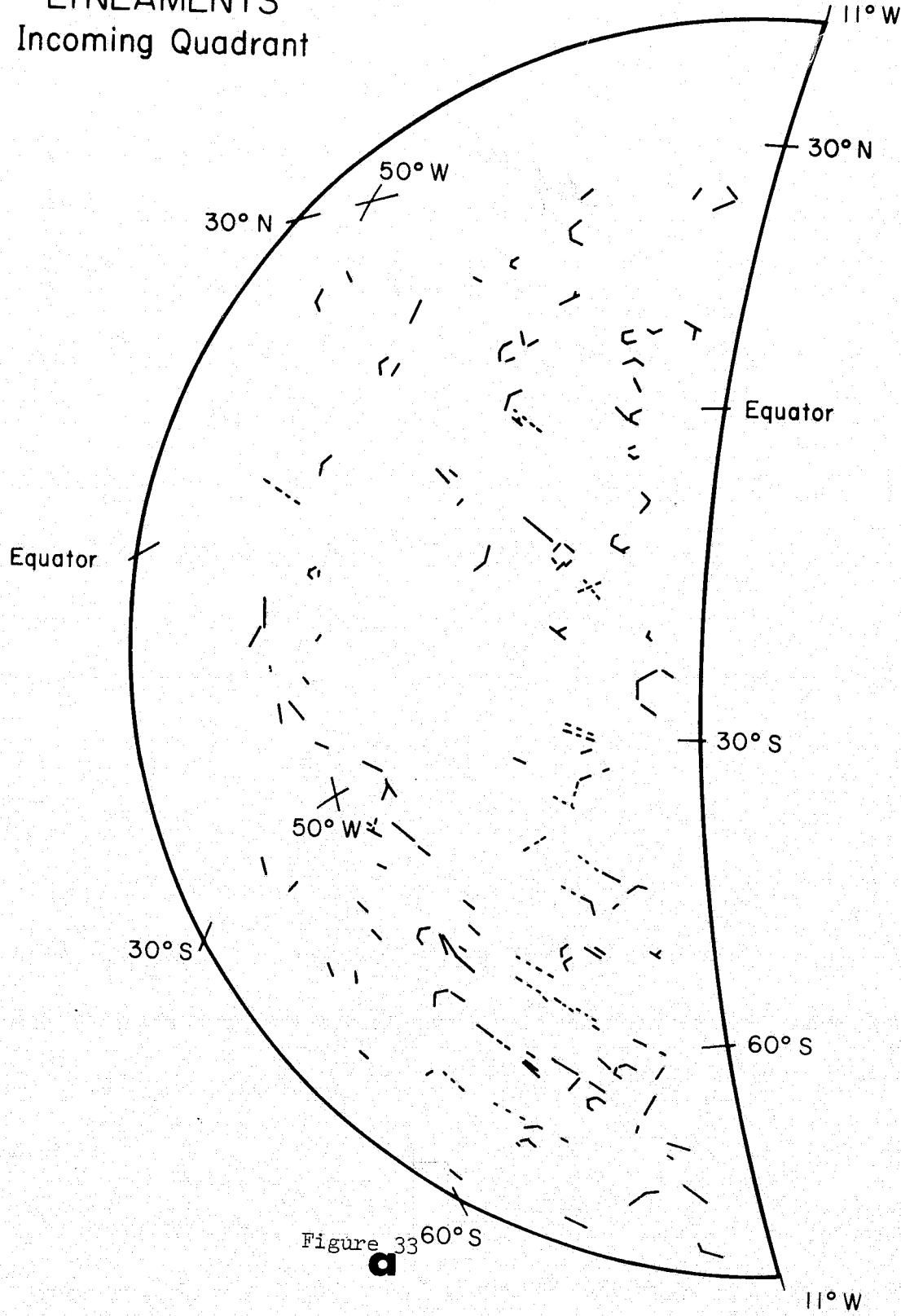


Figure 32

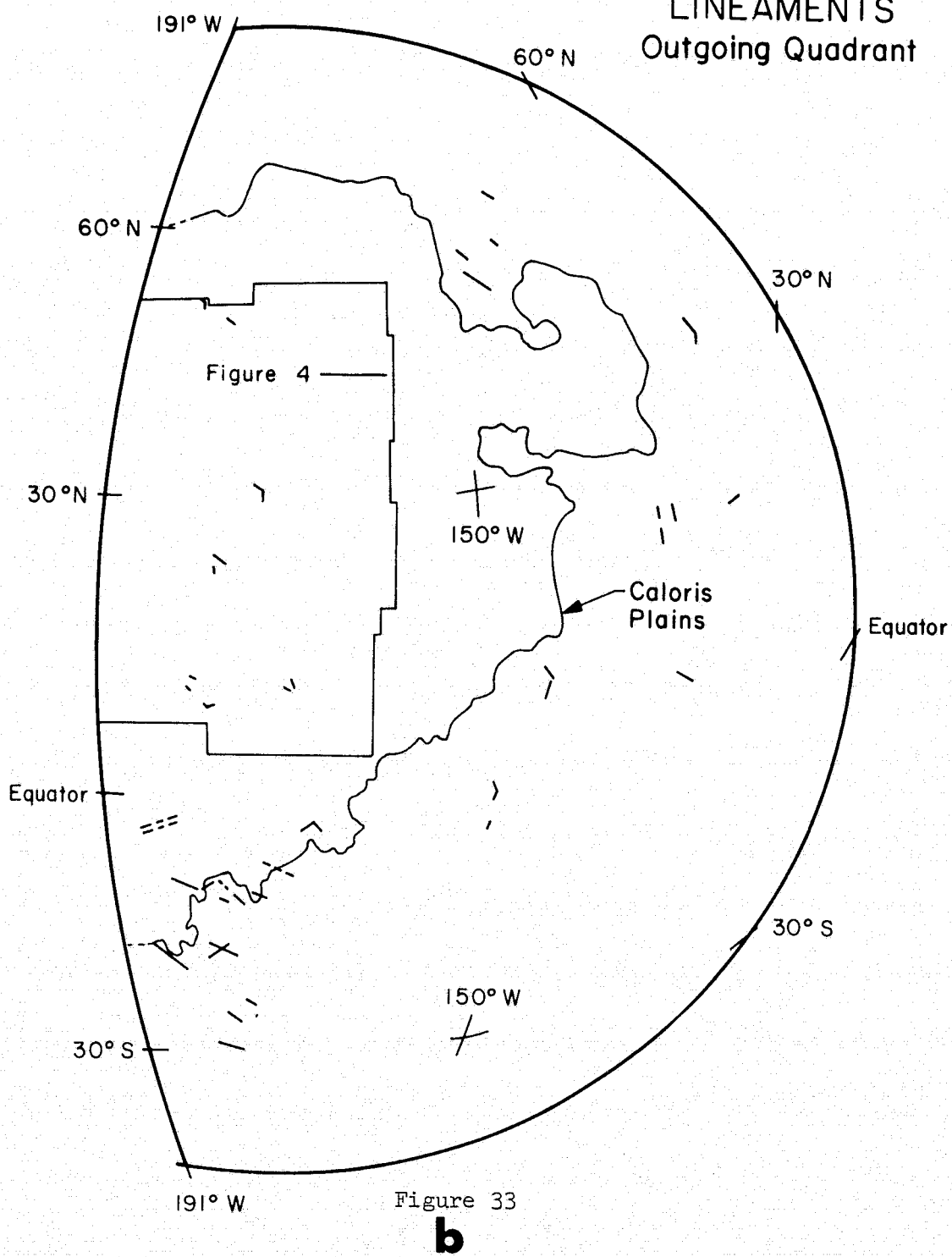
LINEAMENTS

Incoming Quadrant



LINEAMENTS

Outgoing Quadrant



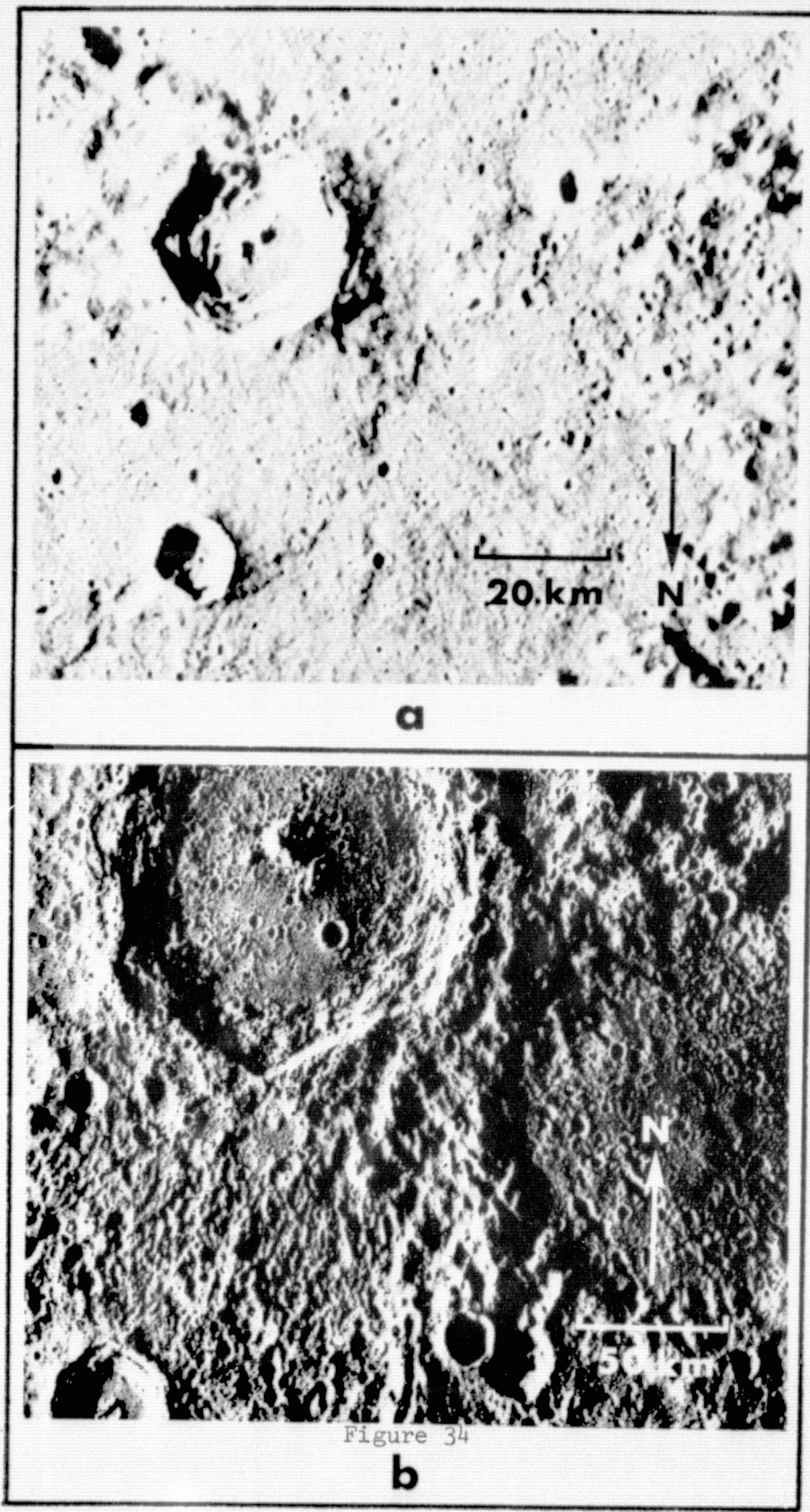


Figure 34

b

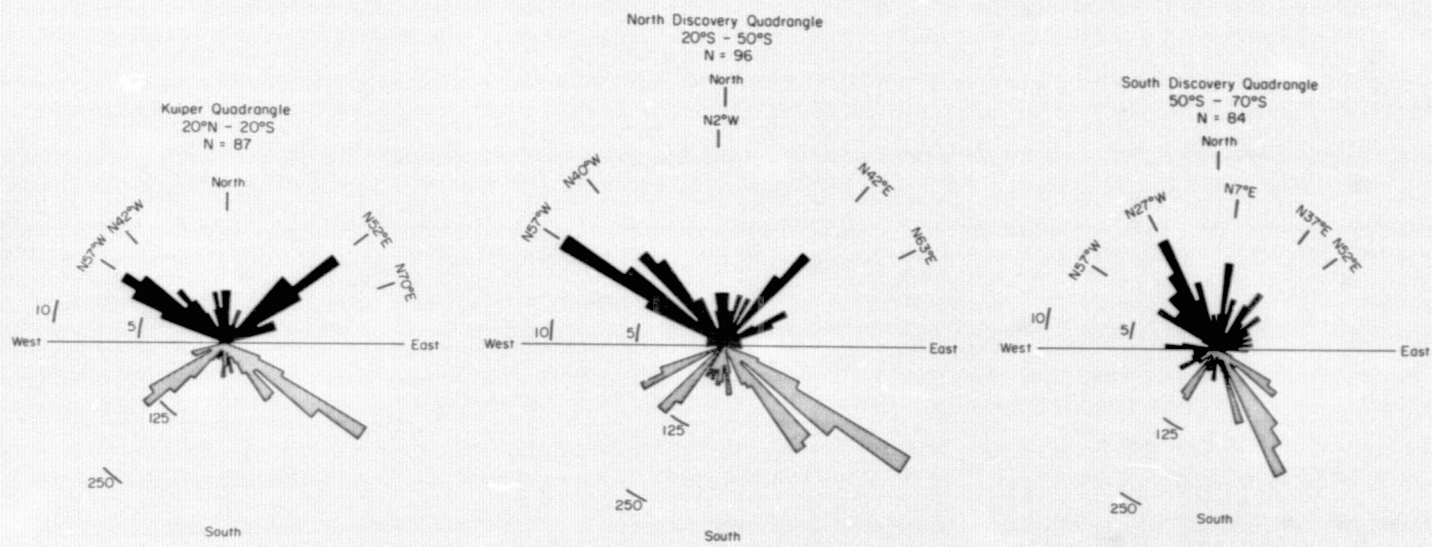
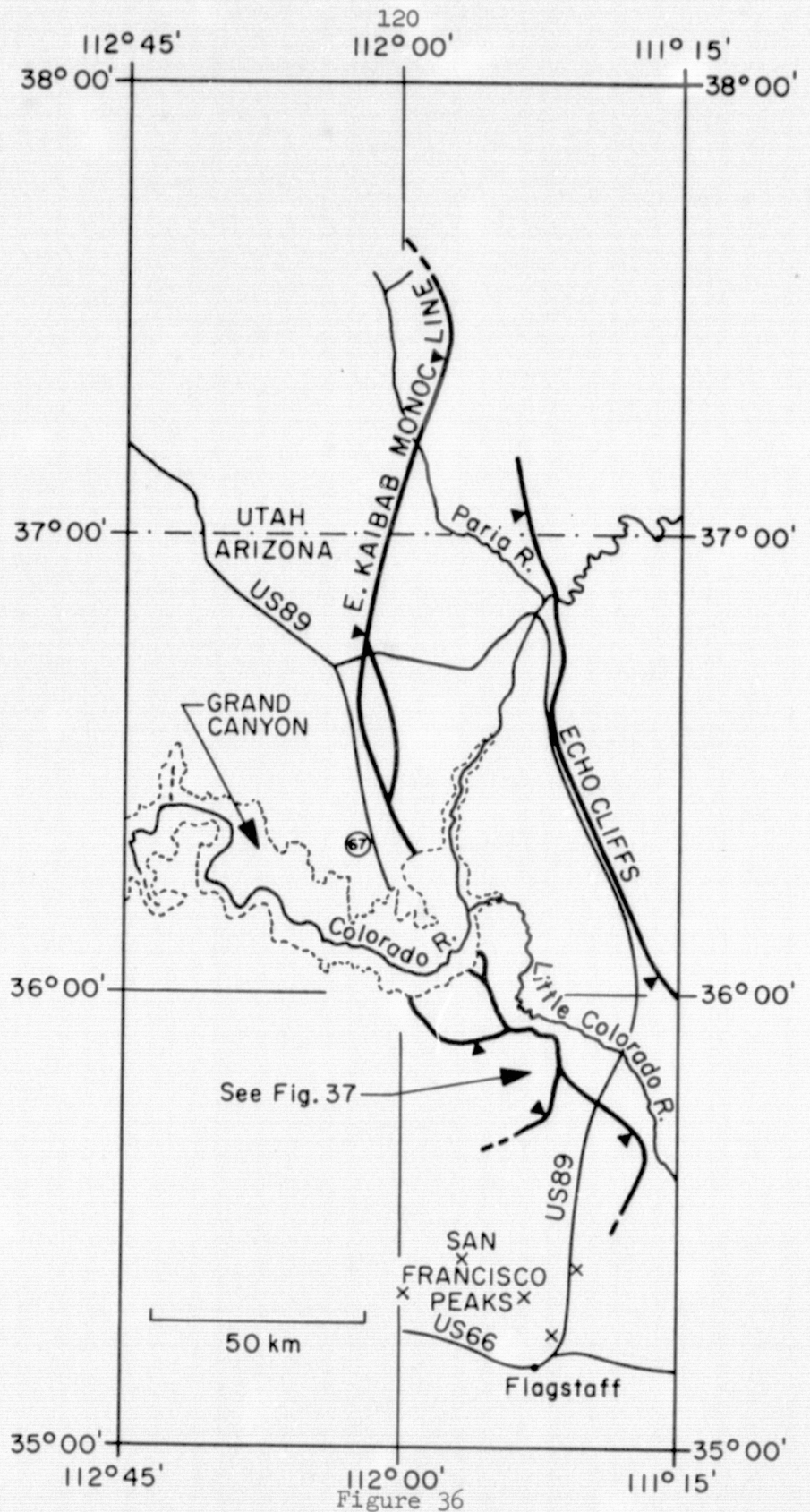


Figure 35



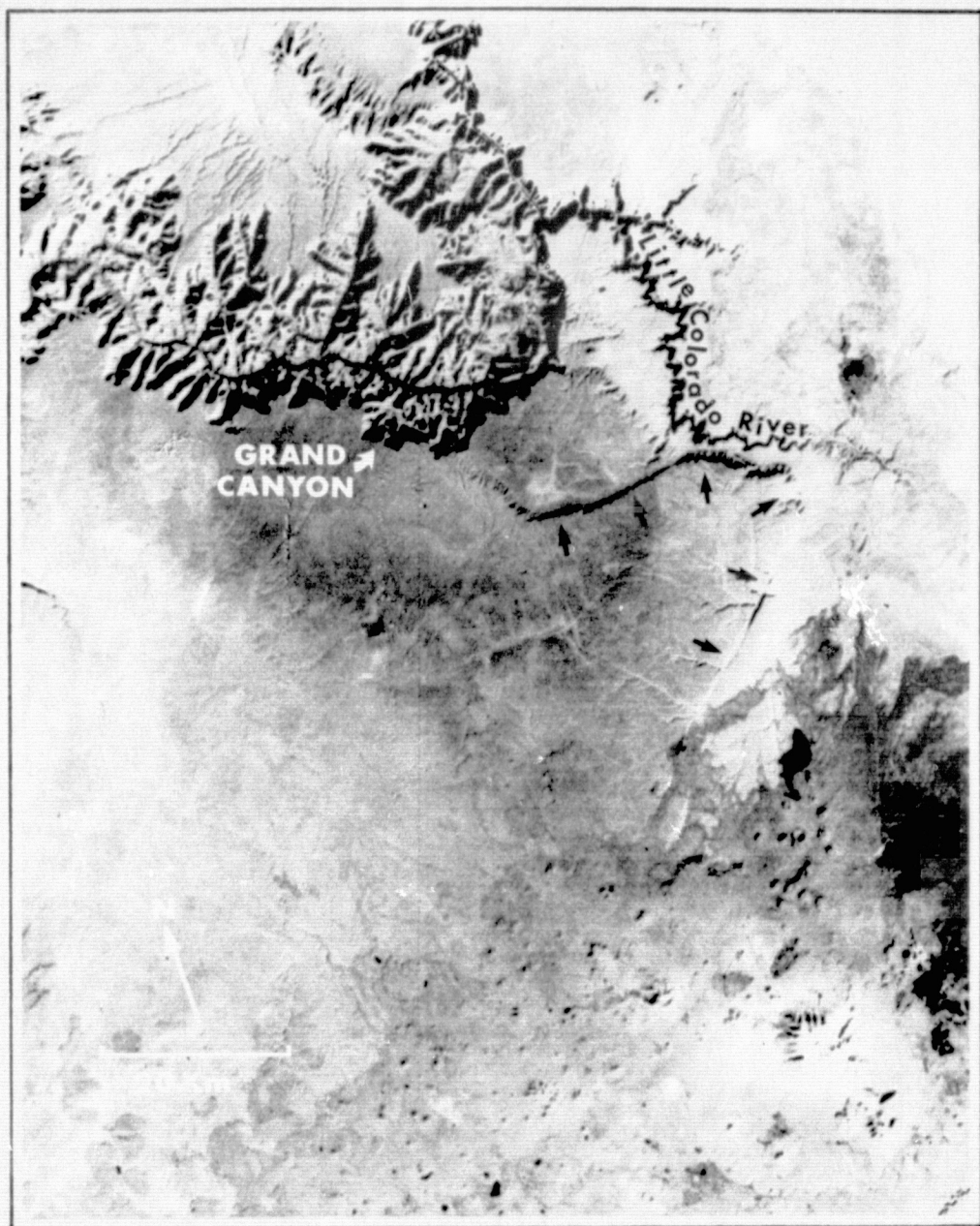


Figure 37

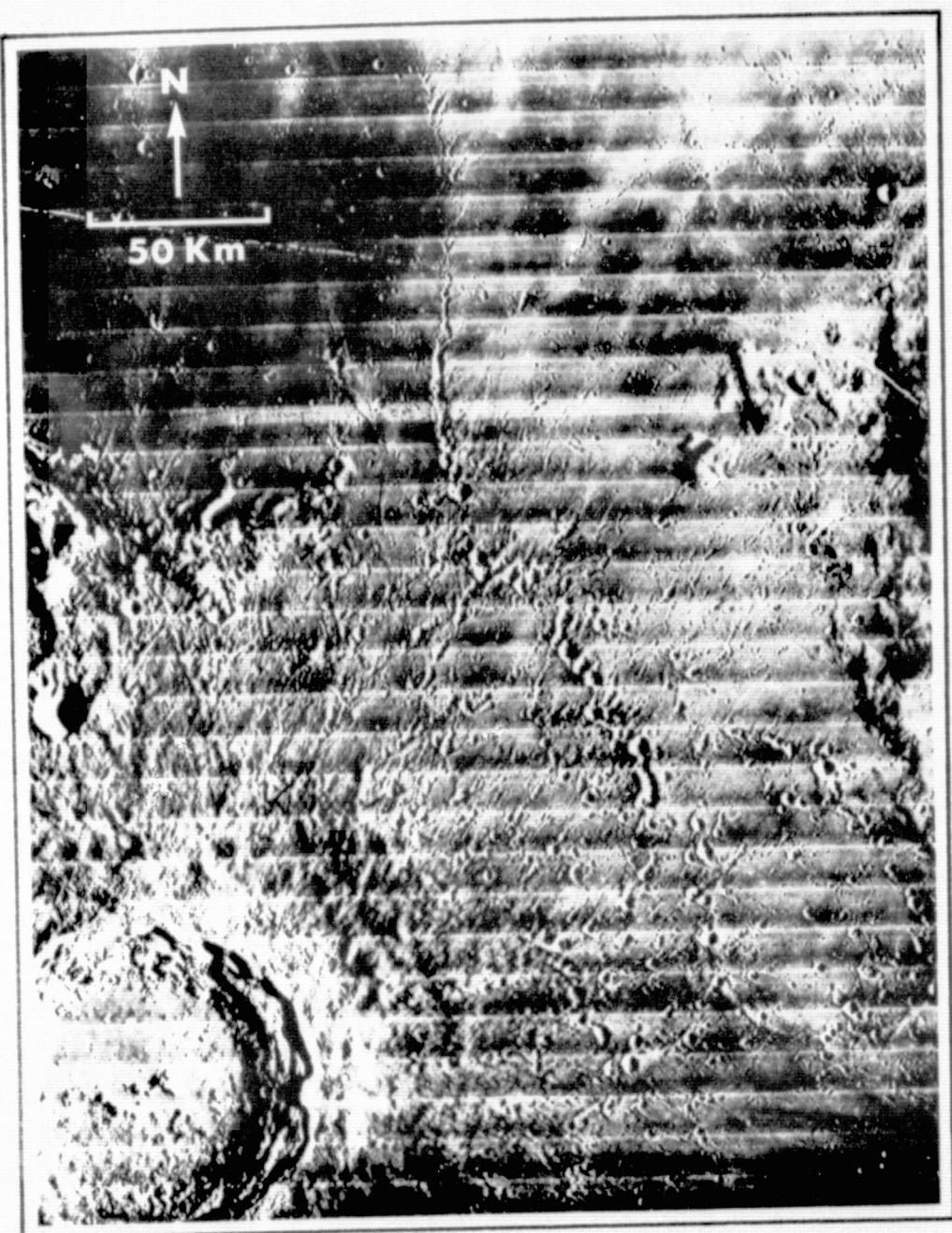


Figure 38

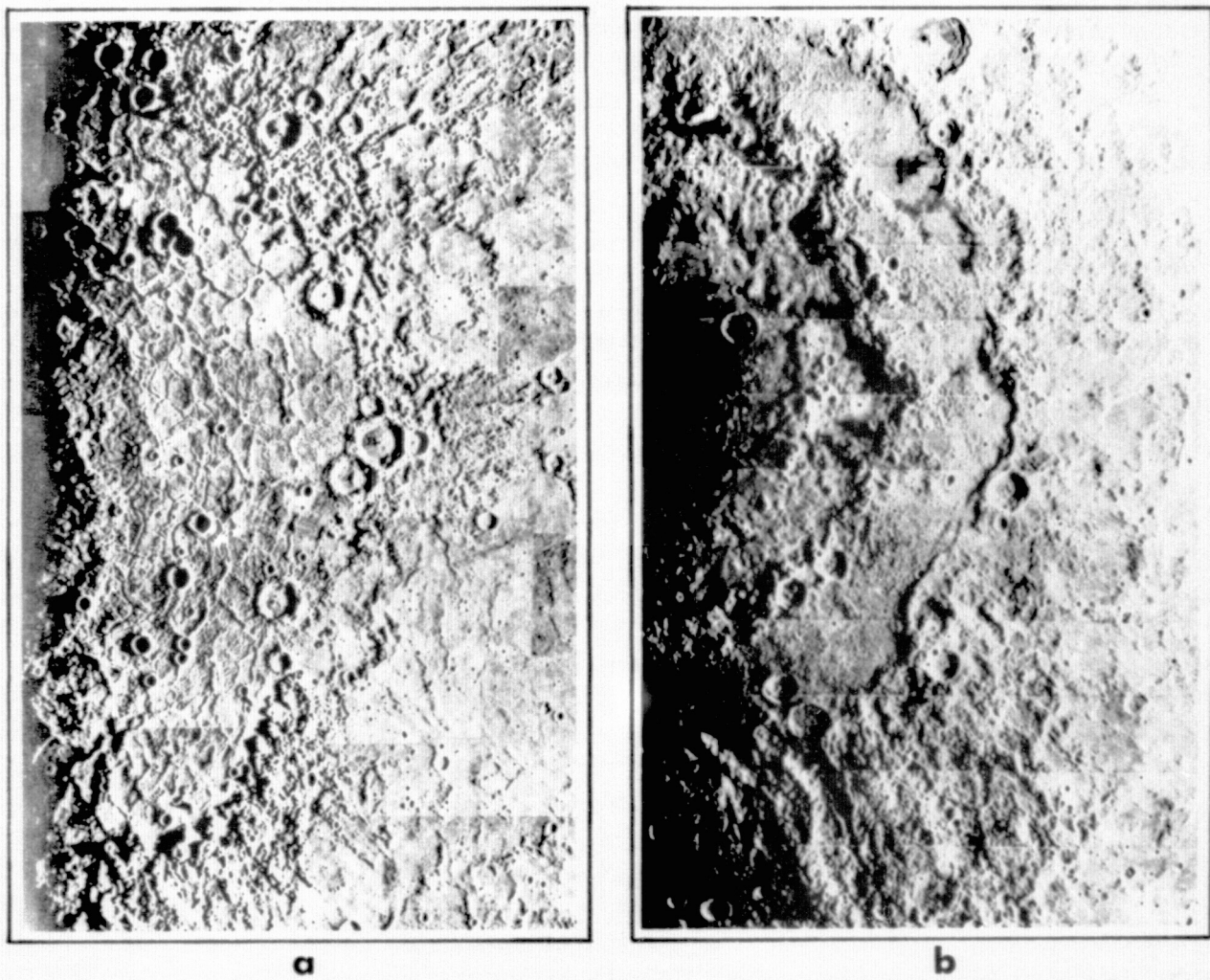
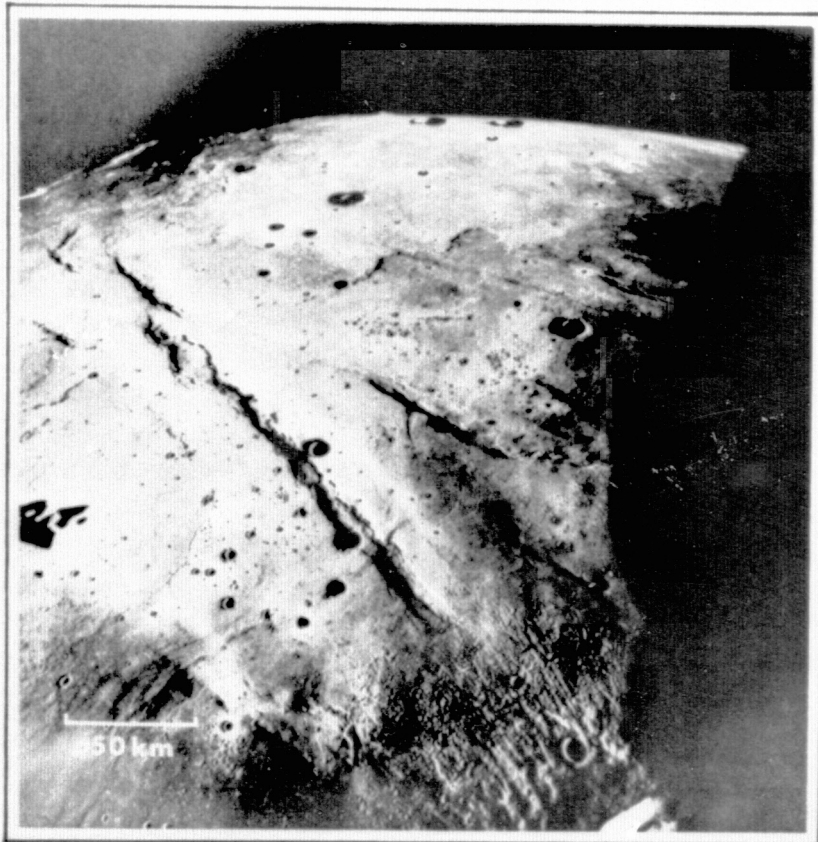
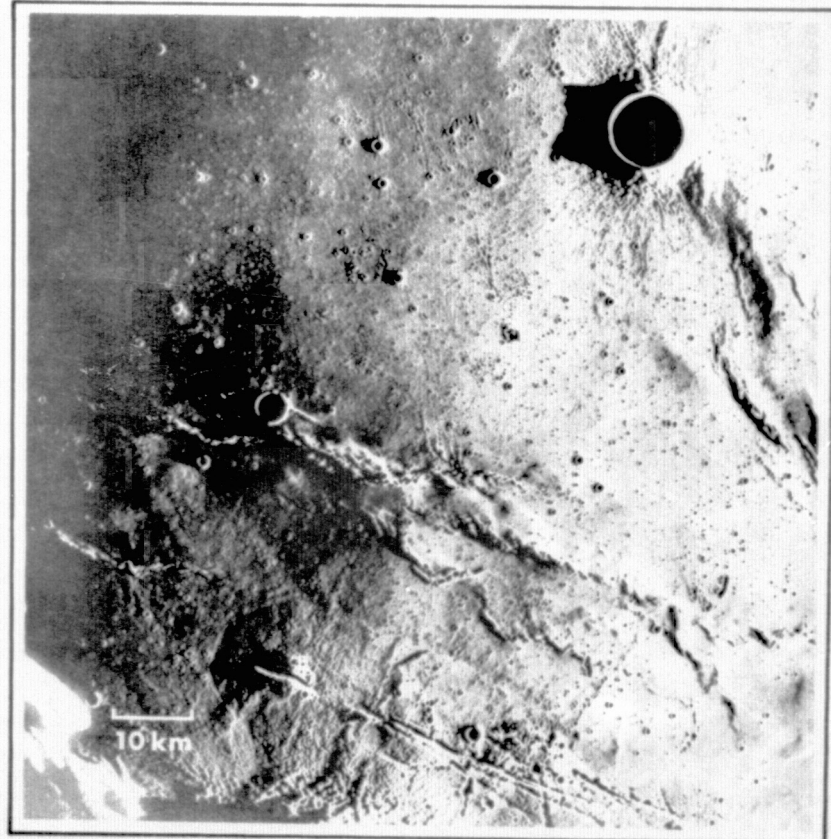


Figure 39



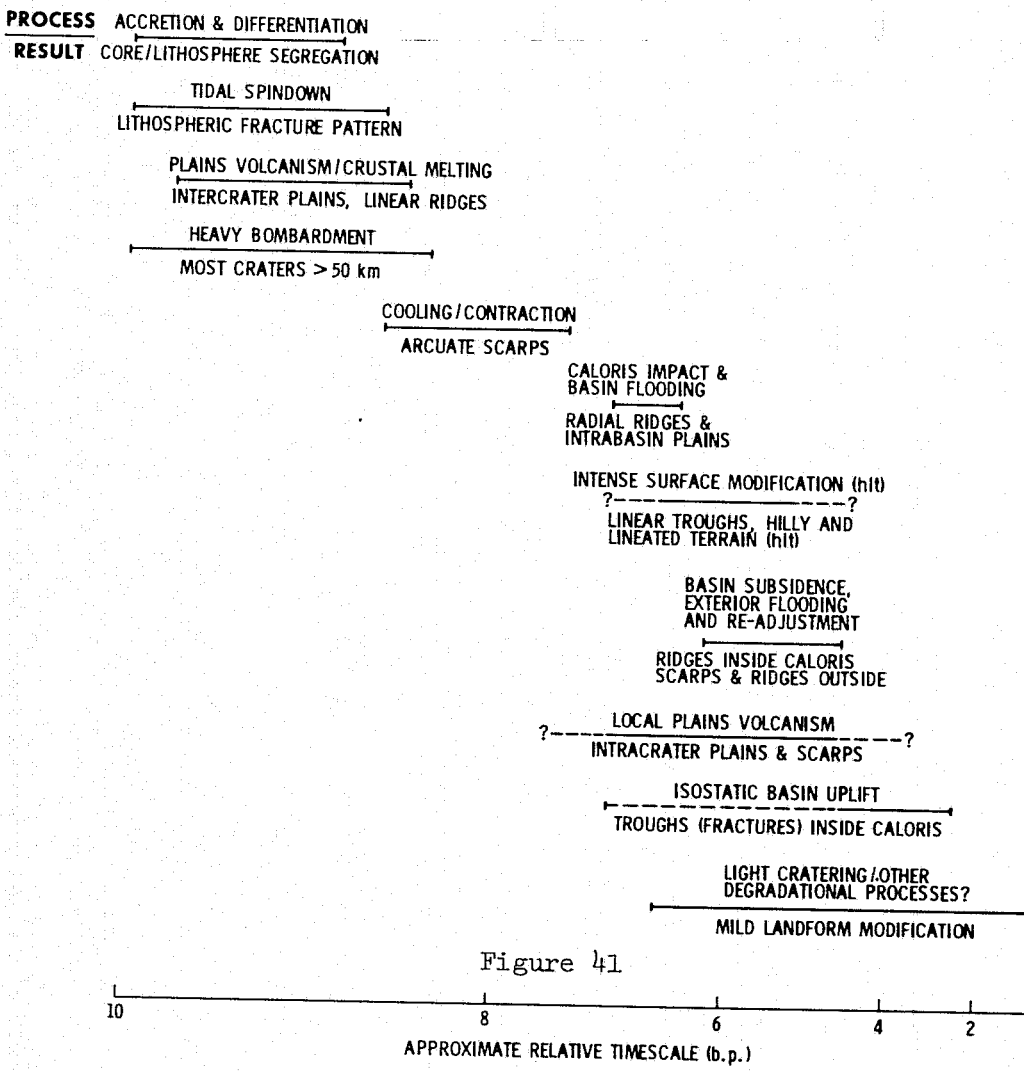
a



b

Figure 40

GENERALIZED CHRONOLOGY FOR MERCURY



PART 2

**Geologic Significance of Photometric
Variations on Mercury**

INTRODUCTION

Mariner 10 returned over 3000 high resolution images of the mercurian surface during encounters with the planet on 29 March 1974, 21 September 1974, and 16 March 1975. The Mariner 10 imaging system included dual 1500 mm focal length optical systems and an improved version of the selenium sulfur (Se-S) photo-surface slow-scan vidicon used on Mariner 9 (Danielson *et al.*, 1975). Design changes coupled with extensive pre-flight and in-flight calibration programs significantly upgraded photometric integrity of the Mariner 10 Se-S vidicon system.

Preliminary analysis of Mariner 10 photometric data by Hapke *et al.* (1975) included normal albedo calculations for 40 widely distributed areas on the mercurian surface. This paper revises and extends those calculations, presents computer-generated global photometric maps of Mercury, and discusses implications of photometric variations for mercurian surface materials and processes. Early sections of the paper treat data reliability, calculation of normal albedo, and production of global photometric maps from Mariner 10 data. These are followed by discussion and speculative interpretation of several characteristics of mercurian photometric observations. The paper's final section summarizes photometric results which bear on current debates concerning mercurian surface evolution.

DATAReliability

Prior to the Mariner 10 mission to Venus and Mercury, photometric observations of planets by spacecraft vidicon systems were subject to large uncertainties owing to system design limitations (Young, 1974). Problems such as nonlinear response to incident light intensity, non-uniform response to flat-field illumination, and residual image contamination owing to charge retention combined to discredit the vidicon as a photometric instrument. In the case of Mariner 10, however, extensive pre-flight and in-flight calibrations coupled with a novel approach to residual image suppression successfully reduced such difficulties to unprecedented low levels (Soha *et al.*, 1975).

Hapke (1976a) based conservative estimates of the reliability of photometric measurements from Mariner 10 on post-flight analyses of selected Mercury, Moon, Jupiter, and Venus images from the spacecraft (Table 1). Uncertainties are $\pm 3\%$ for relative accuracy within a single frame, and $\pm 10\%$ for absolute accuracy and for frame-to-frame comparisons. These estimates do not include uncertainties in the photometric function employed to calculate normal albedo from Mariner 10 radiance measurements. Accordingly, absolute albedo calculations are conservatively assigned an uncertainty of $\pm 20\%$.

Local Normal Albedos

An algorithm for calculating normal albedo from Mariner 10 television data has been outlined and applied to Mercury by Hapke *et al.* (1975). Normal albedo of a point on the mercurian surface is directly

proportional to radiance observed from that point:

$$A = \frac{R}{\varphi N} \quad (1)$$

where: A = normal albedo

R = observed radiance (watts/cm²/steradian)

φ = value of the surface photometric function at the appropriate phase angle (g).

N = radiance of a perfectly reflecting Lambert surface normal to incident solar illumination.

Hapke *et al.* (1975) averaged a constant number of data cells in several images of differing resolution to calculate local normal albedos. This introduces errors, because different surface areas are considered in each image. Observations suggest that albedo calculations depend strongly on image resolution (Hapke *et al.*, 1975). For these reasons, previously published albedo calculations have been revised and expanded. Results in Table 2 are averages of four independent calculations for each area - one each from the four highest resolution clear filter images available from Mariner 10's first two encounters with Mercury. These four calculations generally agreed to within 5% and never differed by more than 15%.

The albedo algorithm outlined above was applied to a constant 50 km x 50 km element of surface area in each image. This involved averaging roughly 25 data numbers (pixels) in lower resolution frames, and more than 100 data numbers in the highest resolution frames available. Radiance observed through the imaging system's clear filter

(effective wavelength = 487 nm, see Murray et al., 1974) was converted to predicted radiance at 554 nm using the whole-disk mercurian spectrum of McCord and Adams (1972). This facilitates comparisons with photometry of the Moon and other planets at the standard visual wavelength of the UBV photoelectric system (e.g., Pohn and Wildey, 1970; Lane and Irvine, 1973).

Polarimetric (Dollfus and Auriere, 1974) and photometric (Hapke et al., 1975) observations suggest that the mercurian surface is optically similar to that of the Moon. In particular, the photometric character of both bodies is seemingly determined in large part by ubiquitous, fine-grained regoliths generated by impacts. For the purposes of this paper, therefore, it was assumed that Mercury obeys the average lunar photometric function derived by Hapke (1966), without the correction for the lunar "opposition effect" (brightness surge near zero phase) introduced in equation (12) of that work. Gehrels et al. (1964) estimated that lunar brightness nearly doubles from $g = \pm 5^\circ$ to zero phase (see also Van Diggelen, 1965). More recent observations confirm that the change is at least 25%, but probably not more than 50% (Pohn et al., 1969). The potential existence of a similar effect on Mercury cannot be reliably evaluated from ground-based telescopic or Mariner 10 imaging observations. This uncertainty applies only to areas viewed at extremely small phase angles, however, and should not affect measurements reported in Table 2. Small discrepancies may exist between the lunar and mercurian photometric functions, at larger phase angles, however. The effects of multiple scattering or other unmodeled phenomena may contribute 10-15% error to results reported in Table 2 (Hapke, personal communication, 1976).

Global Photometric Maps

In addition to local albedo calculations, global photometric maps were generated through pixel-by-pixel application of equation (1) (Figures 2-5). Observed radiance is related to pixel data number by the imaging system's calibrated light transfer curve. Data numbers can therefore be translated into normal albedos on a pixel-by-pixel basis, yielding photometric maps from optical images. An automatic algorithm to perform this calculation has been applied to 23 medium resolution clear filter frames (Table 3) at the Image Processing Lab of NASA's Jet Propulsion Laboratory. Intermediate products include radiometrically decalibrated (Figure 2) and phase normalized (Figure 3) versions. The following brief descriptions of image processing techniques are intended to enhance the utility of these maps. For a more detailed treatment of image processing techniques applied to Mariner 10 images, the reader is referred to Soha *et al.* (1975).

- 1) Figure 2 - Bit error compensation and radiometric decalibration are the first steps toward production of global photometric maps. Pixel data numbers were converted to equivalent observed radiance using decalibration files generated before launch. As noted above, absolute accuracy of this procedure is estimated to be $\pm 10\%$ at the pixel level.

To within this uncertainty, Figures 2a and 2b are accurate relative radiometric representations of Mercury, i.e., they duplicate the appearance of the planet as seen by Mariner 10 except for contrast enhancement by a factor of roughly 2.5.

2) Figure 3 - Compensation for terminator-to-limb brightness variations owing to changes in illumination angle was accomplished by assuming that the mercurian surface obeys the whole disk lunar photometric function (Hapke, 1966). An alternate approach is to use the average mercurian photometric function derived by ground-based observers (Irvine *et al.*, 1968; Danjon, 1948), but this complicates direct comparisons of Mercury and the Moon. Differences between the observed mercurian photometric function and that used here are generally less than the 10% uncertainty in Mariner 10 absolute photometry. The purpose of this study is to evaluate photometric variations on Mercury in terms of surface properties and processes. Such variations may reflect differences in surface albedo, photometric function, or both. They presumably reflect differences in age, surface composition, or other surface parameters, all of which are geologically significant. Accordingly, the lunar photometric function was used to facilitate comparison of relative photometric variations on Mercury and the Moon. Regardless of potential errors in the photometric function applied, the images in Figure 3 can usefully be regarded as accurate photometric maps of the mercurian surface, combining normal albedo information with that on local deviations from an average (lunar) photometric function.

3) Figures 4 and 5 - To simplify visual interpretation, the images in Figure 3 have been contoured in equal increments to produce Figures 4 and 5. If brightness variations in Figure 3 reflect real albedo differences and not variations in the surface photometric function, these increments correspond to normal albedo changes of .065 .

Average Normal Albedo

The average normal albedo of Mercury at 554 nm, calculated from equation (1) using the arithmetic mean of data numbers comprising the images in Figure 3, is $.16 \pm .03$. This is roughly 40% higher than the corresponding lunar value (Pohn and Wildey, 1970). However, ground-based photometric and polarimetric results suggest that the reflectivities of Mercury and the Moon are comparable (Table 4). Harris (1961) reported a geometric albedo for Mercury at 554 nm of .10 from photometric observations. Dollfus and Auriere (1974) used polarimetric results to derive a geometric albedo at five degrees phase angle of .125 . For the Moon, values of the geometric albedo range from .113 (Lane and Irvine, 1973) to .125 (Dollfus and Titulaer, 1971; see Table 4). These results suggest that the mean normal albedo for Mercury reported here may be in error owing to differences in photometric function between the Moon and Mercury, or to unmodelled effects such as multiple scattering. Recent studies by Hapke (personal communication, 1976) indicate that a more careful treatment of multiple scattering on Mercury greatly reduces the apparent discrepancy in normal albedo for Mercury and the Moon.

DISCUSSION

Several distinctive features of mercurian photometric data which bear on current debates over the planet's surface evolution are discussed below. These include: 1) general lack of photometric contrast between and within intercrater plains, heavily cratered terrain, and Caloris plains units; 2) small local variations associated with two mercurian escarpments; 3) existence of both bright and dark smooth plains; and 4) high albedo and distinctive morphology of several localized patches inside large craters.

1. Similarity of Heavily Cratered Terrain, Intercrater Plains, and

Caloris Plains

Perhaps the most striking feature of mercurian photometric maps is the relatively consistent apparent brightness of heavily cratered terrain, intercrater plains, and Caloris plains as mapped by Trask and Guest (1975; Figures 4-6). It is unlikely that differences in photometric function between these units compensate for albedo variations to produce the observed similarity. Hence, all three units are probably of similar albedo. With the exception of superposed bright ray material associated with very fresh craters, intercrater plains and heavily cratered terrain in general constitute a photometrically uniform surface ranging from .13 to .18 in normal albedo. These units are photometrically indistinguishable from younger smooth plains near Caloris, both inside and outside the rim of that basin. Although near-terminator artifacts introduced by computer processing suggest that plains inside Caloris basin are bright relative to their surroundings

(Figure 5), individual local albedo measurements indicate no significant difference between plains units interior and immediately exterior to the basin. These plains exhibit a combined normal albedo range of .12-.18 (Table 2).

Murray *et al.* (1975) and Strom *et al.* (1975) concluded that smooth plains in and around Caloris Basin formed by lava extrusion in a manner similar to that envisioned for lunar mare formation. On the Moon, significant photometric contrast exists between relatively dark maria and neighboring terra surfaces (Pohn and Wildey, 1970). This is not the case for Mercury, where no significant correlation exists between albedo and physiographic province. However, the net range in albedo exhibited by mercurian heavily cratered terrain, intercrater plains, and Caloris plains is comparable to the combined range for mare and terra surfaces on the Moon. If the volcanic hypothesis for emplacement of Caloris plains is to be accepted, future volcanic models for their genesis must account for the apparent discrepancy between the photometric character of those plains and that of the lunar maria.

One potential explanation invokes the action of some surface process which effectively masks lunar-like photometric boundaries on Mercury. Eolian redistribution of material by an early atmosphere on Merucry could have subdued regional photometric contrasts, but no independent evidence for an ancient mercurian atmosphere has been reported. Malin and Dzurisin (1976) inferred from crater morphology studies that mild surficial modification of mercurian landforms by processes other than impact cratering has occurred on Caloris plains

since formation of Caloris Basin. This degradational process could conceivably have caused sufficient redistribution of surficial material to mask preexisting albedo boundaries, but this cannot be demonstrated at present. Clearly, albedo studies alone cannot distinguish between models which explain the present photometric character of Caloris plains as a primary feature of their genesis and those which invoke secondary alterational processes. However, lack of lunar-like, terrain correlated photometric boundaries on Mercury provides an important constraint on future models for genesis of Caloris plains.

2. Photometric Variations Across Escarpments

No significant photometric contrast exists across most planimetrically arcuate or lobate escarpments on Mercury (Figure 4, B, H, K, M; Figure 7). This is consistent with the tectonic origin for these features inferred from morphologic studies (Dzurisin, 1976; Strom *et al.*, 1975). Two notable exceptions are shown in Figures 8 and 9.

An expanse of intercrater plains in Figure 8 is distinguished from the smooth floor of a 200 km double ring basin by the former's seemingly lower albedo ($A = .17$ vs. $.23$) and irregular, pitted surface. This surface is bounded by low escarpments which transect both rims of the basin, and that of an 80 km degraded crater to the southeast (Figure 8, arrows). Stereo images reveal that both rims are topographically continuous through the visually obscured areas, suggesting that preexisting topography has been mantled by material comprising the pitted unit. Several lineaments within that unit parallel nearby

elements of a global lineament pattern interpreted to reflect a system of linear crustal fractures (Dzurisin, 1976). Combined with transectional evidence noted above, this suggests that the pitted plains unit may have formed through eruption from preexisting fractures of lava or ash which covered and thereby subdued local topography. In this scenario, photometric contrast between the pitted unit and its surroundings is attributed to differences in composition and/or surface texture.

Figure 9 shows the northern part of a planimetrically lobate escarpment which transects and obscures arcuate Resolution Scarp. To the southeast, parts of the rim and floor of a 70 km crater are visually obscured immediately above this escarpment. Stereoscopy reveals that obscured segments of the crater rim and Resolution Scarp are topographically continuous with their unobscured extensions. The surface immediately above the lobate scarp slopes gently upward to the southwest for roughly 25 km as a ramp which terminates in a broad ridge parallel to the basal scarp (Dzurisin, 1976). Photometric shading owing to this regional slope is apparent in Figure 9b. In addition, the lobate scarp and parallel ridge separate expanses of intercrater plains which differ in photometric character. These observations suggest that material bounded by the lobate scarp has mantled and subdued pre-existing topography. Volcanic extrusion along linear crustal fractures is the mechanism favored to explain these photometric and transectional relationships (Dzurisin, 1976).

3. Bright and Dark Smooth Plains

Local areas of relatively bright ($A \approx .23$) smooth plains on Mercury can be distinguished from darker smooth plains flooring many large craters, and from plains in and around Caloris Basin (Hapke *et al.*, 1975; Table 2). Except for areas overlain by bright ray material, all mercurian bright plains are confined within large craters. Predominance of darker smooth plains ($A \approx .13$) inside craters argues that formation of bright plains is not inherent in the cratering process (e.g., impact melt). Absence of smooth plains with intermediate albedos indicates that bright and dark plains are not merely end points of a continuous series. Relative densities of superposed small craters indicate that bright plains are not systematically younger or older than dark plains, suggesting that dark plains do not evolve into bright plains, or bright into dark (Figure 10). Subject to these constraints, three plausible mechanisms for creation of bright smooth plains on Mercury are discussed below: (1) superposition of smooth crater floors by bright ray material from nearby impacts, (2) accumulation of impact-mobilized debris in preexisting depressions, and (3) emplacement by lava extrusion.

The existence of small, fresh craters superposed on light plains in several areas (e.g., Figures 4 and 5, C, E, J, L) suggests that bright ray material may contribute to the elevated albedo of some smooth plains. Studies by Oberbeck (1971) suggest that rays are produced primarily by disturbance of in situ material by very low-angle ejecta generated by primary impacts. Distribution of such

ejecta would presumably be strongly influenced by local topography, and restriction of rays inside a preexisting crater or basin floored by dark plains is thus a plausible mechanism for production of high albedo plains. The floor of crater E in Figure 4, for example, reflects the influence of Kuiper (crater D) ray material, and bright plains enclosed by the inner rim of basin C can be reasonably interpreted as a thin veneer of ray material from a nearby, fresh impact.

This hypothesis fails in general, however, for two reasons.

Fresh craters with clearly defined rays display concentric, filamental haloes of bright material which progressively increase in albedo toward the crater rim (Figures 4 and 5). In several cases, small craters superposed on bright plains do not display this characteristic pattern, suggesting that they were not the source of bright material for the plains. In addition, no potential source craters superpose the bright floors of craters I or N in Figures 4 and 5. It therefore seems unlikely that superposition by ray material can account for the existence of mercurian bright plains in general.

Selective accumulation in topographic depressions of impact-mobilized debris has been proposed as a mechanism to produce smooth plains in some lunar and mercurian craters (Wilhelms, 1976; Oberbeck *et al.*, 1975). An impact origin cannot be ruled out for some darker smooth plains inside mercurian craters, but the absence of source craters in some cases and lack of bright plains outside craters are difficult to reconcile with such an emplacement mechanism for bright plains. It seems implausible that transportation of ground hugging

ejecta over hundreds of kilometers to collect in preexisting craters would leave terrain immediately outside the rim entirely unaltered. Deposition or disruption of only a few millimeters of surface material would drastically affect surface photometric properties, and this is not observed. Thus, a nonimpact, intracrater origin is favored for production of mercurian bright plains.

Strom *et al.* (1975) have inferred a volcanic origin for the bulk of intracrater smooth plains on Mercury, and Trask and Guest (1975) conclude that at least some probably represent sheets of flood lavas broadly similar in origin to lunar maria. Although the origin of intracrater smooth plains on Mercury cannot be conclusively demonstrated, the existence of both bright and dark intracrater plains is most easily reconciled with the volcanic hypothesis advanced by others. Lateral restriction of bright plains inside craters may reflect control of extrusion sites by impact-induced fractures. Flood lavas erupted from such fractures would likely produce flat, featureless plains which abut the surrounding crater rim abruptly, similar to those seen on Mercury. Albedo of intracrater plains on Mercury is most likely controlled by chemical composition, which may reflect the degree of differentiation in parent magma bodies. Although consistent with available morphologic and photometric observations, this volcanic scenario for formation of smooth plains on Mercury remains highly speculative, and must be examined in light of other evidence for both Mercury and the Moon.

4. Localized Bright Patches

A final aspect of photometric results for Mercury which merits discussion is the existence of several localized, photometrically anomalous patches of surface material which may exhibit normal albedos as high as 48% (Figures 4 and 5, A, F, O, Q, R, S; Figure 11; Table 2). These patches are generally localized within relatively large ($D \geq 50$ km) craters, and can be distinguished from bright ray deposits by the former's well-defined, relatively abrupt contact with surrounding material.

In several cases (Figure 11 C, D), bright patches form discontinuous but distinct ring of U-shaped patterns tens of kilometers in extent which are roughly concentric with the surrounding crater rim. Those identified to date are broadly restricted between latitudes 20° N- 20° S and longitudes 55° W- 145° W, although this may simply reflect the combined effects of limited viewing and lighting conditions in available photography. Except for the floor of Kuiper crater, all bright patches were viewed at relatively high sun elevation angles (39° - 52°). Viewing angles for high resolution photographs ranged from 38° to 70° at phase angles from 71° to 103° (Table 5). There is a tendency for bright patches to be associated with dark haloed craters (Figure 11 C, D), although the floor of Kuiper crater and the patch shown in Figure 11b are notable exceptions. Stereo photography indicates no substantial relief associated with most bright patches, and suggests they are relatively thin surficial units. Color ratio images of Mariner 10 orange ($\lambda_{\text{eff}} = 575$ nm) and UV ($\lambda_{\text{eff}} = 355$ nm) frames indicate that bright patches are in general more reflective in blue light, and are

surrounded by crater floor material and, in some instances, by dark haloes which are more reflective in red, both with respect to typical mercurian plains material (Figure 12). Calculations of normal albedo for bright patches on Mercury range from .37 to .48, assuming they obey the average lunar photometric function. These measurements exceed those reported for the brightest regions on the Moon by roughly 70% (Pohn and Wildey, 1970). This difference may reflect in part significant local departures of mercurian bright patches from the average lunar photometric function. This occurs on the Moon for bright craters and rays, for which multiple scattering becomes important. This effect is not included here. For this reason, the following discussion focuses on qualitative characteristics of mercurian bright patches, including their high relative albedo, distinctive morphology, and color relationships with surrounding plains units.

The existence of relatively high albedo material on Mercury in localized patches with distinct outer boundaries requires either that the material was produced in place, or that it was produced elsewhere and subsequently transported to, and perhaps concentrated in, its present location. Production of high albedo material on the Moon is generally attributed to pulverization by primary impacts, and disruption by secondary ejecta, of near-surface materials. This mechanism has undoubtedly been active on Mercury, producing well-developed ray systems around fresh craters. Bright patches are distinct from such ray patterns both in form and apparent albedo, however, and alternate mechanisms for their production are therefore discussed below.

On Earth, sources of bright material are both numerous and varied.

Multiple reflections from relatively fine-grained material such as beach sand, playa deposits, frozen volatiles, and some evaporites commonly produce normal albedos in excess of 50%. Specular reflection from crystal faces, from cleavage planes in sheet silicates such as mica, or from natural pavements common in desert environments can result in relatively high reflectivity at certain phase and viewing angles. Local erosion of dark/light stratigraphy, chemical weathering of silicates to clay minerals and silica wreckage, alteration of parent rock by fumarolic action, accumulation of salts around fumaroles, and precipitation from solution all produce localized areas of high albedo material on Earth.

However, environmental constraints combined with photometric observations outlined above preclude many potential genesis mechanisms for material comprising bright patches on Mercury. The planimetric forms and distribution of bright patches are inconsistent with a ballistic origin such as that invoked to produce lunar rays, at least in the absence of some process to selectively concentrate bright material on the floors of only a few large craters. Frozen deposits of common volatiles are implausible in the present mercurian environment, and chemical weathering or evaporite formation in general require the presence of water or some other suitable solvent.

One potential explanation of the distinctive albedo, color, and distribution of mercurian bright patches involves deposition around fumaroles of high albedo salts and chemical alteration of silicates to

clay minerals by acid fumarolic gases. Ammonium, aluminum, and ferric chlorides commonly form high albedo deposits around terrestrial fumaroles whose gases include significant amounts of HCl. Calcium, potassium, and magnesium sulfates are also common, as are minor amounts of metallic chlorides, sulfates, or oxides. Alteration of parent rock through leaching by HCl, H_2SO_3 , and H_2SO_4 derived from volcanic gases commonly produces fine-grained clay minerals and hydrated iron oxides, sometimes with lesser amounts of hydrated metal sulfates. When leached iron and magnesium compounds can be mobilized by percolating water, the resulting residue of clay minerals produces a white to cream-colored deposit which is highly reflective owing to multiple reflections from fine-grained materials. Such deposits are in general bluer than the rocks from which they were derived, since iron and magnesium, which absorb strongly in the blue, have been preferentially removed. Mobilized iron and magnesium compounds are generally redder than their parent rocks for the same reason.

In summary, fumarolic activity on Earth typically involves deposition of high albedo salts and leaching of silicates to produce:

- 1) high albedo clay deposits which are blue relative to unaltered silicates, and 2) relatively low albedo iron and magnesium compounds which are red relative to unaltered silicates, and which are typically removed from the immediate vicinity of the fumarole by percolating ground water. The observation of relatively blue, high albedo patches surrounded by relatively red, darker materials on Mercury suggests a potential origin through fumarolic activity. Restriction of bright

patches to crater floors and their ring or U-shape may reflect control by impact-induced fractures which have acted as vents for fumarolic gases. An interesting note in this regard is that the majority of bright patches on Mercury occur inside craters formed in smooth Caloris plains, which have tentatively been interpreted as volcanic in origin (Strom et al., 1975; Trask and Guest, 1975; Murray et al., 1975).

Although fumarolic activity successfully explains several otherwise perplexing characteristics bright patches on Mercury, there remain a number of substantial difficulties with this interpretation. Many salts typically associated with terrestrial fumaroles would decompose or rapidly sublime in the mercurian thermal environment, suggesting that these do not contribute to the elevated albedo of mercurian bright patches. Mobilization by percolating ground water is implausible on Mercury, where another mechanism is required to segregate dark iron and magnesium compounds from bright clay minerals. Chemical alteration or slow volitization are potential alternatives. Mercurian bright patches are many times larger than typical terrestrial fumarole fields, and no unambiguous evidence for associated volcanic landforms in Mercury has been identified. Finally, current models for planetary accretion suggest that Mercury is extremely depleted in most volatiles commonly associated with terrestrial fumaroles. Although chemical alteration along fractures remains a viable explanation for many characteristics of mercurian bright patches, these difficulties suggest that alternatives to Earth-analogous fumarolic activity merit consideration.

SUMMARY

The mean normal albedo of Mercury, assuming an average lunar photometric function and ignoring the effects of multiple scattering, is $.16 \pm .03$. Lack of terrain-correlated photometric variations on Mercury may indicate that much of the surface was chemically homogeneous at formation, or that some process has obscured photometric boundaries. Local deviations from the mean mercurian albedo most often are associated with fresh craters and rays, and probably record comminution of surface material by primary impacts and disruption by secondary ejecta. However, the existence of both bright and dark intracrater plains, regional photometric contrast associated with two escarpments, and localized patches of morphologically distinct, high albedo material in several craters are not easily explained by impact-related processes.

Fissure eruption of flood-type lavas through impact-induced fractures is the mechanism most easily reconciled with available morphologic and photometric observations of mercurian intracrater smooth plains, and transectional relationships with preexisting craters and scarps suggest that at least some intercrater plains on Mercury formed by extrusion from older crustal fractures. Finally, although details of their origin remain unclear, several well-defined patches of photometrically anomalous material are best explained as products of local chemical alteration, perhaps associated with fumarolic activity along impact-induced fractures.

REFERENCES

- Danjon, A., Photometry and Colorimetry of the Planets Venus and Mercury,
Bull. Astr., 14, 315-345, 1948.
- Danielson, G.E., Jr., K.P. Klaasen, and J.L. Anderson, Acquisition and
Description of Mariner 10 Television Science Data at Mercury,
J. Geophys. Res., 80, 2357-2393, 1975.
- Dollfus, A. and C. Titulaer, Polarimetric Properties of the Lunar
Surface and Its Interpretation, 3, Volcanic Samples in Several
Wavelengths, Astron. Astrophys., 12, 199-209, 1971.
- Dollfus, A. and M. Auriere, Optical Polarimetry of the Planet Mercury,
Icarus, 23, 456-482, 1974.
- Dzurisin, D., Scarps, Ridges, Troughs, and Other Lineaments on Mercury,
Ph.D. Thesis (Part 1), Division of Geological and Planetary
Sciences, California Institute of Technology, Pasadena, California,
1976.
- Gehrels, T., T. Coffeen, and D. Owens, Wavelength Dependence of Polari-
zation. III. The Lunar Surface, Astron. J., 69, 826-852, 1964.
- Hapke, B., An Improved Theoretical Lunar Photometric Function, Astron.
J., 71, 333-339, 1966.
- Hapke, B., G.E. Danielson, Jr., K.P. Klaasen, and L. Wilson, Photometric
Observations of Mercury from Mariner 10, J. Geophys. Res., 80,
2431-2443, 1975.
- Hapke, B., Photometry of Venus from Mariner 10, submitted to J.A.S.,
1976a.

- Hapke, B., Composition and Microrelief of the Mercury Regolith, Paper presented at Conference on Comparisons of Mercury and the Moon, November 15-17, Lunar Science Institute, Houston, Texas, 1976b.
- Harris, D., Photometry and Colorimetry of Planets and Satellites. In Planets and Satellites, G. Kuiper and B. Middlehurst, eds., Univ. of Chicago Press, Chicago, 272-342, 1961.
- Irvine, W., T. Simon, D. Menzel, C. Pikoos, and A. Young, Multicolor Photoelectric Photometry of the Brighter Planets, III. Observations from Boyden Observatory, Astron. J., 73, 807-828, 1968.
- Lane, A.P. and W.M. Irvine, Monochromatic Phase Curves and Albedos for the Lunar Disk, Astron. J., 78, 267-277, 1973.
- Malin, M.C. and D. Dzurisin, Landform Degradation on Mercury, the Moon, and Mars, J. Geophys. Res., 1976 (in press).
- McCord, T.B. and J.B. Adams, Mercury: Surface Composition from the Reflection Spectrum, Science, 178, 745-747, 1972.
- Murray, B.C., M. Belton, G.E. Danielson, M.E. Davies, D.E. Gault, B. Hapke, B. O'Leary, R.G. Strom, V. Suomi, and N.J. Trask, Mercury's Surface: Preliminary Description and Interpretation from Mariner 10 Pictures, Science, 185, 169-179, 1974.
- Murray, B.C., R.G. Strom, N.J. Trask, and D.E. Gault, Surface History of Mercury: Implications for Terrestrial Planets, J. Geophys. Res., 80, 2508-2514, 1975.
- Oberbeck, V.R., A Mechanism for the Production of Lunar Crater Rays, The Moon, 2, 263-278, 1971.

- Oberbeck, V.R., W.L. Quaide, R.E. Arvidson, and H.R. Aggarwal,
Comparative Studies of Lunar, Martian, and Mercurian Craters and
Plains, NASA Technical Memorandum TM-X-62, 501, 1975.
- Pohn, H.A., H.W. Radin, and R.L. Wildey, The Moon's Photometric Function
Near Zero Phase Angle from Apollo 8 Photography, Astrophys. J.,
157, L193-L195, 1969.
- Pohn, H. and R. Wildey, A Photoelectric-Photographic Study of the Normal
Albedo of the Moon, U.S. Geol. Surv. Prof. Paper 599-E, 1970.
- Soha, J.M., D.J. Lynn, J.J. Lorre, J.A. Mosher, N.N. Thayer, D.A. Elliott,
W.D. Benton, R.E. Dewar, IPL Processing of the Mariner 10 Images
of Mercury, J. Geophys. Res., 80, 2394-2414, 1975.
- Strom, R.G., N.J. Trask, and J.E. Guest, Tectonism and Volcanism on
Mercury, J. Geophys. Res., 80, 2478-2507, 1975.
- Trask, N.J. and J.E. Guest, Preliminary Geologic Terrain Map of Mercury,
J. Geophys. Res., 80, 2461-2477, 1975.
- Van Diggelen, J., The Radiance of Lunar Objects Near Opposition,
Planetary Space Sci., 13, 271-279, 1965.
- Wilhelms, D.E., Mercurian Volcanism Questioned, Icarus, 28, 551-558,
1976.
- Young, A., Television Photometry: The Mariner 9 Experience, Icarus,
21, 262-282, 1974.

TABLE 1

COMPARISON OF MARINER 10 AND EARTH-BASED PHOTOMETRY

(After Hapke, 1976)

Object	Mariner 10 Value	Earth-Based Value
Moon - Normal Albedo	0.11	0.115 (Harris, 1961)
Jupiter - Normal Albedo		0.125 (Dollfus and Titulaer, 1971)
	0.44	0.45 (Harris, 1961)
Venus - Radiance of Sub-Solar Point		0.51 (Irvine, <i>et al.</i> , 1968)
Orange image	308	
Blue image	302	
UV image - Bright region	339	
UV image - Dark region	<u>302</u>	
Average	313	310 (Calculated from Irvine, <i>et al.</i> , 1968)

TABLE 2

LOCAL NORMAL ALBEDOS

(See Figure 1 for Index)

Heavily Cratered Terrain

Point	Latitude	Longitude	Normal Albedo (554 nm)	Hapke et al. (1975) Result
5	20°N	21°W	.16 ± .05	.16 ± .08
7	0°	22°W	.17 ± .04	-

Intercrater Plains

Point	Latitude	Longitude	Normal Albedo (554 nm)	Hapke et al. (1975) Result
6	27°N	26°W	.18 ± .02	-
8	6°N	20°W	.17 ± .03	-
11	56°S	40°W	.18 ± .02	.17 ± .03
12	57°S	37°W	.18 ± .02	.17 ± .04
13	61°S	41°W	.13 ± .01	-
14	66°S	52°W	.16 ± .01	-
29	11°N	117°W	.18 ± .01	-
30	12°S	142°W	.15 ± .01	.13 ± .01
31	32°N	102°W	.14 ± .01	.14 ± .01
39	44°S	29°W	.17 ± .02	-
40	50°S	60°W	.17 ± .01	.17 ± .01
43	28°N	24°W	.17 ± .02	.17 ± .03
47	19°S	52°W	.17 ± .02	-

Average .17

Caloris Plains

Point	Latitude	Longitude	Normal Albedo (554 nm)	Hapke et al. (1975) Result
15	33°N	179°W	.18 ± .03	.14 ± .04
16	53°N	167°W	.16 ± .02	.14 ± .02
18	5°N	175°W	.13 ± .02	.13 ± .01
19	40°N	178°W	.18 ± .04	-
23	10°S	160°W	.12 ± .01	-
28	54°N	151°W	.14 ± .01	.13 ± .01
32	37°N	109°W	.16 ± .01	-

TABLE 2
(Continued)

Point	Latitude	Longitude	Normal Albedo (554 nm)	Hapke <i>et al.</i> (1975) Result
-------	----------	-----------	---------------------------	--------------------------------------

34	31° N	130° W	.15 ± .01	.14 ± .01
35	27° N	162° W	.13 ± .01	.11 ± .01
36	39° N	166° W	.16 ± .02	-
37	37° N	168° W	.15 ± .02	-
44	0°	171° W	.16 ± .02	.14 ± .01
45	3° S	156° W	.13 ± .02	-

Average .15

Dark Smooth Plains

Point	Latitude	Longitude	Normal Albedo (554 nm)	Hapke <i>et al.</i> (1975) Result
-------	----------	-----------	---------------------------	--------------------------------------

17	45° N	155° W	.13 ± .01	-
22	14° S	159° W	.16 ± .01	.13 ± .01

Light Smooth Plains

Point	Latitude	Longitude	Normal Albedo (554 nm)	Hapke <i>et al.</i> (1975) Result
-------	----------	-----------	---------------------------	--------------------------------------

3	30° S	28° W	.24 ± .03	.21 ± .01
4	29° S	35° W	.22 ± .01	.20 ± .02
41	17° S	51° W	.23 ± .01	-

Average .23

Rays

Point	Latitude	Longitude	Normal Albedo (554 nm)	Hapke <i>et al.</i> (1975) Result
-------	----------	-----------	---------------------------	--------------------------------------

2	21° S	32° W	.22 ± .03	-
9	2° N	28° W	.22 ± .03	.20 ± .04
10	12° S	36° W	.26 ± .02	.27 ± .03
24	2° N	120° W	.27 ± .02	.26 ± .02

TABLE 2
(Continued)

Point	Latitude	Longitude	Normal Albedo (554 nm)	Hapke et al. (1975) Result
25	38°N	123°W	.23 ± .01	.24 ± .01
26	39°N	127°W	.20 ± .01	.21 ± .01
27	40°N	115°W	.25 ± .01	-
33	35°N	133°W	.22 ± .01	-
38	37°S	54°W	.20 ± .01	.19 ± .01
Average			.23	

Bright Patches

Point	Latitude	Longitude	Normal Albedo (554 nm)	Hapke et al. (1975) Result
1	11°S	31°W	.48 ± .02	.45 ± .04
20	2°S	138°W	.44 ± .03	.39 ± .04
21	6°N	144°W	.43 ± .03	.40 ± .03
42	11°S	56°W	.48 ± .02	.45 ± .05
46	12°N	141°W	.37 ± .02	-
Average			.44	

TABLE 3

FRAMES COMPRISING FIGURES 2-5

Incoming		Outgoing	
FDS	Resolution (2 pixels)	FDS	Resolution
27085	6.5 km		
27087	6.2	498	4.0 km
27090	4.6	500	3.4
27091	4.2	501	4.0
27093	3.8	503	4.2
27094	5.6	504	5.0
27095	4.0	505	8.0
27096	3.6	506	4.2
27097	4.4	507	4.2
27208	3.4	508	5.4
27212	3.2	509	4.2
27221	4.5	510	4.4

TABLE 4

GEOMETRIC ALBEDO OF MERCURY AND THE MOON

Geometric Albedo (554 nm)		Source
Mercury	.10	Harris (1961)
	.125	Dollfus and Auriere (1974)
Moon	.115	Harris (1961)
	.12	Pohn and Wildey (1970)
	.125	Dollfus and Titulaer (1971)
	.113	Lane and Irvine (1973)

REPRODUCIBILITY OF
ORIGINAL PAGE IS POOR

TABLE 5
MERCURIAN BRIGHT PATCHES
Lighting and Viewing Conditions

ID (Figures 4,5)	Sun Elevation Angle	Phase Angle	Viewing Angle
4A	52°	102°	70°
4D	25°	103°	41°
4F	45°	71°	45°
50	39°	77°	35°
5Q	41°	77°	32°
5R	42°	77°	42°
5S	40°	77°	38°

FIGURE CAPTIONS

Part 2

Figure 1 - Photomosaics of Mariner 10 Incoming (a) and Outgoing Quadrants (b) of Mercury, with numbered points marking locations for which local normal albedos are presented in Table 2.

Mean resolution of photographs comprising mosaics = 2 km.

Figure 2 - Radiometrically decalibrated and contrast enhanced mosaics of Mariner 10 Incoming (a) and Outgoing Quadrants (b).

Appearance is dominated by terminator-to-limb brightness variations owing to changing illumination conditions. Line in (a) marks position of limb.

Figure 3 - Phase-normalized versions of Incoming (a) and Outgoing Quadrants (b). Picture data numbers have been individually corrected to those expected under normal viewing and lighting conditions, thereby eliminating terminator-to-limb brightness variations. It was assumed for this calculation that the mercurian surface everywhere obeys the average lunar photometric function derived by Hapke (1966).

Figure 4 - Relative photometric map, Incoming Quadrant. If Mercury obeys the average lunar photometric function everywhere, each gray level step corresponds to a change in normal albedo of .065. Thus, black (shadows) indicates $A = 0.0 - .065$, and white indicates $A > .325$. Hapke (1976b) has shown that apparent polar darkening is an artifact produced by crater shadowing effects. There is at present no evidence

Figure 4 - for a latitudinal variation of mean normal albedo on Mercury. Letters A-M are referenced in the text.

Figure 5 - Relative photometric map, Outgoing Quadrant. Apparent brightening near the terminator (left) is an artifact produced by the computer algorithm employed to generate photometric maps from digital images. If Mercury obeys the average lunar photometric function (Hapke, 1966), gray level steps correspond to normal albedo changes of .065. Letters N-S are referenced in the text. See Table 3 for list of Mariner 10 frames comprising Figures 2-5.

Figure 6 - Generalized terrain map of Mercury, after Trask and Guest (1975). Caloris plains as outlined here include smooth Caloris plains, hummocky plains, and lineated terrain units as mapped by those authors. The hilly and lineated terrain unit is included here as intercrater plains. Dashed lines indicate discriminability limit in Mariner 10 photographs owing to unfavorable lighting and viewing conditions.

Figure 7 - Arcuate and lobate escarpments on Mercury.

(a) Unnamed arcuate scarp near 57° S, 175° W which transects at least four craters in the upper left corner of FDS 166842.

(b) Arcuate Discovery Scarp (54° S, 38° W) similarly crosses intercrater plains and two large craters without otherwise modifying the morphology of preexisting surfaces or

Figure 7 (b) - landforms. Mosaic of Mariner 10 frames 27386, 27393,
(cont.) 27398, and 27399.

(c) Vostock Scarp transects two large craters in the upper left and foreshortens the rim of one by roughly 10 km.

Mariner 10 FDS 27380.

(d) Mosaic of frames 166649 and 166650 showing large, planimetrically lobate escarpment near 24° S, 53° W. No significant photometric variations were observed across these or similar scarps elsewhere on Mercury inferred by Dzurisin (1976) from morphologic considerations and trans-sectional relationships to be tectonic in origin.

Figure 8 - Mariner 10 frame 166649 reveals apparent photometric contrast between visually obscured and unobscured parts (boundaries marked by arrows) of a 200 km double ring basin and an 80 km degraded crater. Obscured rim segments are seen in stereo images to be topographically continuous with their unobscured extensions (Dzurisin, 1976). Local albedo measurements shown are for points 41 and 47 (Figure 1a, Table 2). Seemingly lower albedo of visually obscured areas may in part be an artifact caused by a high density of small, partially shadowed pits.

Figure 9 - (a) Planimetrically lobate escarpment (arrows) which transects and obscures arcuate Resolution Scarp and two large craters (top, center) near 63° S, 53° W. Mariner 10 frames 166679 and 166686.

(b) Photometric map of the region shown in 9a, with arrows marking trace of lobate escarpment. Computer processing of this frame (FDS 27208) was similar to that applied to images in Figures 4 and 5. Note that the scarp separates regional expanses of plains which differ in photometric character. Local albedo measurements are for points 13 and 14 in Figure 1a, Table 2.

Figure 10 - Bright and dark smooth plains. Densities of small superposed craters suggest that bright ($A = .23 \pm .01$, top) and dark ($A = .14 \pm .02$, bottom) mercurian intercrater plains are roughly the same age. Top left = FDS 166607, centered near 42° S, 55° W. The 200 km basin in the center is labeled L in Figure 4. Top right (FDS 27379, 30° S, 35° W) shows bright smooth plains in 85 km craters labeled I in Figure 4. Bottom left (FDS 166673) shows typical dark mercurian plains inside a 140 km crater at 60° S, 62° W. Bottom right = FDS 27392 (48° S, 19° W). Crater with dark smooth plains inside is 160 km in diameter. North is approximately toward top in each image.

Figure 11 - Mercurian bright patches.

- (a) Kuiper crater (Point 1, Figure 1a, Table 2). FDS 27362 and 27363.
- (b) Bright patch on the floor of a 40 km crater near 11° S, 56° W (point 42, FDS 166637).
- (c) Two bright patches (points 21 and 46) on floors of dark-haloed craters near 9° N, 142° W (FDS 214).
- (d) FDS 215, with several bright patches on crater floors near 2° S, 138° W (point 20, Figure 5, Table 2). Color ratio images of the areas shown in 11C and 11D are provided in Figure 12.

Figure 12 - Color ratio images of mercurian bright patches. Mariner 10

UV ($\lambda_{\text{eff}} = 355$ nm) and orange ($\lambda_{\text{eff}} = 575$ nm) frames have been registered and picture data numbers ratioed (UV/OR) to produce these representations of mercurian color variations. Relatively blue areas appear bright; relatively red areas appear dark. Some high frequency variations are artifacts produced by camera blemishes and slight image misregistration. Figure 12a shows bright Lermontov Crater (15.5° N, 48.5° W; arrow) labeled A in Figure 4. Note red crater floor with relatively blue patches which coincide with location of bright material. Small dark dot to left of Lermontov and similar examples elsewhere are artifacts produced by fiducial marks on camera face plate. Bright patches shown in Figure 11(C,D) are seen in Figure 12b

Figure 12 - (arrows) to be relatively blue areas situated on relatively red crater floors. Dark haloes of two northern craters are likewise redder than surrounding plains. Large dark (i.e., red) area near center of image corresponds to location of bright, fresh crater. Most other mercurian craters are distinctly bluer than their surroundings (Hapke et al., 1975). North is roughly toward top in both images. Lermontov Crater in Figure 12a is 160 km in diameter. Distance between two northernmost arrows in 12b is roughly 400 km. Top = FDS 26846(UV)/FDS 26847(OR). Bottom = FDS 742(UV)/FDS 741(OR).

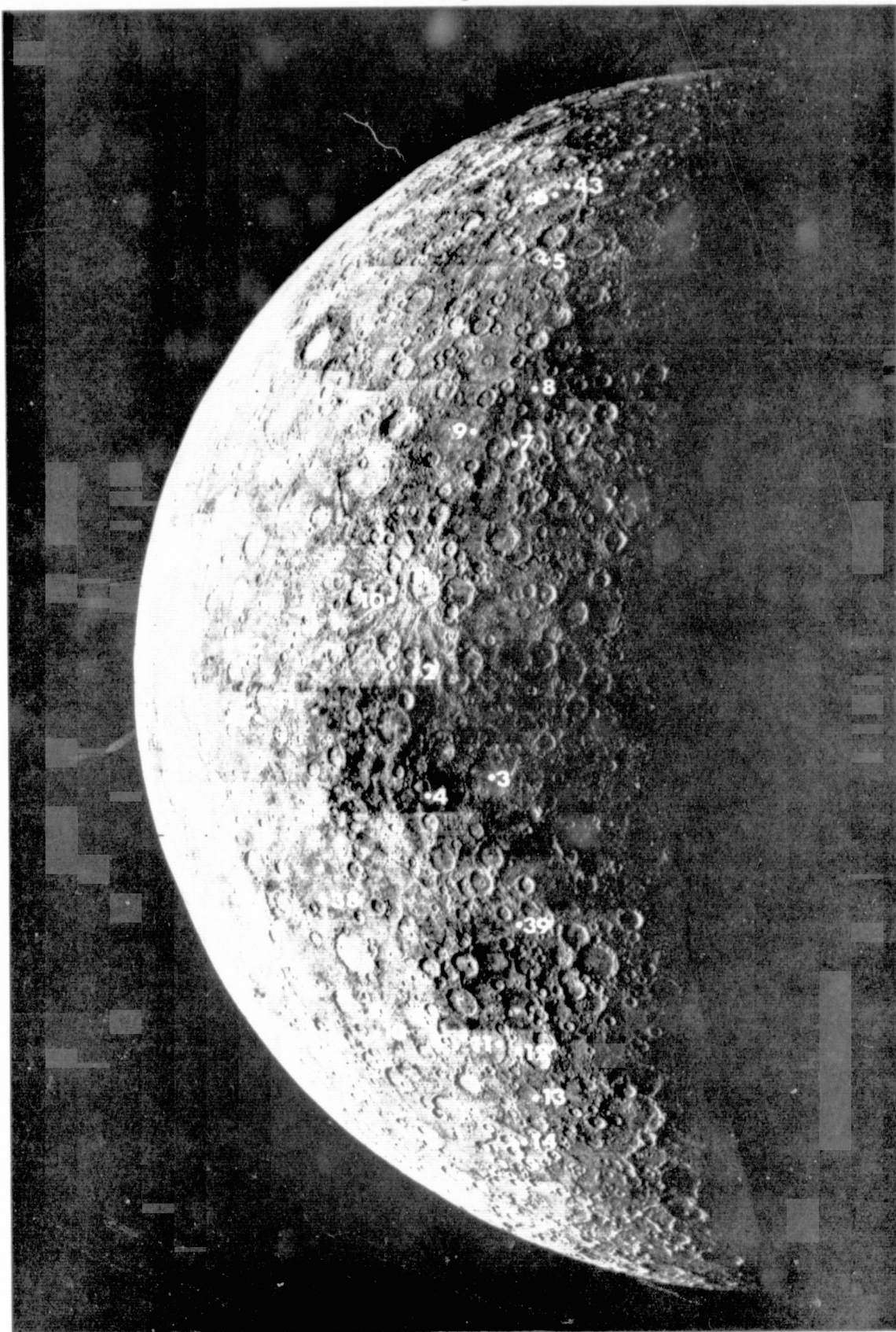


Figure 1a

164

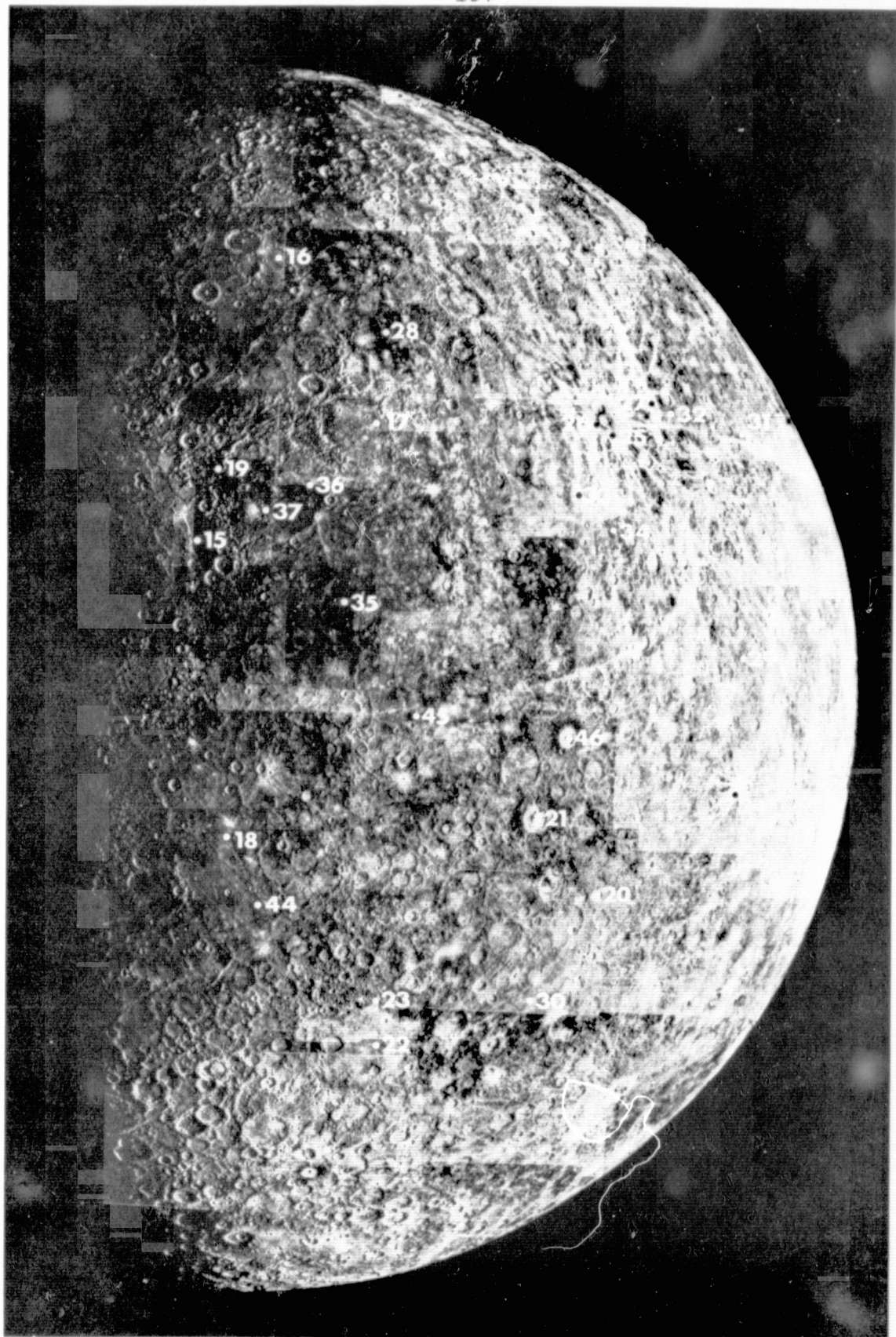


Figure 1b

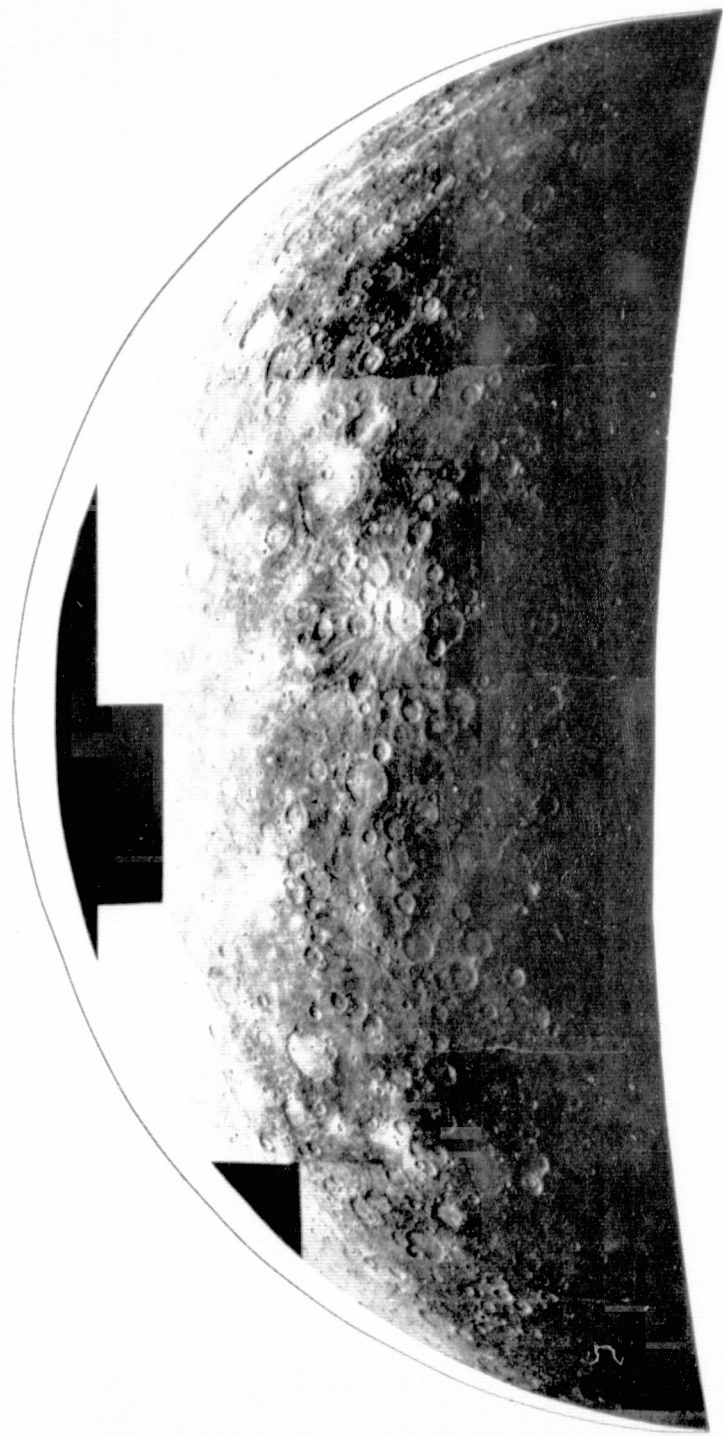


Figure 2a

REPRODUCIBILITY OF T
ORIGINAL PAGE IS POOR

166

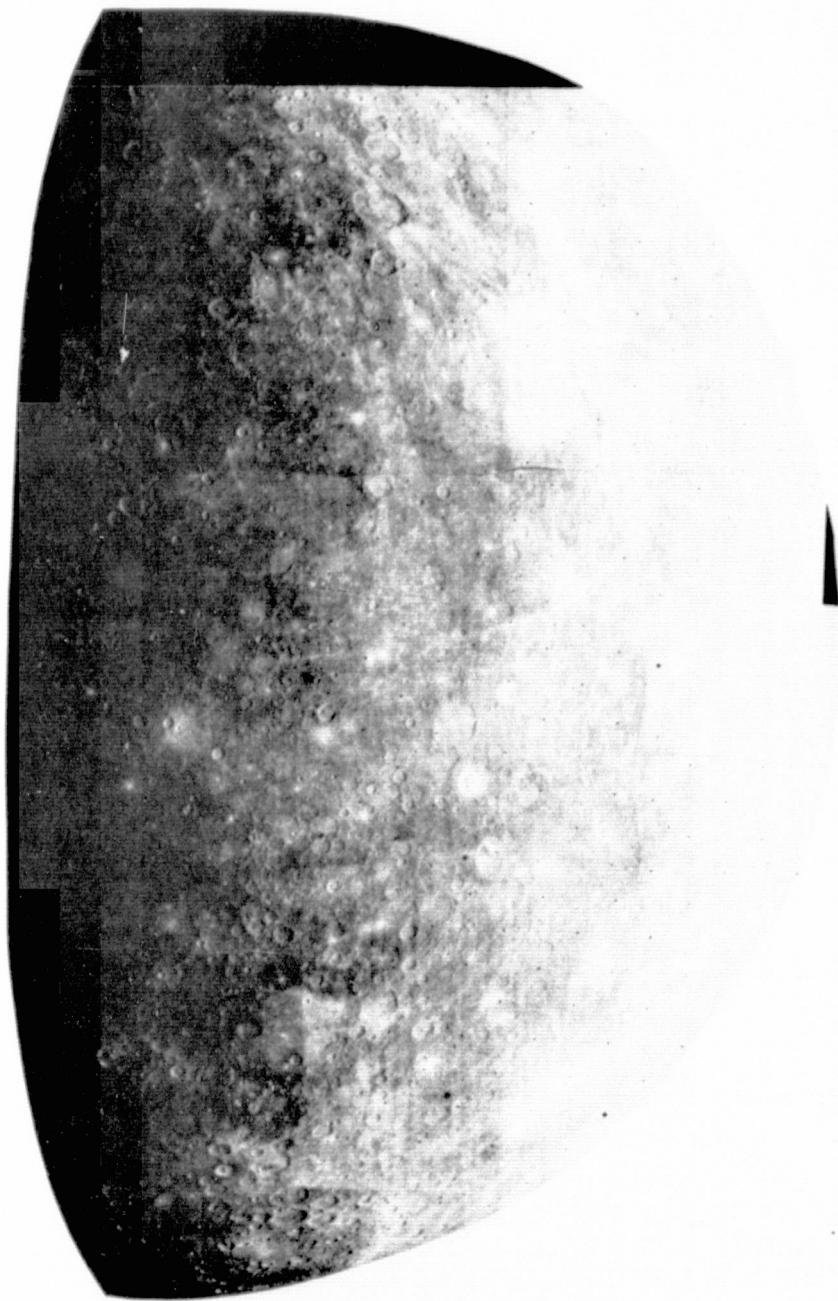


Figure 2b

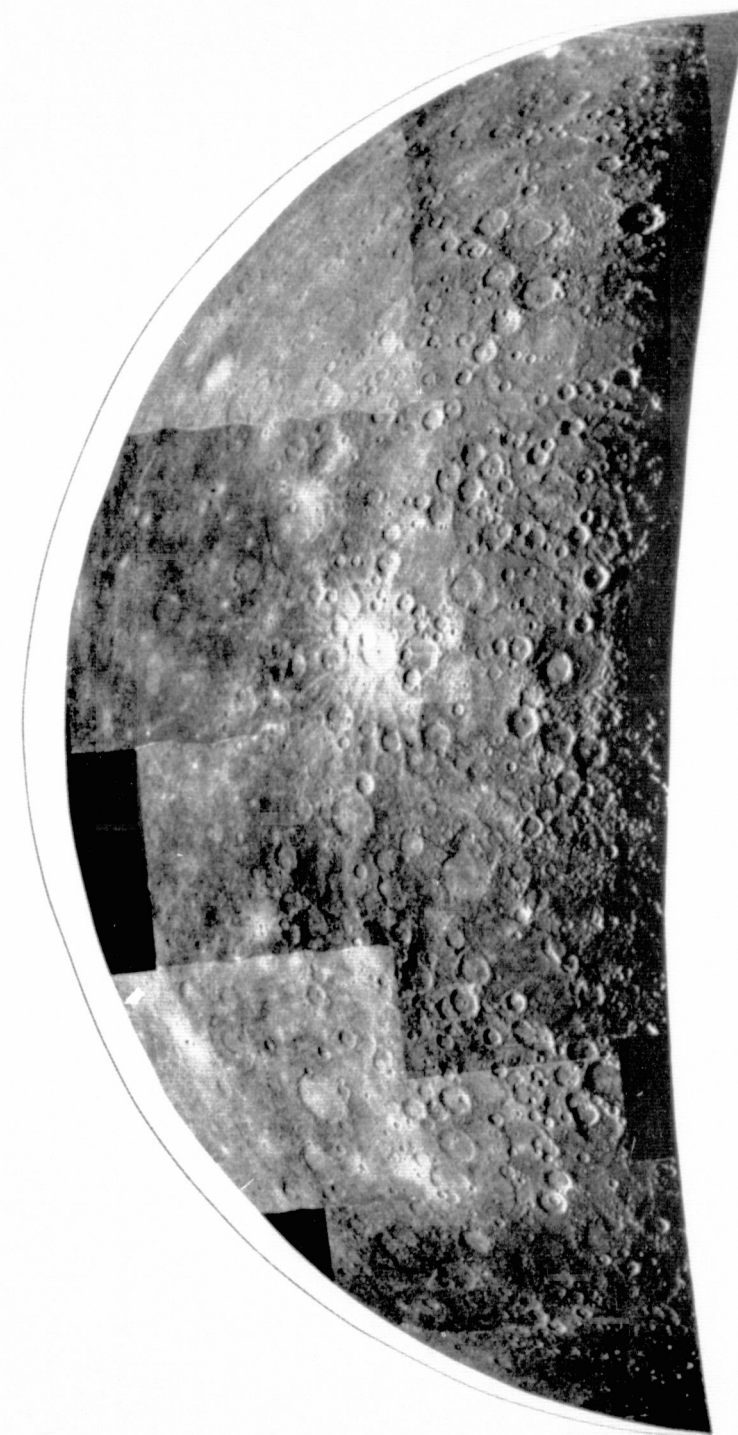


Figure 3a

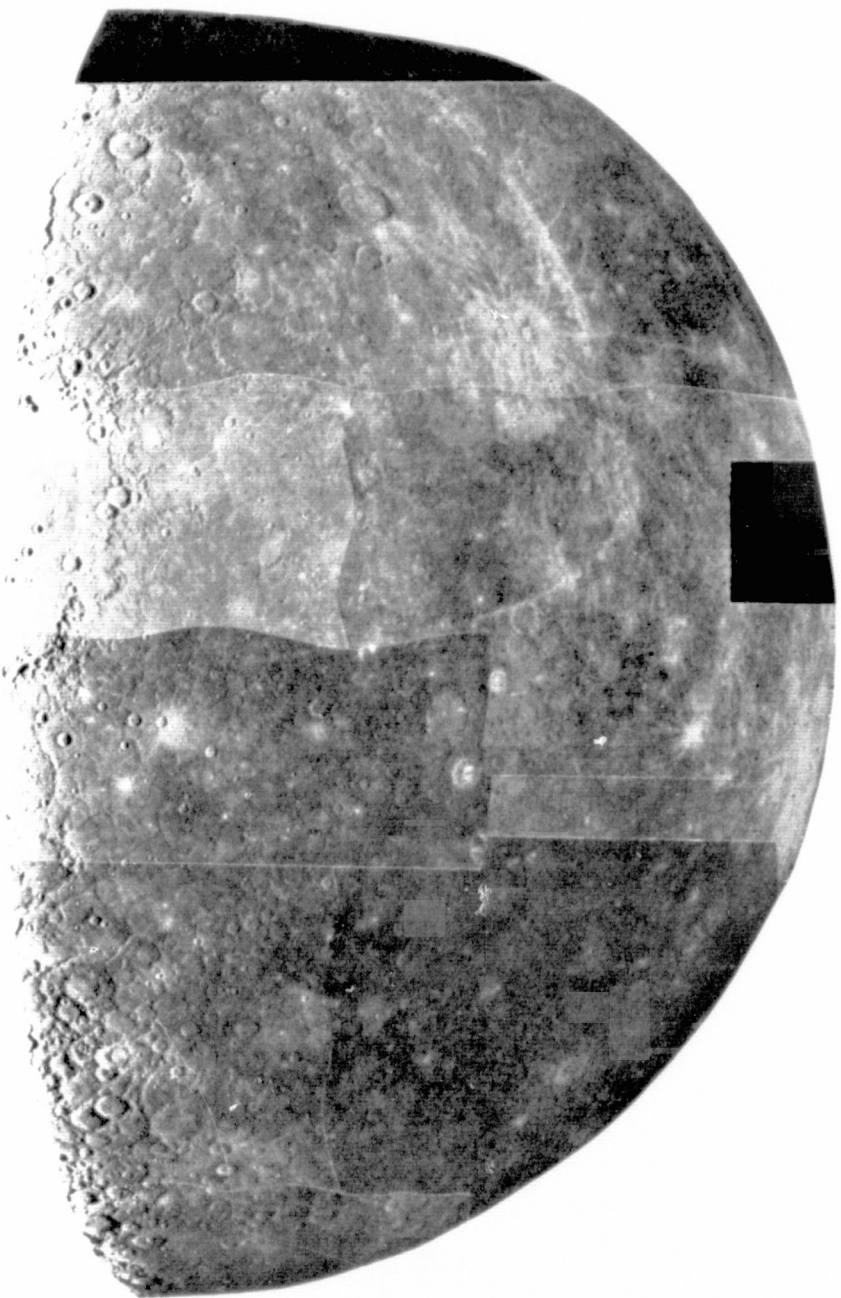
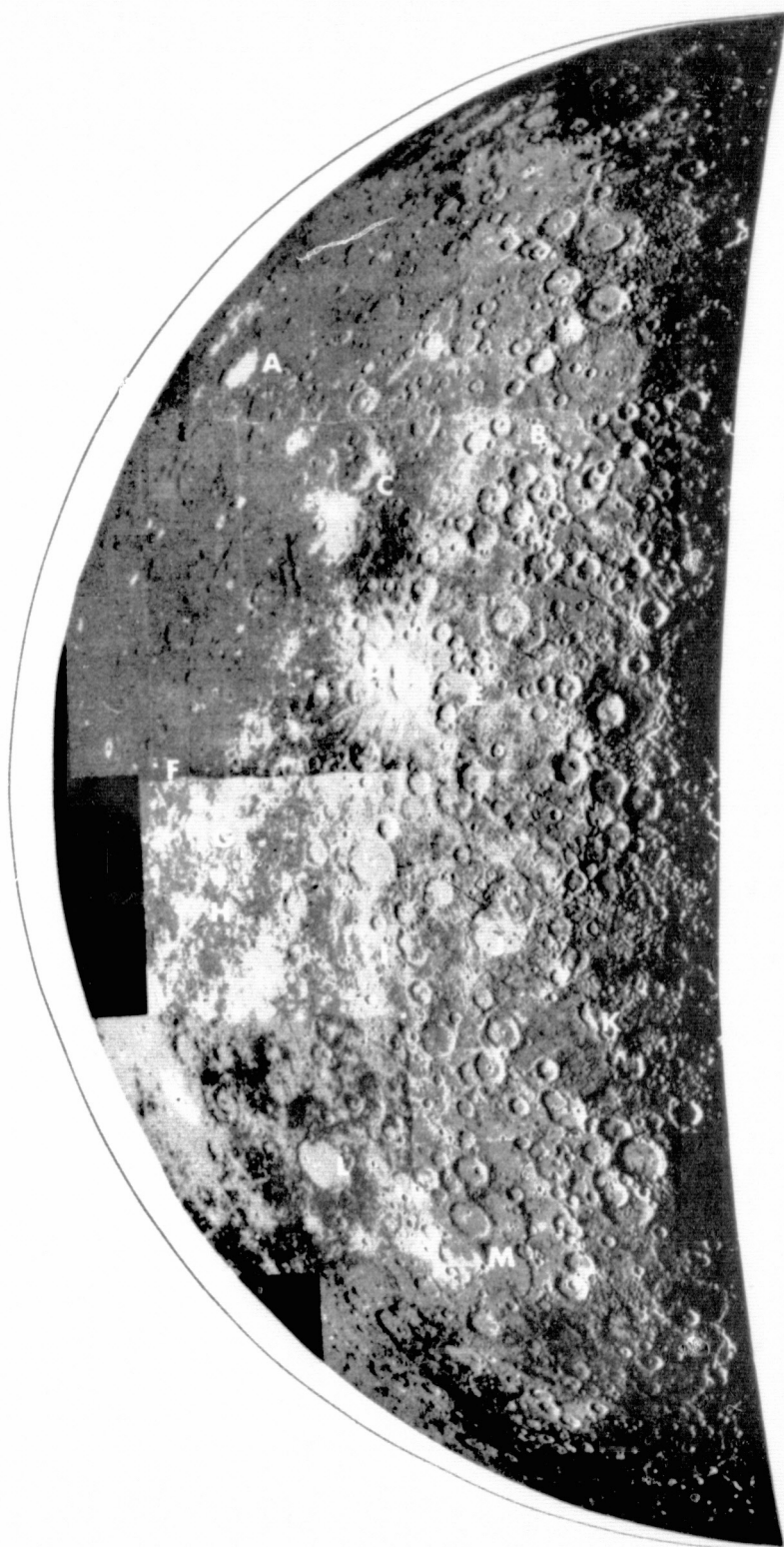


Figure 3b



REPRODUCIBILITY OF THE
ORIGINAL PAGE IS POOR

Figure 4

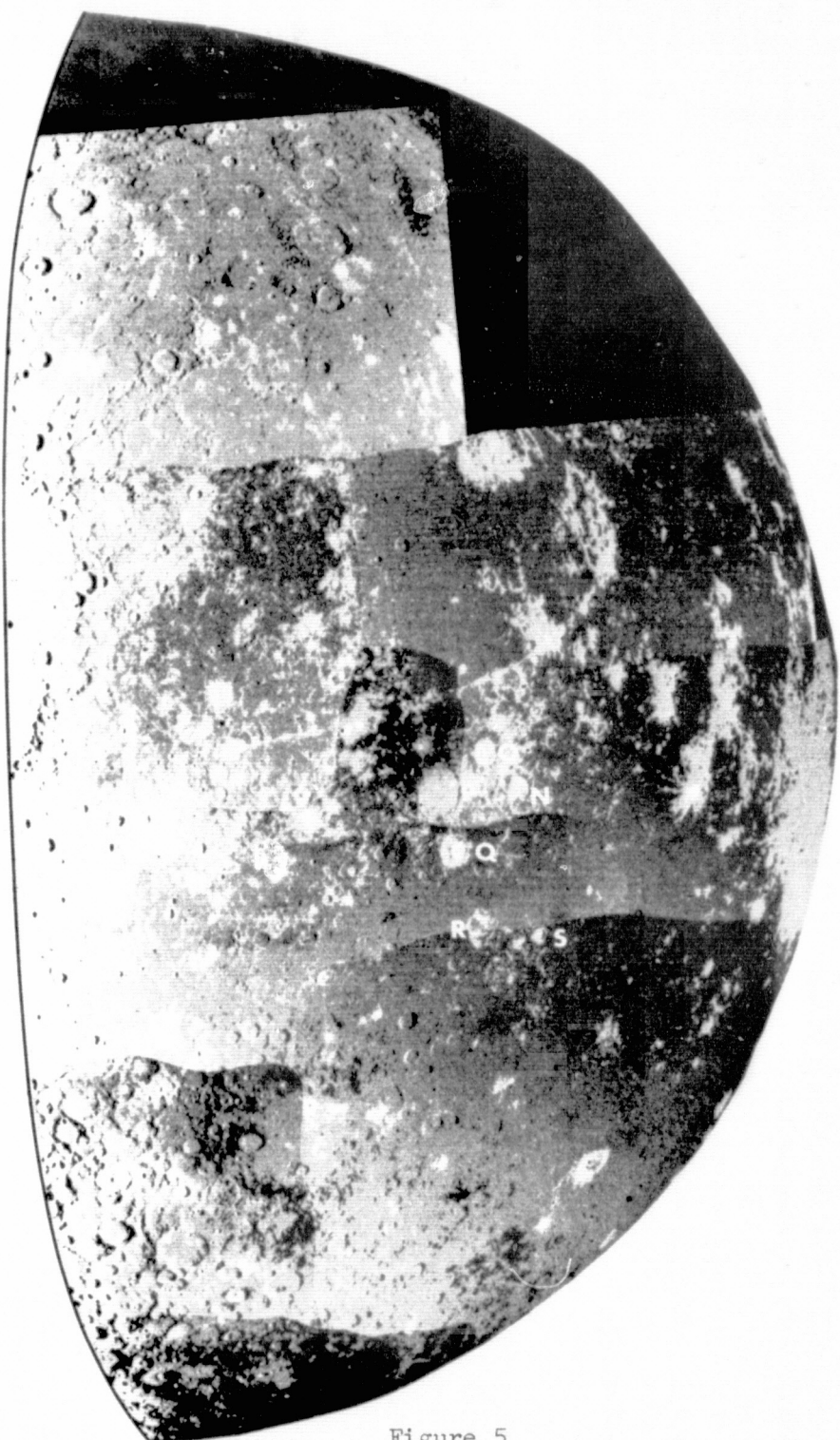
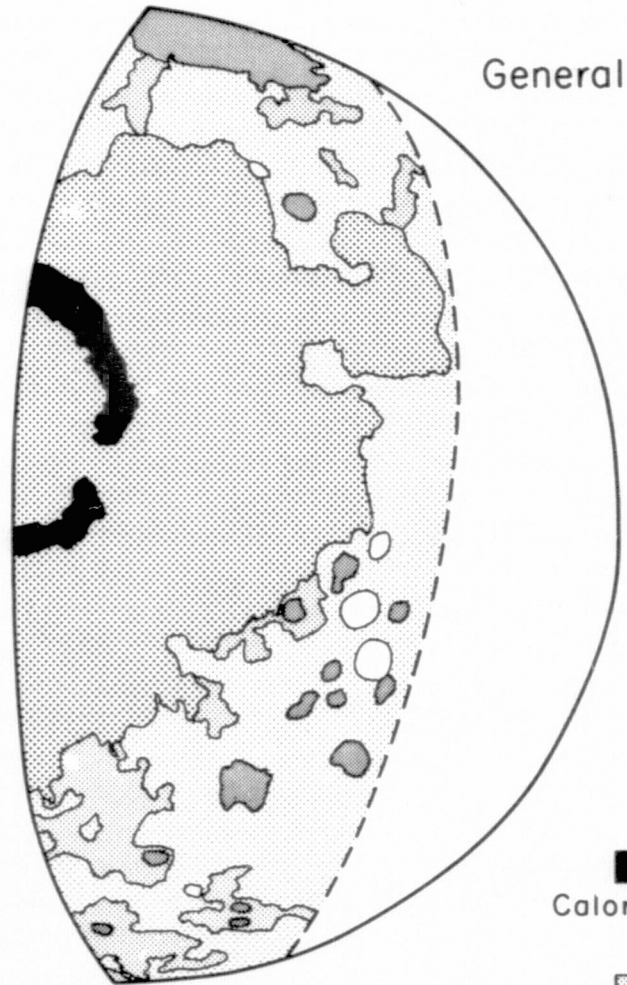
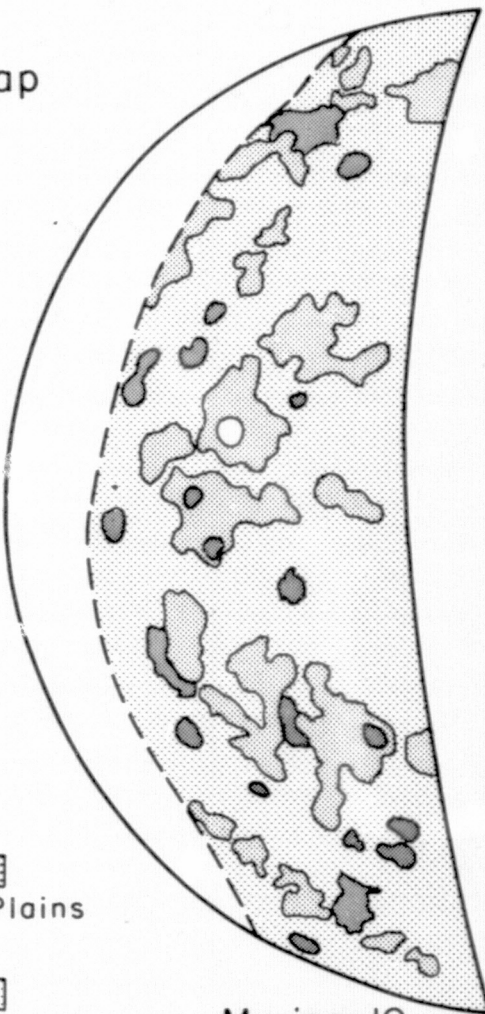
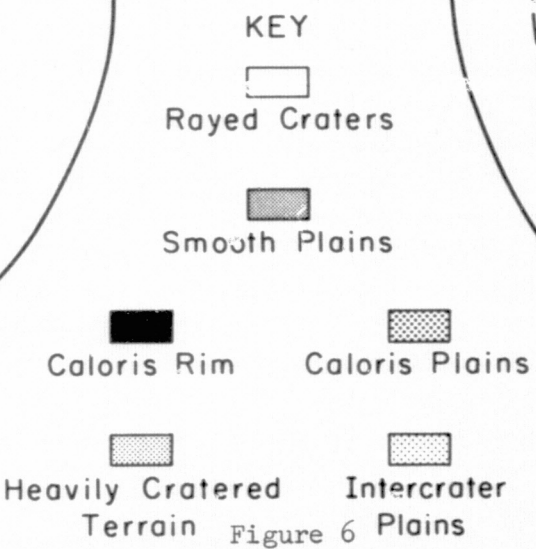


Figure 5

MERCURY
Generalized Terrain Map



Mariner 10
Outgoing Quadrant



Mariner 10
Incoming Quadrant

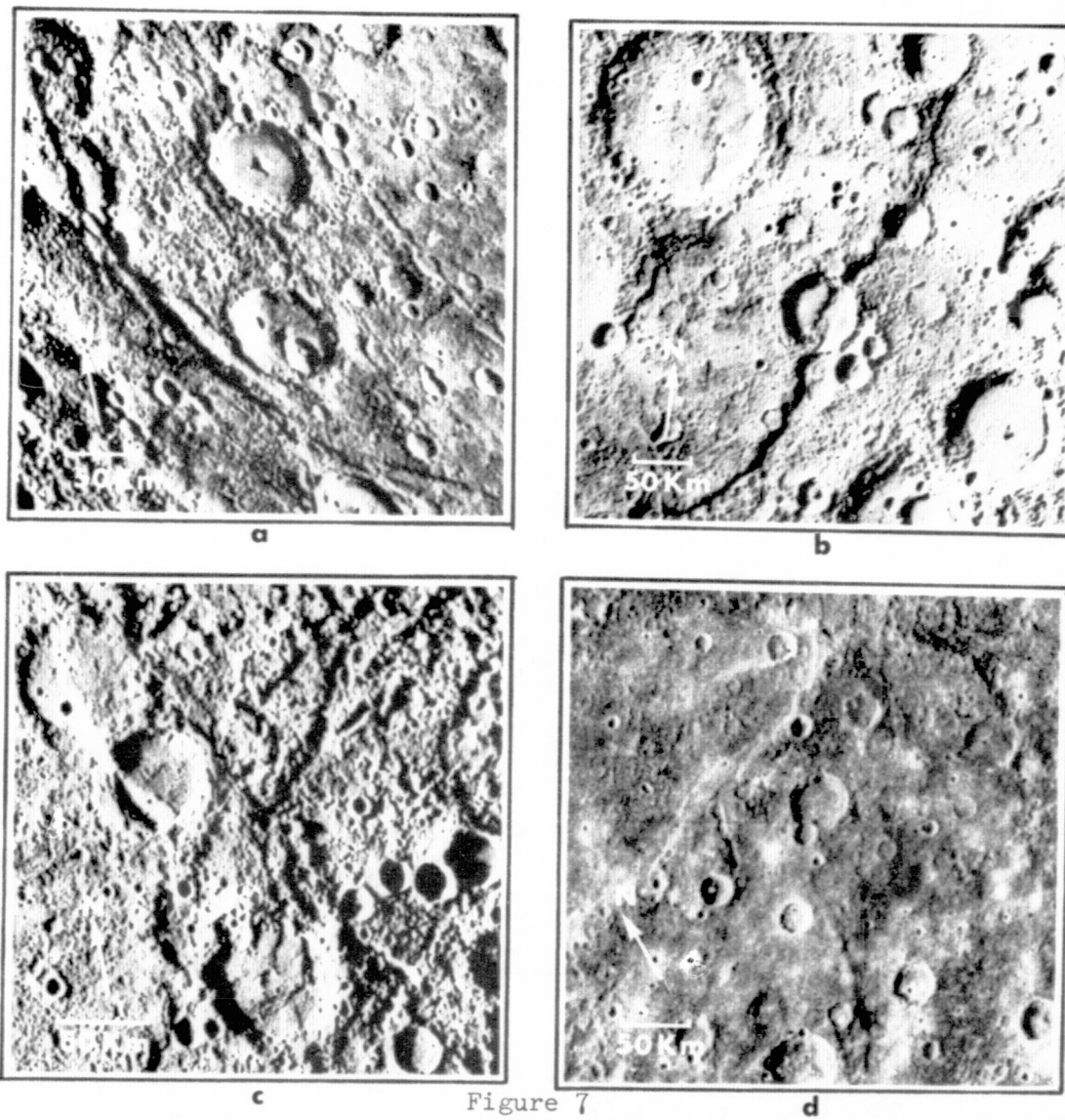


Figure 7

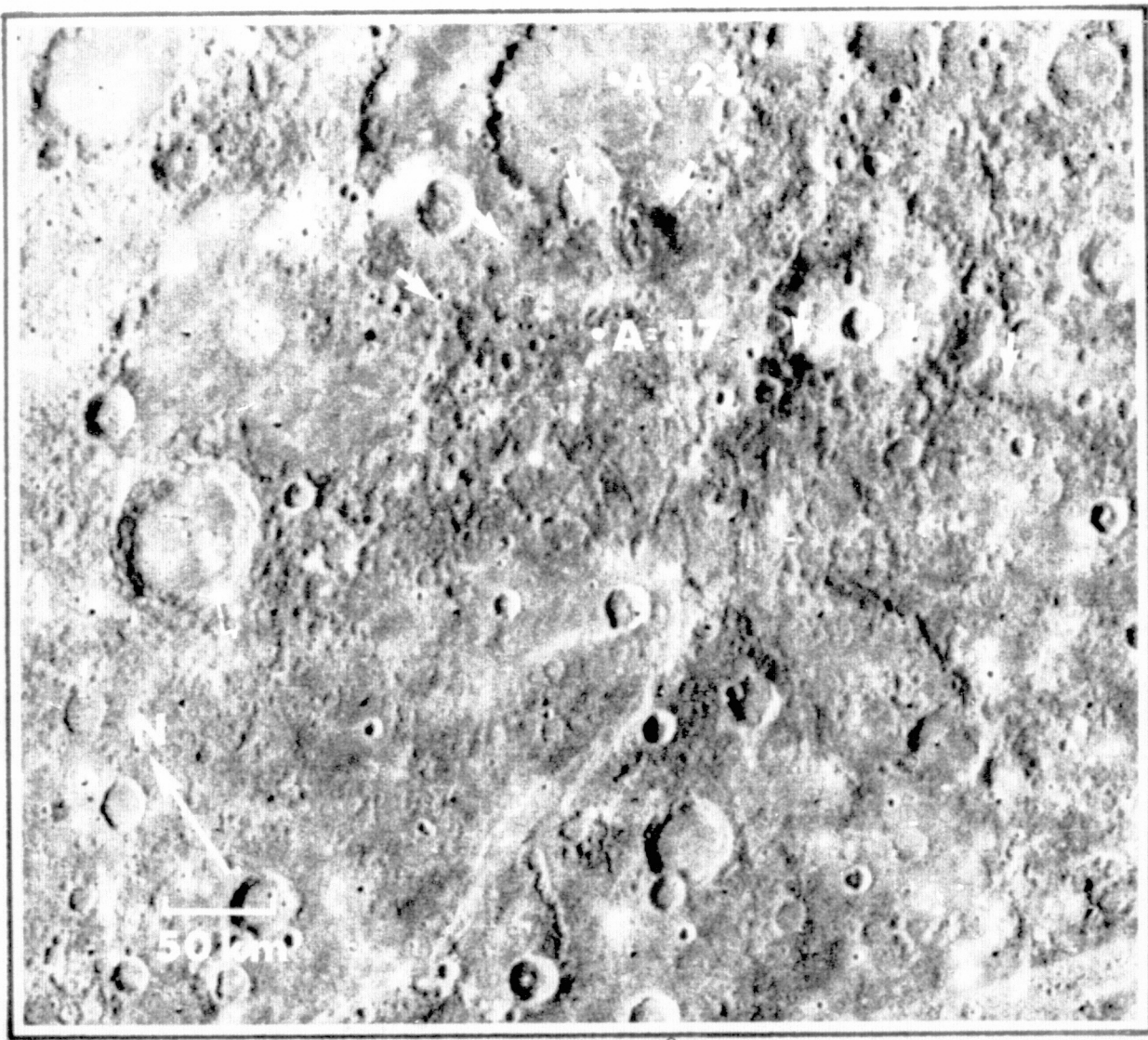


Figure 8

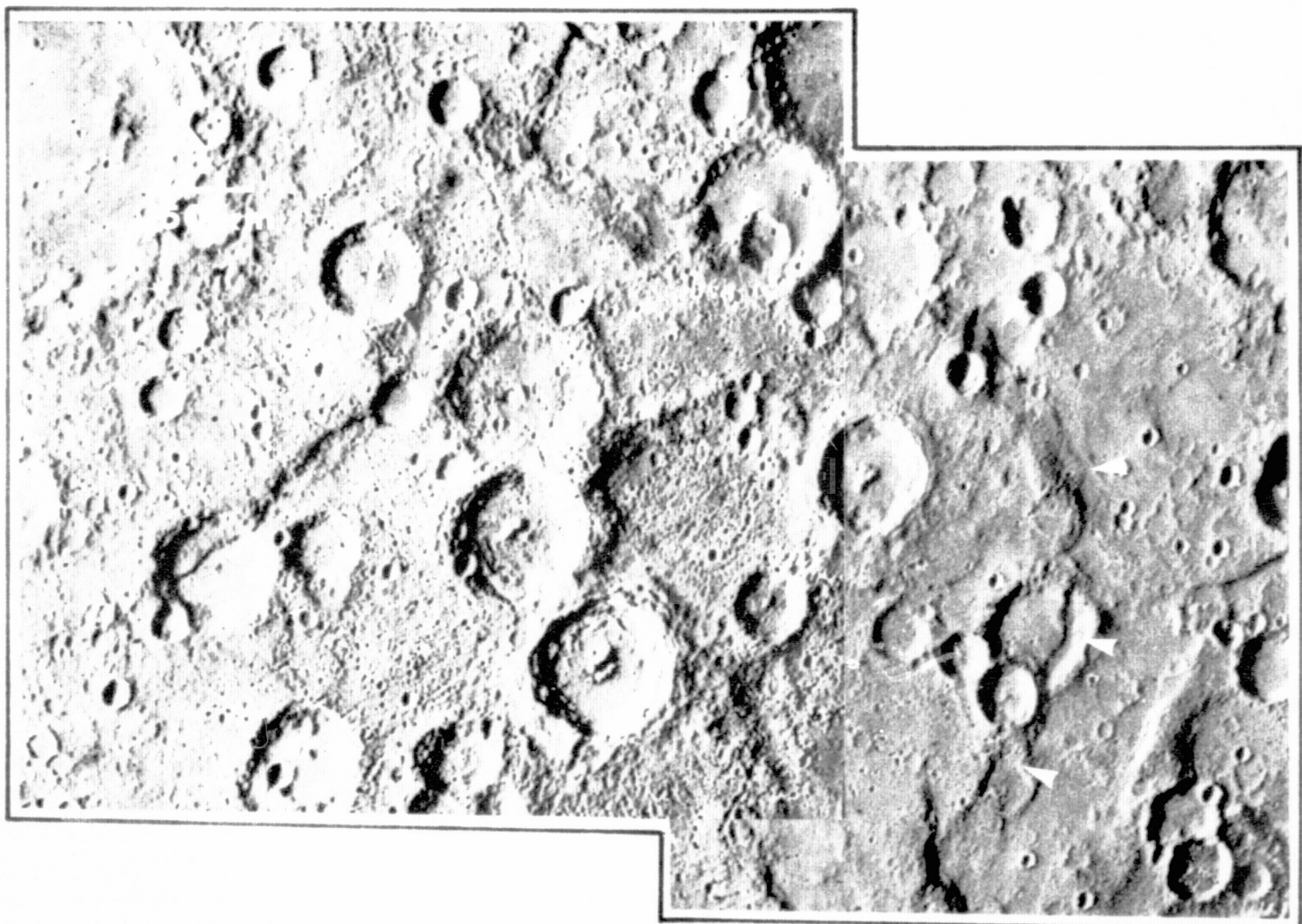


Figure 9

a

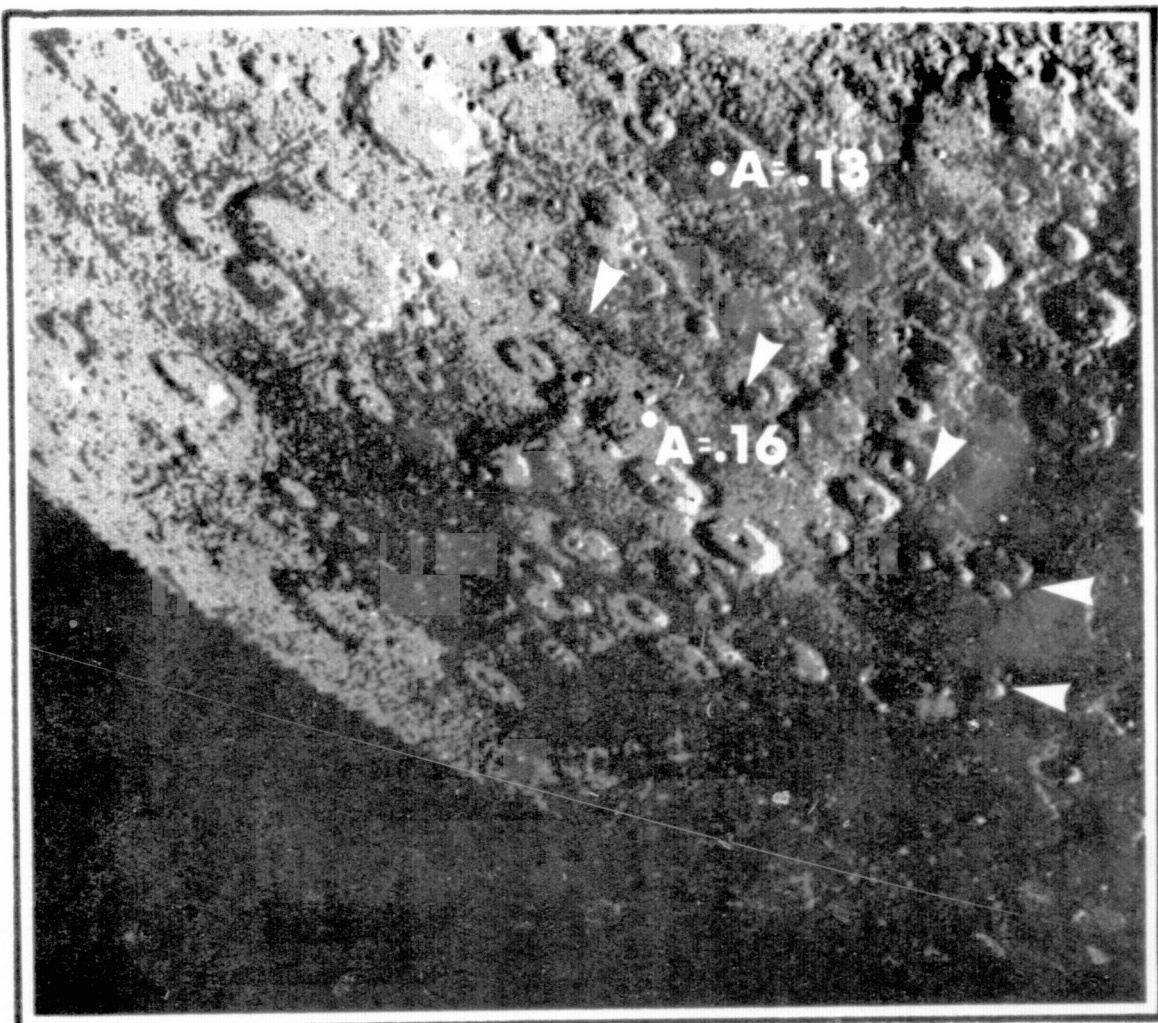


Figure 9

b

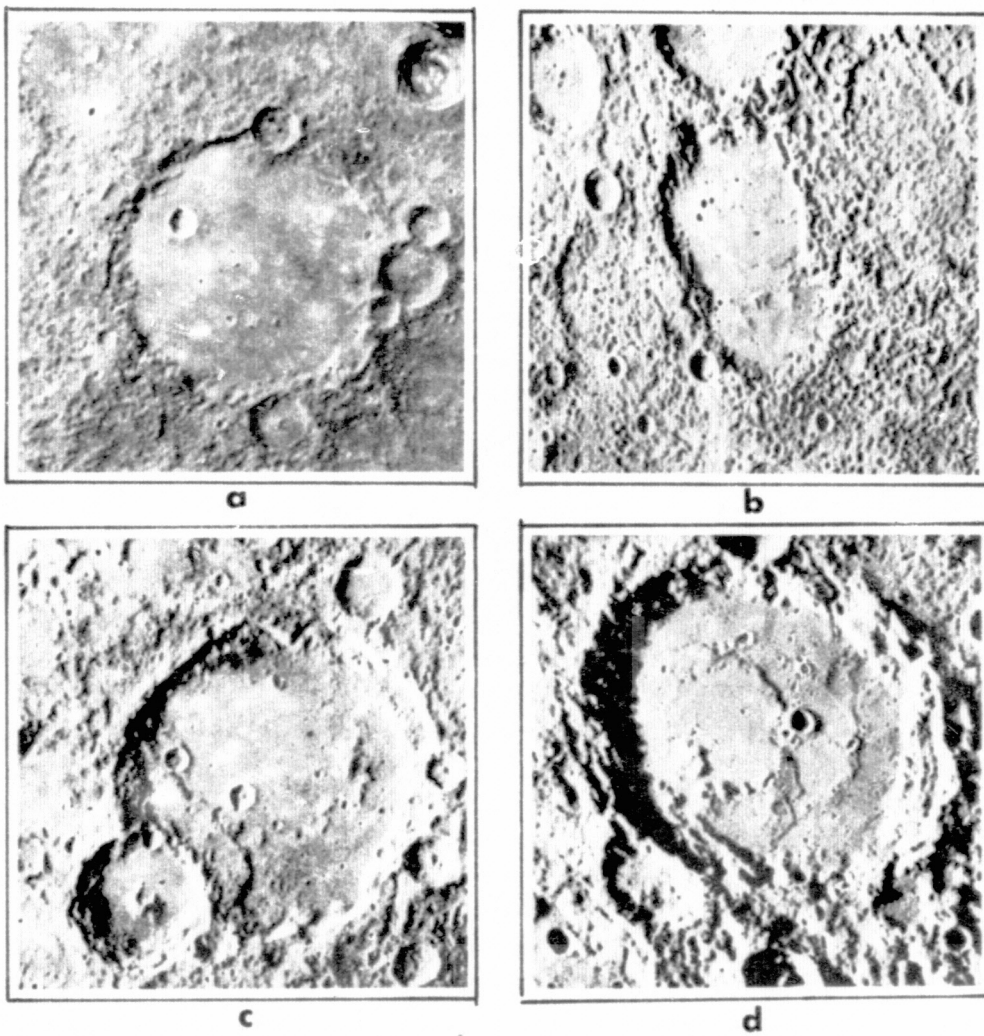
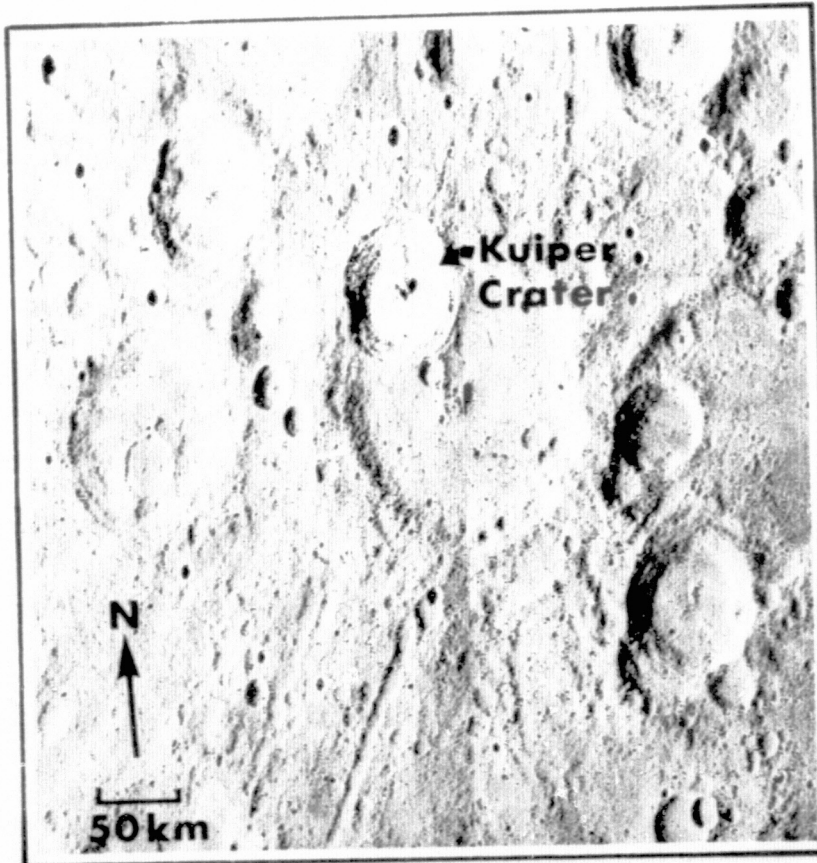
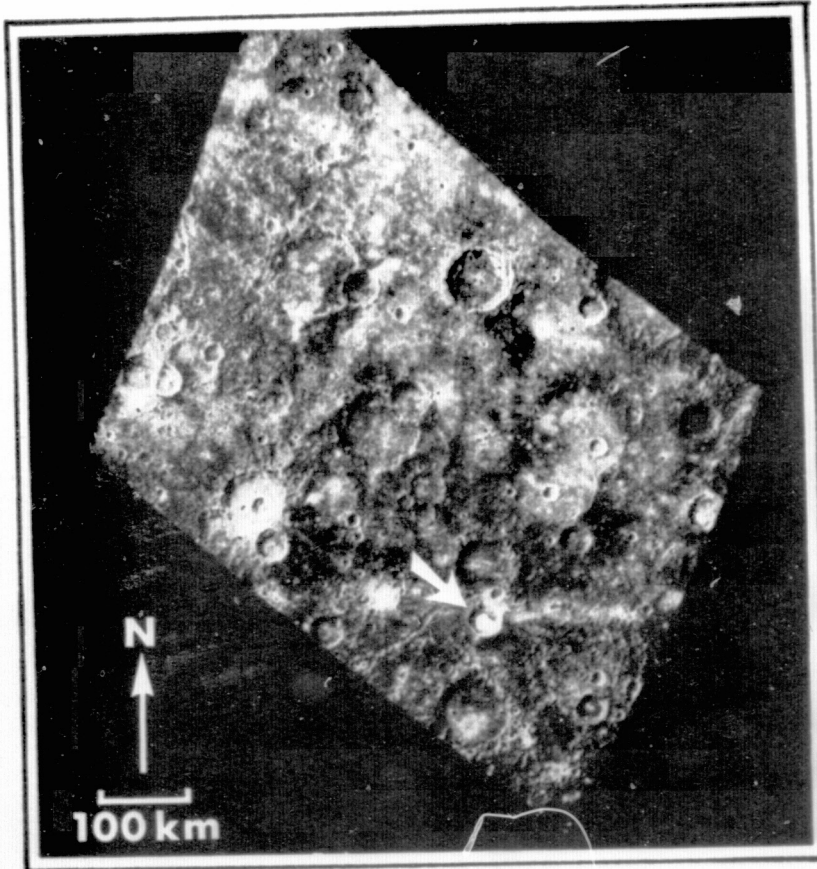


Figure 10

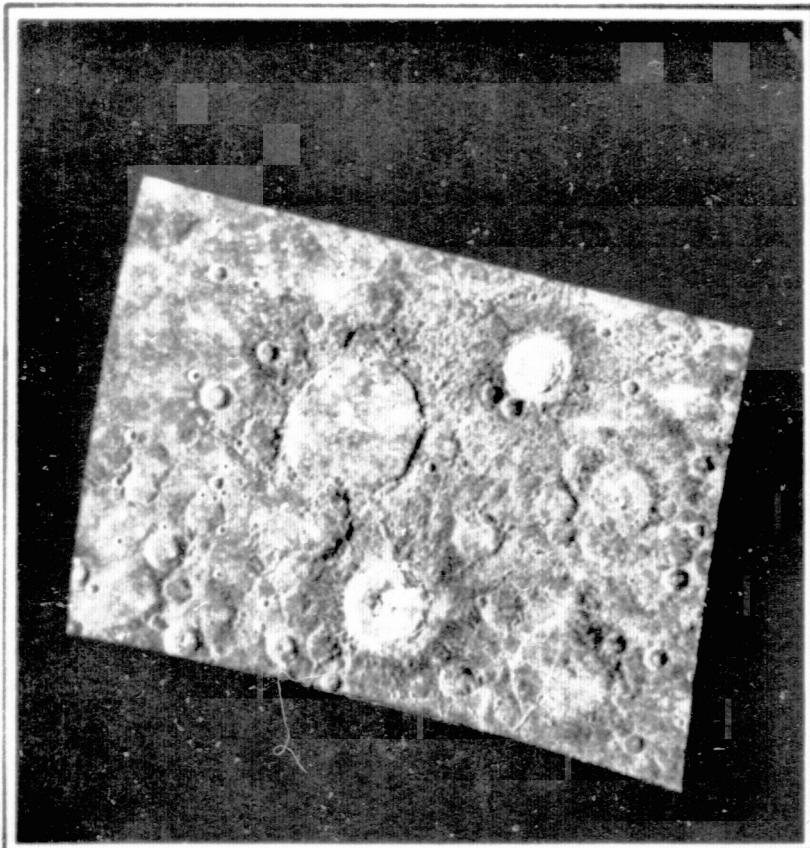


a



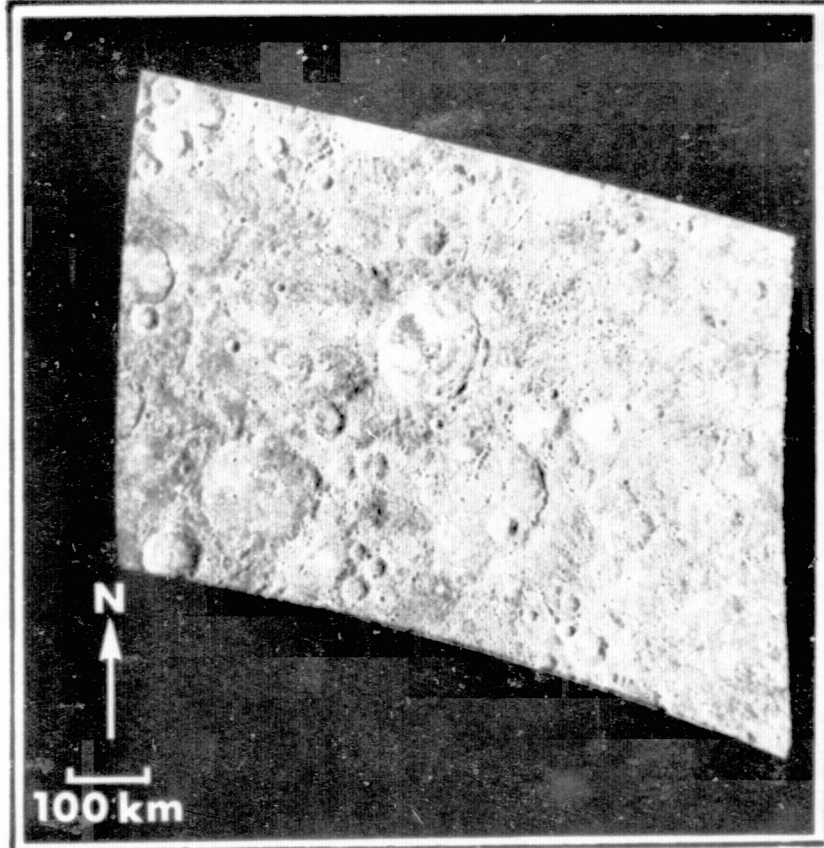
b

Figure 11



C

Figure 11



D

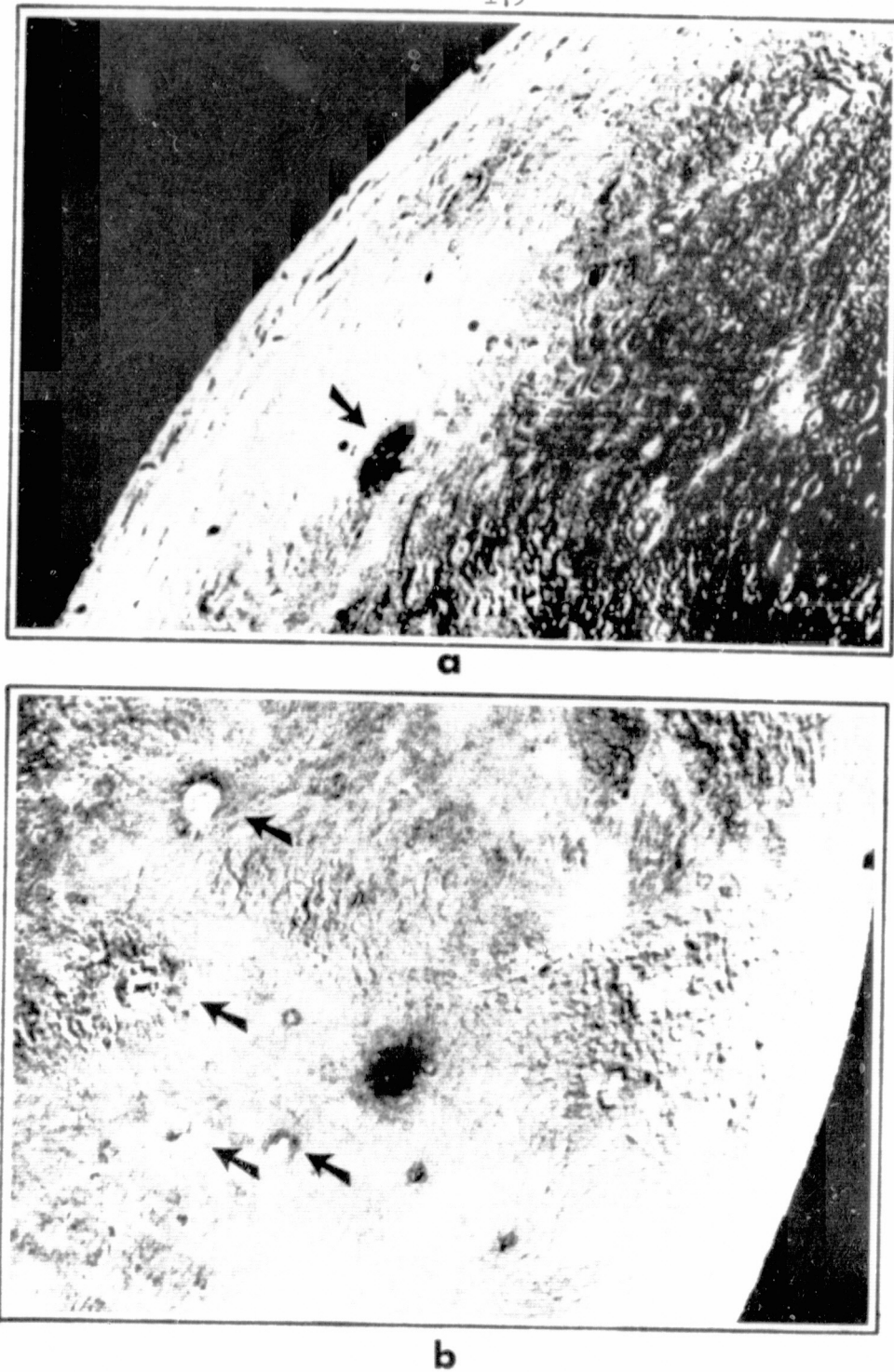


Figure 12